Tunneling and Zero-Point Energy Effects in Multidimensional Hydrogen Transfer Reactions: From Gas Phase to Adsorption on Metal Surfaces

Inaugural-Dissertation

to obtain the academic degree

Doctor rerum naturalium (Dr. rer. nat.)

Submitted to the Department of Biology, Chemistry and Pharmacy

of Freie Universität Berlin

by

Yair Ezequiel Litman

from Ciudad de Buenos Aires, Argentina.

May, 2020

This work was performed between October 2016 and May 2020 under the direction of Dr. Rossi in the Theory Department at Fritz Haber Institute of the Max Planck Society.

1st reviewer: Dr. Mariana Rossi

2nd reviewer: Prof. Dr. Beate Paulus

Date of defense: July 16th, 2020

My doctoral degree thesis entitled "Tunneling and Zero-Point Energy Effects in Multidimensional Hydrogen Transfer Reactions: From Gas Phase to Adsorption on Metal Surfaces" has been prepared by myself and it is based on my own work; the work from other has been specifically acknowledged in the text. The thesis is submitted to the Department of Biology, Chemistry and Pharmacy of Freie Universität Berlin to obtain the academic degree Doctor rerum naturalium (Dr. rer. nat.) and has not been submitted for any other degree.

Berlin, May 2020

Acknowledgments

First and foremost, I would like to thank Mariana for giving me the opportunity to perform research in her group at the Fritz Haber Institute of the Max Planck Society, and her supervision, encouragement, suggestions of all kind, training, discussions, and support throughout all these years. I thank Prof. Dr. Paulus for kindly agreeing to be my co-supervisor and reviewer of my thesis.

I would also like to thank to all my collaborators, particularly to Takashi Kumagai, and Jeremy Richardson, for their valuable contributions, fruitful scientific discussions, and insights that significantly enriched this project. My work would not have been possible without the computer infrastructure that I could access within the Max Planck Society (in MPCDF), many books obtained from the library at FHI, and access to many manuscripts guaranteed by ArXiv and Sci-hub.

I am very grateful to all my friends and colleagues from the SABIA group and theory department for the shared coffee breaks, lunches, German-lunches, and group outings. It was a pleasure to work in such a friendly atmosphere. A special thanks goes to FK for the countless discussions and walks, to Nathaniel for being Nathaniel, to Julia and Hanna for their willingness to help me every time I needed it, and to all my colleagues who took part of their time to proofread portions of this thesis. I am incredibly grateful to the Argentinean mafia, 'la peque' y Alex, for all moments that made me feel at home in this beautiful city. Gala, Mauro, Mati, Uri and Zippo, thanks for all the chats, pieces of advice, pictures, surprises, and travel experiences.

Un especial reconocimiento a la gente que hizo posible incluso arrancar este doctorado: Sergio, el equipo de la OAQ, Enrique, Hernan, Pablo y Daniel. Gracias!

Leila, fue un largo camino desde el departamento del primer piso no? Gracias por todo el apoyo y por estar siempre que lo necesite para escucharme y darme buenos consejos.

Gaby, gracias por resignificar mi vida. Brindo por el comienzo del viaje!

Abstract

Hydrogen transfer reactions play a significant role in many technological applications and fundamental processes in nature. Despite appearing to be simple reactions, they constitute complex processes where nuclear quantum effects (NQE) such as zero-point energy and nuclear tunneling play a decisive role even at ambient temperature. Moreover, the anharmonic coupling between different degrees of freedom that take place in realistic systems leads to hydrogen dynamics that, in many cases, are hard to interpret and understand.

Systematic and quantitative *ab initio* studies of hydrogen dynamics were performed in systems ranging from gas phase molecules to adsorbates on metallic surfaces using state-of-the-art methodologies based on the path integral formulation of quantum mechanics in combination with the density functional approximation. In order to achieve this task, the construction of a general infrastructure that made the required ring polymer instanton simulations feasible was created, and a new approximation which considerably reduces the computational cost of including NQE on weakly bound systems was proposed and tested in the study of water dissociation at Pt(221) surface. Practical guidelines and limitations were also discussed to help the adoption of such methodologies by the community.

The system of choice for most of the studies presented in this thesis was the porphycene molecule, a paradigmatic example of a molecular switch. The are a large number of experimental results in well-controlled environments available in the literature which have demonstrated the importance of NQE and multidimensional coupling for this molecule. Therefore, the porphycene molecule provides the unique possibility to theoretically address these effects and compare the theoretical predictions with experimental results in different environments.

A portion of this thesis focuses on the study of porphycene molecule in the gas phase. For this purpose, the intramolecular double hydrogen transfer (DHT) rates and vibrational spectrum were calculated. The theoretical results showed a remarkable agreement with the experiments, and enabled the explanation of the unusual infrared spectra, the elucidation of the dominant DHT mechanism, and the understanding of their temperature dependence. In all the cases, the coupling between low- and high-frequency modes proved to be essential to get qualitatively correct trends.

Another portion of this thesis examines molecules adsorbed on surfaces. Studies of porphycene molecules adsorbed on (111) and (110) metal surfaces showed that the stronger the surface-molecule interaction is, the more the molecule buckles upon adsorption, leading to an overall decrease of the DHT rates. The simulations identified different temperature regimes of the DHT mechanism, which was not possible by experimental measurements, and evidenced the importance of surface fluctuations on the DHT rates.

In conclusion, this thesis provides a stepping stone towards the understanding of the impact of NQE, anharmonic effects, and multidimensional mode coupling on hydrogen dynamics, and also describes novel computational tools to approach their study by using first-principle calculations.

Kurzzusammenfassung

Wasserstofftransferreaktionen spielen in vielen technologischen Anwendungen und grundlegenden Prozessen in der Natur eine bedeutende Rolle. Obwohl es sich um einfache Reaktionen zu handeln scheint, umfassen sie komplexe Prozesse, bei denen nukleare Quanteneffekte (NQE) wie Nullpunktsenergie und nukleares Tunneln auch bei Raumtemperatur von entscheidender Bedeutung sind. Darüber hinaus führt die anharmonische Kopplung zwischen verschiedenen Freiheitsgraden, die in realistischen Systemen stattfindet, zu einer Dynamik des Wasserstoffs, die in vielen Fällen schwer zu interpretieren und zu verstehen ist.

In der vorliegenden Arbeit werden systematische und quantitative ab initio Studien zur Wasserstoffdynamik in Systemen durchgeführt, die von Molekülen in der Gasphase bis zu Adsorbaten auf metallischen Oberflächen reichen. Hierbei werden Methoden eingesetzt, die auf der Pfadintegralformulierung der Quantenmechanik in Kombination mit Dichte-Funktional-Approximationen basieren. Um diese Aufgabe zu erfüllen, wird eine Infrastruktur entwickelt, die die erforderlichen Ringpolymer-Instanton-Simulationen ermöglicht. Weiterhin wird eine neue Näherung für schwachbindende Systeme vorgeschlagen und für die Wasserdissoziation auf Pt(221) Oberfläche getestet, welche die Rechenkosten für die Berücksichtigung von NQE deutlich reduziert. Ebenso werden praktische Richtlinien und Einschränkungen dieser Methode erörtert, die deren Verwendung in der Community erleichtern soll.

Das Porphycenmolekül - ein paradigmatisches Beispiel für einen molekularen Schalter - bildet die Grundlage für die meisten in dieser Arbeit vorgestellten Untersuchungen. In der Literatur gibt es eine große Anzahl von experimentellen Ergebnissen in gut kontrollierten Umgebungen, die die Bedeutung von NQE und mehrdimensionaler Kopplung für dieses Molekül gezeigt haben. Daher bietet das Porphycenmolekül die einzigartige Möglichkeit, diese Effekte theoretisch anzugehen und die theoretischen Vorhersagen mit experimentellen Ergebnissen in verschiedenen Umgebungen zu vergleichen.

Ein Teil dieser Arbeit befasst sich mit der Untersuchung von Porphycenmolekülen in der Gasphase. Zu diesem Zweck wurden die intramolekularen Doppelwasserstofftransferraten (DHT) und das Vibrationsspektrum berechnet. Die theoretischen Ergebnisse zeigen eine bemerkenswerte Übereinstimmung mit Experimenten und ermöglichen die Erklärung der ungewöhnlichen Infrarotspektren und die Aufklärung des dominanten DHT-Mechanismus, sowie das Verständnis ihrer Temperaturabhängigkeit. In allen Fällen erwies sich die Kopplung zwischen Nieder- und Hochfrequenzmoden als entscheidend um qualitativ korrekte Trends zu erhalten.

Ein weiterer Teil dieser Arbeit untersucht Moleküle, die an Oberflächen adsorbiert sind. Untersuchungen von an (111)- und (110)-Metalloberflächen adsorbierten Porphycenmolekülen zeigen, dass die Wechselwirkung zwischen Oberfläche und Molekül umso stärker ist, je mehr sich das Molekül bei der Adsorption verbiegt, was insgesamt zu einer Abnahme der DHT-Raten führt. Die Simulationen identifizieren unterschiedliche Temperaturregime des DHT-Mechanismus, was

bisher durch experimentelle Messungen nicht möglich war und hebt die Bedeutung von Oberflächenfluktuationen für die DHT-Raten hervor.

Zusammenfassend bildet diese Arbeit die Grundlage zum Verständnis des Einfluss von NQE, anharmonischen Effekten und mehrdimensionaler Modenkopplung auf die Wasserstoffdynamik und beschreibt zudem neuartige Simulationswerkzeuge für die ab initio Untersuchungen dieser Effekte.

Contents

Abbreviation List

- a.u: atomic units
- a.k.a: also known as
- AFM: atomic force microscopy
- BOA: Born-Oppenheimer approximation
- DFA: density functional approximation
- DFT: density functional theory
- DHT: double hydrogen transfer
- CMD: centroid molecular dynamics
- FHI-aims: Fritz Haber Institute ab initio molecular simulations
- GGA: generalized gradient approximation
- GLE: generalized Langevin equation
- HB: hydrogen-bond
- HDNNP: high-dimensional neural network potential
- HK: Hohenberg and Kohn
- IHT: intramolecular hydrogen transfer
- IR: infrared
- KIE: kinetic isotope effect
- KRR: kernel ridge regression
- MD: molecular dynamics
- NAO: numeric atom-centered orbitals .
- NQE: nuclear quantum effects
- NR: Newthon-Raphson
- PES: potential energy surface
- PIMD: path integral molecular dynamics
- RP: ring polymer
- RPI: ring polymer instanton
- RPC: ring polymer contraction
- RPMD: ring polymer molecular dynamics
- SD: steepest descent
- SPM: scanning Probe Microscopy
- STM: scanning tunneling microscopy
- TISE: time-independent Schrödinger equation
- TRPMD: thermostatted ring polymer molecular dynamics
- vdW: van der Waals
- w.r.t: with respect to
- TST: transition state theory
- MEP: minimum energy pathway
- WFC: work function change
- ZPE: zero-point energy

List of Publications

Paper I "i-PI 2.0: A universal force engine for advanced molecular simulations"

V. Kapil, M. Rossi, O. Marsalek, R. Petraglia, **Y. Litman**, T. Spura, B. Cheng, A. Cuzzocrea, R. H. Meißner, D. M. Wilkins, B. A. Helfrecht, P. Juda, S. P. Bienvenue, W. Fang, J. Kessler, I. Poltavsky, S. Vandenbrande, J. Wieme, C. Corminboeuf, T. D. Kühne, D. E. Manolopoulos, T. E. Markland, J. O. Richardson, A. Tkatchenko, G. A. Tribello, V. Van Speybroeck and M. Ceriotti.

Comp. Phys. Comm. ***236****, 214-223 (2019)*

Paper II "Elucidating the Nuclear Quantum Dynamics of Intramolecular Double Hydrogen Transfer in Porphycene"

Y. Litman, T. Kumagai, J. O. Richardson, M. Rossi.

J. Am. Chem. Soc. ***141****, 2526-2534 (2019)*

Paper III "Temperature dependence of the vibrational spectrum of porphycene: a qualitative failure of classical-nuclei molecular dynamics"

Y. Litman, J. Behler, and M. Rossi

Faraday Discuss., ***221****, 526-546 (2020)*

Paper IV "Quantum tunneling in real space: Tautomerization of single porphycene molecules on the (111) surface of Cu, Ag, and Au"

J. Chem. Phys. ***148****, 102330 (2018)*

T. Kumagai, J.N. Ladenthin, **Y. Litman**, M. Rossi, L. Grill, S. Gawinkowski, J. Waluk and M. Persson.

Paper V "Multidimensional Hydrogen Tunneling in Supported Molecular Switches: The Role of Surface Interactions "

Submitted

Y. Litman, and M. Rossi

Chapter 1

Introduction

1.1 Motivation

Proton, and hydrogen transfer are among the most fundamental and elementary reactions in chemistry and can be found everywhere in nature and technological applications [1]. The respiratory chain, the photosynthesis complexes, fuel cells [2], metal cracking [3], and catalysis [4] are just a few examples of their extended relevance across many disciplines. In the particular cases where the hydrogen atom changes connectivity within the same molecule, the process is called intramolecular hydrogen transfer (IHT) or tautomerism, and the two (or more) states involved in the reaction are called tautomers. [a]

Upon tautomerization, the molecules not only change their structure, but there might be also present modifications in several physicochemical properties, such as solubility, emission spectra, or absorption spectra (i.e., color). The most frequent cases of tautomerism are keto-enol and amine-imine tautomerism. Depending on the molecule and the specific conditions, namely, temperature, pH, and solvent, both tautomers may coexist in comparable proportions, or the equilibrium may be largely shifted towards one preferred tautomer. The differences in structure and electronic density between the tautomers sometimes cause them to bind differently to bio-receptors, making a huge impact in its bioactivity. Thus, the possibility to control the relative tautomeric populations via external conditions or minor derivatization of the molecule has been a target in drug design research [6–8]. Moreover, it has also been suggested that tautomerism may play a significant role in DNA mutations [9–11].

IHT has been intensively studied in solution, solid state and gas phase for many decades [12] using several spectroscopic techniques such as fluorescence spectroscopy [13], UV-vis absorption [14], X-ray and neutron diffraction [15] and nuclear magnetic resonance spectroscopy [16].

[a] Strictly speaking, the concept of tautomerism is broader. IUPAC defines it as: "Isomerism of the general form, $G-X-Y=Z \longleftrightarrow X=Y-Z-G$, where the isomers (called tautomers) are readily interconvertible. The atoms connecting the groups X, Y, Z, are typically any of C, H, O or S, and G is a group which becomes an electrofuge or nucleofuge during isomerization" [5]. In this thesis, unless specified, the term tautomerism will refer to the cases where G=H.

In recent years, with the popularization of molecular electronics, IHT was proposed as a switching mechanism in molecular devices, triggering its study on surfaces at the single-molecule level. One the of remarkable advantages of this type of switching mechanism is the fact that, in many cases, the molecule does not undergo a large conformational change upon switching, facilitating its integration in molecular circuits and the formation of self-assembled monolayers [17]. Scanning Tunneling Microscopy (STM) and Atomic Force Microscopy (AFM), usually encompass as Scanning Probe Microscopies (SPM), have opened a revolutionary avenue to study surface properties at the atomic scale already in the eighties [18,19]. Since then, the imaging capabilities have considerably improved [20–22]. Moreover, atomistic scale applications, like manipulation of atoms and molecules [23,24], and spectroscopic measurements at the single-molecule level [25–27] have been developed. Interestingly, SPM based experiments have now evidenced the ability to remotely switch between different tautomers using external stimuli of different nature, like hot carriers, photons and force [17,28–35].

STM experiments are often not straightforward to interpret, and the assistance of theoretical simulations is typically needed to arrive to a robust conclusion. In this context, simulations open a window to a nanoscopic world that is hardly achieved by experiments, upgrading the spatial resolution and complementing the time resolution. In cases where the surface does not exhibit a large surface reconstruction and the molecule under consideration has a rather simple conformational space, finding the minimum energy geometry presents no major difficulties. The calculation of approximated STM images associated to such structures, using for example the Tersoff-Hamann model [36], is a straightforward task. However, the modeling of other types of responses, like the dynamics induced by inelastic collisions of the electrons, are more challenging, and there is a lack of consensus in the community about how to adress them [37,38]. The theoretical scenario is considerably simplified when the STM tip acts only as an observer, and the external potential bias or tunneling electrons can be neglected. Even so, when dealing with tautomerization, several other challenges have to be faced. First, the light mass of the hydrogen atom means that nuclear quantum effects (NQE), like zero-point energy (ZPE) and tunneling, are substantial. Second, if quantitative and sometimes even qualitative theoretical predictions are desired, anharmonic and multidimensional coupling of the reaction coordinate with other modes cannot be neglected. Finally, if dynamical observables are going to be studied, like optical responses or chemical rates, the treatment of the nuclear dynamics at a quantum-mechanical substantially increases the level of complexity.

The work presented in this thesis tackles the problem of understanding the equilibrium properties and quantum dynamics of hydrogen transfer of molecules on metallic surfaces attempting to close, or at least narrow, the gap between experiment and theory. This enterprise is carried out mainly, but not only, using the porphycene molecule, which is introduced in the next section.

1.2 Porphycene molecule as a model to study hydrogen transfer

Reported by Vogel in the 1980s[39], porphycene molecule was the first structural isomer of porphyrin to be synthesized. As shown in Fig. 1, the central cavity shape of both molecules differs significantly. While in porphycene molecule, the rectangular shape of the cavity results in a rather small nitrogen-nitrogen distance (2.63 Å) and close to linear hydrogen-bonds (HB) (152°), in porphyrin the square shape of the cavity produces higher distances and less linear HBs (2.89 Å and 118° respectively). Compared with porphyrin molecule, the stronger HBs present in porphycene lead to a faster tautomerization rate seven orders of magnitude faster in solution at room temperature[40]. Beyond these peculiar IHT properties, porphycene molecule and its derivatives have attracted the attention of the photochemistry and photobiology communities due to their special optical properties: Substantial absorption in the red spectral region, and high triplet state formation efficiency. As a consequence, its capabilities as sensitizers in photodynamic therapy are under current investigation[41,42]. The suggested applications extend also to fields like catalysis[43,44], organic photovoltaics[45], artificial heme components[46,47] and biomotif-based magnetic molecular devices[48].

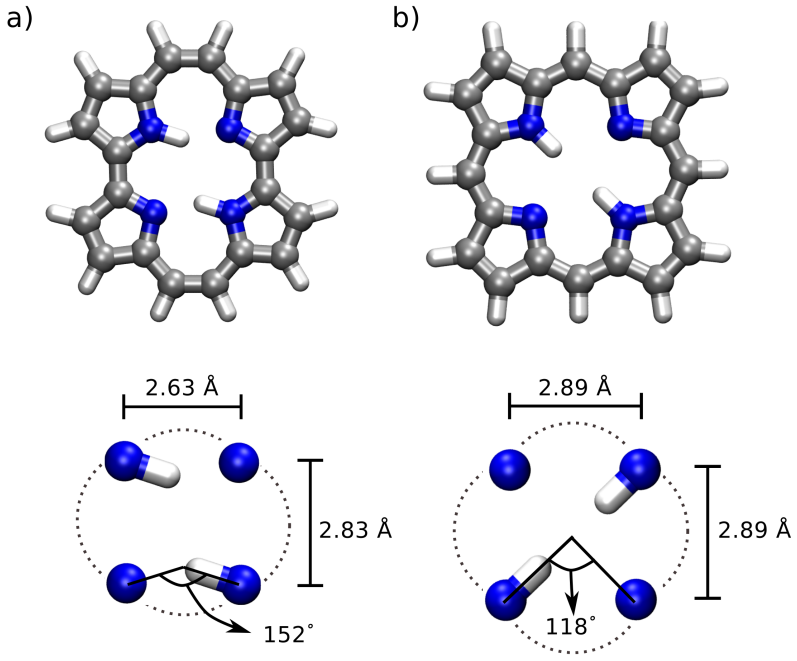

Figure 1: Molecular structures and inner cavities for a) porphycene and b) porphyrin molecules.

The research on the IHT of porphycene molecule and its derivatives constitute a rich set of studies with a numerous amount of different experimental techniques in different environments ranging from helium-nanodroples[49] and supersonic jets[50], going through different organic solutions[51] and polymeric matrices[52], up to single-molecule studies in nanoparticles[53] and metallic

surfaces[30,32]. Since in most of the cases considered here the IHT process involves the transference of two hydrogen atoms, hereafter, this process will be referred as double hydrogen transfer (DHT). Only the central results relevant for the work in this thesis are summarized here, and the interested reader is referred to the excellent recent review in Ref. 40 for further details.

Isolated Molecules [b]

High-resolution absorption and fluorescence spectra of porphycene molecule and symmetric derivatives show characteristic doublets evidencing the presence of tunneling splitting. Their origin is attributed to the coherent double hydrogen tunneling between the equivalent *trans* tautomers. Interestingly, while the ground state tunneling, which corresponds to the *trans*→*trans* reaction, is 4.4 cm^{-1}, different vibrational modes present either higher or lower tunneling splitting values[49,50]. This observation proves that the DHT reactive mode couples to several modes and it is a manifestation of the multidimensional nature of the DHT process. An impressive consequence of this fact is evidenced when the peripherical hydrogen atoms are replaced by deuterium. Even though it is a modification rather 'far' from the inner cavity, some of the tunneling splittings are increased or reduced by a factor of three[54].

Condensed Phase experiments

Similar to what is observed in the gas phase, *trans* is the most stable tautomer. In most of the situations only the *trans*→*trans* reaction is observed, even though the coexistence of both tautomers has been found for meso-alkylated derivatives[55]. In contrast to isolated molecules, the coupling with the environment damps the coherence quickly, and the coherent tunneling gives place to a rate process.

Measuring DHT rates on symmetric molecules is not a trivial task since the reactants and products present the same properties. For this purpose, ingenious polarized spectroscopy setups that take advantage of the change in the direction of the transition moment vector upon hydrogen transfer were developed[56,57]. The experiments consist in measuring the temporal profile of the absorption anisotropy signal using polarized pump and probe beams. It is possible find conditions where the primary source of depolarization is the tautomerization kinetics, and effects like rotational diffusion or intermolecular energy transfer can be neglected. Then, by an educated choice of the wavelengths of the beams, it is possible to determine the DHT rate in both the ground and lowest excited electronic states. Several porphycene derivatives have been measured in different solvents[51,55] showing that, while the solvent identity rarely affects the DHT rates, the nature of the derivatization leads to 5 orders of magnitude difference between the fastest and the slowest cases. As expected, the DHT rates have a strong correlation with standard descriptors of the hydro-

[b] The term isolated molecule is used for situations when the interaction of the molecule with other molecules and the environment is negligible, like gas phase or helium nanodroplets. Still, the measurements represent averages of a big number of independent molecules, and it should not be confused with single-molecule experiments, where only one molecule is tracked, and the interaction with the environment may be substantial.

gen bond strength like nuclear magnetic resonance chemical shifts and nitrogen-nitrogen distance. A thorough study of the temperature dependence of the DHT rates of porphycene molecule and its isotopologues, where deuterium atoms replace the internal hydrogen atoms, was reported by Ciąćka *et al.*[58]. A strong kinetic isotope effect (KIE) was observed, revealing that tunneling effects are significant even at room temperature. An Arrhenius-like behavior was also observed, and it was attributed to a vibrationally activated tunneling.

Another intriguing observation is related to the infrared (IR) spectra. The harmonic approximation predicts an intense peak around 2900 cm^{-1} for the N-H stretch mode, which compared with porphyrin ($\approx$ 3300 cm^{-1}) or NH_3 ($\approx$ 3500 cm^{-1}) makes it clear that HBs in porphycene molecule are rather strong. However, no clear indication of this vibration was observed neither in the IR nor in the Raman spectra in 2500 to 3400 cm^{-1} region at 12 K[59]. The authors in Ref. 59 considered that either a superposition of that band with the CH stretch vibration signal[c] or an extreme broadening to the extent that avoided its experimental detection were plausible explanations. Later Gawinkowski and co-workers[13], extended that study to other isotopologues and, using theoretical simulations, obtained new results supporting the broadening hypothesis. However, the poor quality of the experimental spectra, together with its discrepancy with the simulation results, have hindered a definitive answer regarding the interpretation of the NH vibrations for this molecule.

Single molecule SPM

The most novel type of experiments applied to the investigation of DHT in porphycene molecule are based on SPM techniques. SPM scans generate distinctive images for the different tautomeric states, enabling their differentiation and identification. As a result, several ways to manipulate the DHT process have been found. One possibility to control it is by the application of an external force. Landenthin and co-workers studied porphycene molecule on Cu(110), and were able to determine which portions of the molecule can induce the DHT reaction under a force stimulu, and how strong the stimulu should be in order to triger it[30]. Another possibility to control the tautomerization is the use of STM manipulation. Kumagai *et al.* showed for the same system that by manipulating an adatom in the vecinity of the molecule[32], the tautomeric state can be adjusted on demand. More specifically, different *cis* states can be achieved by regulating the position of an adatom away from the molecule along the [001] surface axis in the 5 to 10 Å range. Moreover, the DHT can be used as to sensor of the local environment. A third and interesting approach is to induce tautomerization via inelastic electron tunneling. In these cases, if the voltage of the STM is tuned appropriately, the inelastic collisions of hot electrons can excite molecular vibrations and induce the reaction[29]. Even when the voltage pulse is generated at 100 Å away from the molecule, the DHT can be induced with detectable effciency[31]. Similar results have been also obtained for the phthalocyanine[34,60]

[c] At that time no other information about the NH stretch in porphycene molecule was available in literature, so the authors were expecting to observe the signal at higher frequencies than the signal corresponding to the CH vibrations at $\approx$ 3150 cm^{-1}, as it takes place in porphyrin.

and napthalocianine[17] molecules.

The previous examples show different approaches to induce the tautomerization reaction but deliver little information regarding the dynamics of the process. One alternative to access that kind of information is to place the tip apex in one side of the molecule and set the instrument to a constant current and bias mode. As a result of the DHT process, the temporal trace of tip height produces a telegraphic signal as depicted in Fig. 2a, where the "low" and "high" states correspond to the tautomers where the inner hydrogen atoms reside further or closer from the tip (Fig. 2 b and 2c, respectively). Then, the DHT rate can be calculated either by counting the events and dividing it by the corresponding measurement time, or by fitting the histogram of interval lengths between tautomerization events (represented by the length of horizontal lines in the time trace depicted in Fig. 2a.) to an exponential function. Typically, STM measurements can measure rates in the range of 0.01 - 10 Hz, which indirectly restricts the temperature at which rate values are accessible. For example, for porphycene molecule on Cu(110) such interval is only 25 K. At higher or lower temperatures, the rates are either too fast to be tracked or too slow to get enough statistics.

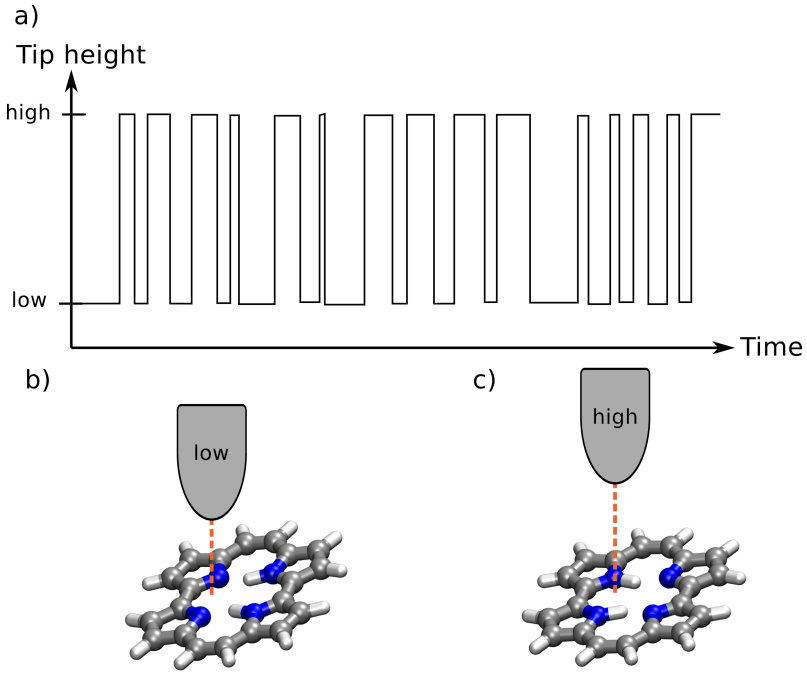

Figure 2: a) Sketch of the time trace of the STM signal obtained during a hydrogen transfer measurement experiment. b) Schematic low tip position with the corresponding porphycene tautomer. c) Analogous to b) for the high tip position.

Additionally, the DHT reaction can be thermally induced. The temperature dependence of the equilibirum DHT rates for the porphycene molecule deposited on Cu(110) and Ag(110) were studied[29,61]. In both cases, the rates presented an effective activation barrier that could not be explained by any simple rate theory (see next section), and it was concluded that hydrogen tunneling was of major relevance. Furthermore, the limited time resolution of the STM measurements made

it impossible to determine the reaction mechanism. In the Ag(110) case, the rates also presented an inexplicable sharp transition from an Arrhenius behavior to a temperature independent regime at 15K. No satisfactory explanation could be found for this anomalous behavior.

Theoretical modeling

Both, the *trans*→*trans* reaction observed in the condensed phase and isolated situations, as well as the *cis*→*cis* reaction observed on surfaces, require the transference of two hydrogen atoms. In principle, several transfer mechanisms can take place. The so-called stepwise mechanism, where the hydrogen atoms are transferred sequentially, and the reaction pathway involves an intermediate state is one of the possible scenarios. The second scenario describes the hydrogen atoms moving in a correlated fashion without passing by any stable intermediate, and it is called the concerted mechanism. The later can develop in two possible manners: one in which the hydrogen atoms move simultaneously through a second-order saddle point, and another one where there is a time delay between the movement of the two atoms. The first is called concerted synchronous, and the second concerted asynchronous mechanism.

The theoretical modeling of DHT on porphyrin and porphycenes molecules is largely due to two independent set of works leaded by Limbach [62–67], and Smedarchina and Fernandez-Ramos [68–71]. In the first group, Limbach and co-workers built the semiempirical Limbach-Bell model [72], which allows the elucidation of the hydrogen or proton transfer reaction mechanism based on the magnitude and the temperature dependence of KIEs. The model proved to be useful in interpreting experimental data of several molecules [73–75], and particularly for porphycene and porphyrin molecules, the concerted [66] and stepwise [76] mechanism were suggested, respectively. Naturally, its intrinsic dependence on the experimental data results in a lack of predictive power, and additionally, some of the considerations required to derive the model, like a parabolic barrier approximation, limits its range of applicability. Even so, Limbach's works on the porphyrin molecule are still among the most outstanding studies on double hydrogen transfer [1].

The second group of studies were carried out by Smedarchina and co-workers using a less emprical strategy. Initially, they performed a systematic 2D study on correlated DHT for different coupling strength. The main conclusion of their work was that the concerted synchronous and the stepwise mechanism are the dominant mechanisms, and their relative contribution depends on the model parameters and temperature. In contrast, the concerted asynchronous mechanism never contributes significantly [70]. Later, they also studied realistic systems by combining approximate quantum dynamics methods with dimensionality reductions techniques. Using symmetry considerations and linear coupling between the reactive coordinate and the modes orthogonal to it [71], they were able to reproduce experimental tunneling splittings and reaction rates for several systems. Limbach's results on porphyrin were confirmed, even though empirical adjustment of the barrier height were required in some cases. In the porphycene case, the comparison between theoretical results and experimental measurements showed a irreconcilable discrepancy among different sets of experimental data [68]. Due to the lack of a reliable predictive power of their approach, new

experimental measurements were suggested to resolve the dispute about the DHT mechanism.

A third and more heterogeneous group of studies, where the 108 nuclear degrees of freedom of the molecule are treated explicitly, appeared in the literature. Walewski and co-workers performed Car-Parrinello molecular dynamics simulations and, by tracking the hydrogen hopping, concluded that the DHT mechanism is mostly asynchronous concerted[77], in clear disagreement with Smedarchina results. They also performed non-equilibrium molecular dynamics simulations by adding extra kinetic energy to particular molecular normal modes. Their results showed that normal modes that involve primarily movement of the carbon and nitrogen atoms, also known as skeleton modes, might enhance or inhibit the DHT in agreement with experiments. However, the simulation considered classical-nuclei dynamics and ignored important effects like nuclear ZPE and tunneling. Yoshikawa *et al.* performed simulations based on parameterized force-fields which did include those effects[78,79]. The result demonstrated that NQE have a massive impact on equilibrium properties such as nitrogen-hydrogen distances and free energy barriers. Their work also showed that out-of-plane vibrational motions significantly couple to the DHT coordinate and decrease the contribution of the concerted mechanism. Although the methodology they used does not give access to dynamical information, the authors proposed that the DHT is mainly concerted, and the contribution of the stepwise process may increase with temperature.

Finally, only few theoretical studies investigated the porphycene molecule on surfaces. On the Cu(110) surface, a strong intermode coupling between the N-H stretching mode with an in-plane bending mode was found and it was concluded that anharmonicity plays a crucial role in the DHT reaction[80]. Predictions of the DHT rates for porphycene molecule on other (110) surfaces were performed by Li and co-workers, finding a correlation between the adsorption energy and the calculated rate[81]. However, those calculations neglected quantum tunneling effects which are known to be important. Novko *et al.* showed that the relative stability of the different tautomers needs an accurate treatment of dispersion interactions (see next section) to get even qualitatively correct results on the Cu(111) surface[82,83]. In another study by the same authors, it was found that in the same system the intermode coupling is fundamental to explain the experimental observations for DHT reactions induced by inelastic tunneling electrons[84].

On the whole, experimental and theoretical studies unambiguously point towards a description of DHT where its multidimensional nature, which emerges from the coupling of the reactive mode with plenty of modes orthogonal to it, as well as the the quantum nature of the nuclei, which gives rise to non-trivial isotopic effects and tunneling splitting, are vital constituents and should not be neglected if a comprehensive understanding is pursued. At the beginning of this thesis, an *ab-initio* treatment that includes all those effects was still missing.

1.3 Goal and Outline

The first goal of this thesis is to understand the interplay between NQE, anharmonic effects, and multidimensional mode coupling, and how they impact hydrogen dynamics in general and hydrogen transfer in particular. A second important goal is the construction of a general infrastructure that makes the required simulations feasible, delivering critical insights, and providing reliable predictions to guide current and future experiments.

The porphycene molecule is then an excellent ground where all these effects are experimentally evidenced and studied, but yet, not fully understood. Moreover, the extensive range of explored environments spanning from the gas phase to the adsorption on surfaces gives a unique framework to tackle the DHT comprehensively and systematically, and the possibility to extend the results to other tetrapyrrole molecular switches[85,86]. Ultimately, if a rational designed of molecular switches is sought, one of the fundamental prerequisites is the understanding of its equilibrium dynamical properties such as the reaction mechanism and its temperature dependence.

The results presented in this thesis are organized such that the starting point is the harmonic approximation in the gas phase. Progressively, more effects are systematically included until reaching the most complex scenario tackled in this thesis: the DHT tunneling rates on metal surfaces. This approach will allow the discrimination of the contribution of each physical effect individually making possible a deeper understanding. The work presented here will alternate between two complementary points of view, which are going to be named as 'chemistry viewpoint' and 'physics viewpoint'. Naturally, this division corresponds to a stereotype rather than a formal and well established definition, and it is used here for the sole purpose of illustration. The first one refers to an approach which aims to increase the predictive power and close the gap with the experiments at the cost of losing interpretability[87]. On the contrary, the second approach aims to gut the system under study and put into consideration only the minimum amount of ingredients required to predict the qualitative behavior and, when possible, extract general trends that may apply to other systems in different conditions.

The thesis is structured as follows: after this introduction, the theoretical background and the methodological required to carry out the simulations are described in chapter 2. Chapter 3 contains the details of the semiclassical rate theory implementation employed in this thesis, and the main results are summarized in chapter 4, followed by the publications in chapter 5. Finally, in the last chapter, the conclusions of the this thesis are presented together with a discussion of directions for future work.

Chapter 2

Theoretical Background

This chapter has the intention to be a short review of the well-established theoretical results employed in this thesis. Each topic is addressed with the necessary level of detail, such that the thesis is self-contained. Thus, this review does not aim to present the depth usually found in standard textbooks, and the interested reader is referred to the excellent books in Ref. 88–93, and the carefully picked references provided along the text.

2.1 The Many-Body Hamiltonian

Most of the systems that are relevant in the chemistry field can be described by a many-body non-relativistic Hamiltonian which reads as

$$\hat{H} = \hat{T}_{\text{nuc}} + \hat{T}_{\text{e}} + \hat{V}_{\text{nuc-e}} + \hat{V}_{\text{e-e}} + \hat{V}_{\text{nuc-nuc}}, \tag{2.1}$$

where $\hat{T}_{\text{nuc}}$ is the nuclear kinetic-energy operator, $\hat{T}_{\text{e}}$ is the electronic kinetic-energy operators, and $\hat{V}_{\text{e-e}}$, $\hat{V}_{\text{nuc-e}}$ and $\hat{V}_{\text{nuc-nuc}}$ represent the Coulombic interaction between electron-electron, electron-nucleus, and nucleus-nucleus, respectively. Explicitly, these operators are defined as [a]

$$\begin{aligned}
\hat{T}_{\text{nuc}} &= -\sum_{I}^{N} \frac{\vec{\nabla}_I^2}{2M_I}; \qquad \hat{T}_{\text{e}} = -\sum_{i}^{n} \frac{\vec{\nabla}_i^2}{2}; \\
\hat{V}_{\text{nuc-nuc}} &= \frac{1}{2}\sum_{I\neq J}^{N} \frac{Z_I Z_J}{|\vec{R}_I - \vec{R}_J|}; \qquad \hat{V}_{\text{e-e}} = \frac{1}{2}\sum_{j\neq i}^{n} \frac{1}{|\vec{r}_i - \vec{r}_j|}; \\
\vec{V}_{\text{nuc-e}} &= -\sum_{i}^{n}\sum_{I}^{N} \frac{Z_I}{|\vec{r}_i - \vec{R}_I|};
\end{aligned} \tag{2.2}$$

where $\vec{r}$, i, j are the position vector and indexes for the n electrons, $\vec{R}$, I, J are the position vector and indexes for the N nuclei, and Z_I and M_I are the nuclear charge and mass, respectively. Solving

[a] Unless specified otherwise, atomic units where the electron mass, the electron charge, and $\hbar$ are equal to unity will be used in this thesis.

this Hamiltonian in a non-relativistic and time-independent quantum-mechanical framework means to solve the time-independent Schrödinger equation (TISE) or eigenvalue problem,

$$\hat{H}\Psi = E\Psi. \tag{2.3}$$

Exact analytical solutions of the Eq. 2.3 are only available for a few limited cases, and the following section presents different practical approximations to cope with it.

2.2 Born-Oppenheimer Approximation

The first step towards the resolution of the Eq. 2.3 is the so-called Born-Oppenheimer approximation (BOA)[94]. One route to derive it, is by starting with the definition of the electronic Hamiltonian, H_e, as

$$\hat{H}_\mathrm{e} = \hat{T}_\mathrm{e} + \hat{V}_\text{nuc-e} + \hat{V}_\text{e-e}. \tag{2.4}$$

The TISE for H_e has the formal solution

$$\hat{H}_\mathrm{e}\Phi_s(\mathbf{R},\mathbf{r}) = E_s(\mathbf{R})\Phi_s(\mathbf{R},\mathbf{r}), \tag{2.5}$$

where the dependence on the nuclear position has to be understood as parametric, $\mathbf{R} = \{\vec{R}_1,\ldots,\vec{R}_N\}$. $\mathbf{R}$ should not be confused with $\vec{R}$. While the first symbol represents the positions of all the nuclei in the system, the latter one refers to the position vector of only one nucleus. The positions of the electrons are represented by $\mathbf{r}$ and $\vec{r}$ in the same way.

The set of eigenfuctions of $\hat{H}_\mathrm{e}$, $\{\Phi_s\}$, represents a complete basis that is used to expand the eigenfunctions of $\hat{H}$, denoted by $\{\Psi_\nu\}$, as

$$\Psi_\nu = \sum_s \Lambda_s^\nu(\mathbf{R})\Phi_s(\mathbf{R},\mathbf{r}), \tag{2.6}$$

where $\Lambda_s^\nu(\mathbf{R})$ are functions of the nuclear positions and represent the coefficients of such expansion[95]. After inserting Eq. 2.6 into Eq. 2.3, multiplying by $\Phi_t^*(\mathbf{R},\mathbf{r})$, and integrating over the electronic degrees of freedom, the following equation is obtained

$$E_t\Lambda_t^\nu(\mathbf{R}) = \big[\hat{T}_\text{nuc} + \hat{V}_\text{nuc-nuc} + E_t(\mathbf{R})\big]\Lambda_t^\nu(\mathbf{R}) - \sum_s\sum_I \frac{1}{2M_I}[2\vec{A}^{(1)}_{ts,I}(\mathbf{R})\vec{\nabla}_I + A^{(2)}_{ts,I}(\mathbf{R})]\Lambda_s^\nu(\mathbf{R}), \tag{2.7}$$

where the orthonormality relation of $\{\Phi_s\}$ was used, and the first and second order non-adiabatic coupling terms, $\vec{A}^{(1)}_{ts,\vec{R}_I}(\mathbf{R})$ and $A^{(2)}_{ts,\vec{R}_I}(\mathbf{R})$ respectively, are defined as

$$\vec{A}_{ts,I}(\mathbf{R}) = \int d\mathbf{r}\Phi_t^*(\mathbf{R},\mathbf{r})\vec{\nabla}_I\Phi_s(\mathbf{R},\mathbf{r}), \tag{2.8}$$

and

$$A^{(2)}_{ts,I}(\mathbf{R}) = \int d\mathbf{r}\Phi^*_t(\mathbf{R},\mathbf{r})\vec{\nabla}^2_I\Phi_s(\mathbf{R},\mathbf{r}). \tag{2.9}$$

The BOA consists in considering that $\vec{A}^{(1)}_{st,I}(\mathbf{R})$ and $A^{(2)}_{st,I}(\mathbf{R})$ are equal to zero, making possible to solve Eq. 2.5 and Eq. 2.7 independently. This approximation is equivalent to assuming that the electrons adapt instantaneously to the movement of the nuclei, and therefore, the nuclear movement cannot induce any electronic excitation. For this reason, the BOA is also called adiabatic approximation, and the hypersurfaces defined by

$$V^{\mathrm{BO}}_{nuc,s}(\mathbf{R}) \coloneqq E_s(\mathbf{R}) + V_{\text{nuc-nuc}}(\mathbf{R}), \tag{2.10}$$

are called adiabatic surfaces, BO surfaces, or merely potential energy surfaces (PES). The fact that the electrons are much lighter than the nuclei produces that, in most situations, the BOA works exceptionally well. However, in cases where the energy difference between the adiabatic surfaces is small, like in the vicinity of conical intersections or metallic systems, the approximation can break down[96–98]. In the present work, it is assumed that the BOA remains valid and only the ground state BO surface will be considered. Thus, one has to solve the *electronic problem* given by the electronic Hamiltonian, $\hat{H}_{\mathrm{e}}$, and afterwards the *nuclear problem* given by the nuclear Hamiltonian, $\hat{H}_{\mathrm{nuc}}$. The later is given by the application of the BOA to Eq. 2.7, and it is defined as

$$\hat{H}_{\mathrm{nuc}}\Lambda^{\nu}_0(\mathbf{R}) \coloneqq \left[\hat{T}_{\mathrm{nuc}} + V^{\mathrm{BO}}_{\mathrm{nuc},0}(\mathbf{R})\right]\Lambda^{\nu}_0(\mathbf{R}), \tag{2.11}$$

where the subindex 0 refers to the BO ground state. Hereafter, the 0 subindex and BO supraindex will be dropped for simplicity.

It is worth to emphasize that until now electrons and nuclei are treated on equal footing, i.e., as quantum particles, and the consideration of the nuclei as distinguishable or classical particles are approximations that can be taken in addition to the BOA. Practical, efficient, and accurate methods for solving Eq. 2.4 and Eq. 2.11 are areas of active research[99], and the remainder of this chapter discusses some of them.

2.3 Methods to Solve the Electronic Problem

Most of the methodologies described in this section are based on the variational principle[90]. It states that for a given Hamiltonian, $\hat{H}_{\mathrm{e}}$ in this case, the ground state energy, E_0, is the minimum expectation value that can be achieved for any normalized wave function, Φ. Formally it reads,

$$E_0 = \min_{\Phi}\langle\Phi|\hat{H}_{\mathrm{e}}|\Phi\rangle, \tag{2.12}$$

where the Dirac notation for the inner product has been used. One of the oldest approaches, and also the foundation of many modern methods, of finding the ground state wavefunction is based on this principle, and it is called the variational method. In this approach, a set of normalized trial

wave functions which depend on one or several parameters is considered, and a minimization of the expectation value of the energy with respect to (w.r.t.) the set of those parameters is performed. The resulting solution realizes the best approximation to E_0 and to the ground state wave function that belongs to the considered set.

2.3.1 Hartree and Hartree-Fock methods

The Hartree method is among the first relevant attempts to solve the Eq. 2.5 [100]. In this method, the wave function ansatz is a product of single-particle wave functions,

$$\Phi = \chi_1(\mathbf{X}_1)\chi_2(\mathbf{X}_1)\dots\chi_n(\mathbf{X}_n), \tag{2.13}$$

where the parametric dependence on $\mathbf{R}$ has been dropped for simplicity. $\mathbf{X}_j = (\vec{r}_j, m_{s,k})$ are the spatial and spin coordinates of the electron j, and χ_j represents a single-particle wave function, or spin-orbital. Since H_e does not depend explicitly on the spin variables, the spin-orbitals can be expressed as a product of a spin function, σ, and a spatial orbital, ψ_j, i.e.,

$$\chi_j(\mathbf{X}_j) = \psi_j(\vec{r}_j)\sigma(m_{s,k}). \tag{2.14}$$

The resulting energy expression, obtained by introducing Eq. 2.14 and 2.13 in Eq. 2.5 and integrating out the spin variables, reads as

$$\begin{aligned} E_{\mathrm{HA}} =& \sum_i^n \left[-\frac{1}{2}\int d\vec{r}\psi_i^*(\vec{r})\vec{\nabla}_i^2\psi_i(\vec{r})\right] \\ &+ \sum_i^n \left[-\sum_I^N Z_I \int d\vec{r}\psi_i^*(\vec{r})\frac{1}{|\vec{r}-\vec{R}_I|}\psi_i(\vec{r})\right] \\ &+ \sum_i^n \left[\frac{1}{2}\sum_{j\neq i}^n \int\int d\vec{r}\, d\vec{r\prime}\psi_i^*(\vec{r}\,)\psi_j^*(\vec{r\prime})\frac{1}{|\vec{r}\,-\vec{r\prime}|}\psi_i(\vec{r}\,)\psi_j(\vec{r\prime})\right], \end{aligned} \tag{2.15}$$

where the first, second and third terms of the right hand-side correspond to the the kinetic energy, the electron-nucleus electrostatic interaction energy, and the electron-electron electrostatic interaction energy. The last term can be interpreted as an effective single-particle potential energy that emerges from the mean electrostatic interaction of each electron with the rest of the electrons present in the system. Since this interaction is defined by the orbitals, which in turn are the sought solution, the Eq. 2.15 has to be solved self-consistently. However, the most severe problem that this approach presents is that the wave function ansatz does not fulfill the Pauli principle.

Slater proposed an elegant way to overcome this problem and to include the anti-symmetric nature of the electronic wave function by construction [101]. The suggestion takes the following form,

$$\Phi = \frac{1}{\sqrt{n!}}\begin{vmatrix} \chi_1(\mathbf{X}_1) & \dots & \chi_n(\mathbf{X}_1) \\ \vdots & \ddots & \vdots \\ \chi_1(\mathbf{X}_n) & \dots & \chi_n(\mathbf{X}_n) \end{vmatrix}, \tag{2.16}$$

where $|\bullet|$ stands for the determinant operation which fulfills the required symmetry. Later, Fock [102] proposed to use a Slater determinant as the ansatz for the wave function, and applied the variational principle to find the electronic ground state. This method is known as the Hartree-Fock method (HF), and leads to the HF equations which are also solved self-consistently. Its solution yields a set of orthonormal orbitals, $\{\psi_k\}$, with orbital energies, $\{\epsilon_k\}$. The Slater determinant formed from the n orbitals with the lowest energy is then the HF ground state wave function, Φ_0^{HF}, and represents the best variational approximation to the ground state of a system in the single-determinant picture.

The Hartre-Fock energy, E_{HF}, is given by

$$\begin{aligned} E_{\mathrm{HF}} &= E_{\mathrm{HA}} - \frac{1}{2}\sum_{i,j\neq i}^{n}{}' \int\int d\vec{r}\, d\vec{r\prime}\psi_i^*(\vec{r})\psi_j^*(\vec{r\prime})\frac{1}{|\vec{r}-\vec{r\prime}|}\psi_i(\vec{r\prime})\psi_j(\vec{r})\Big] \\ &\coloneqq E_{\mathrm{HA}} + E_{\mathrm{x}}, \end{aligned} \tag{2.17}$$

where in the last line the exchange energy, E_{x}, is defined. In the last equation, the spin variables have also been integrated out, and the prime symbol indicates that the sum runs only over the electrons with the same spin. It is possible to include the terms where $i = j$ in the expression for E_{HF} because the terms coming from the electron-electron electrostatic interaction energy (Eq. 2.15) cancel exactly with the terms coming from the exchange energy. Since the first terms represent an unphysical self-interaction energy, i.e., a single electron interacting with its own charge density, the HF method is said to be self-interaction free. Additionally, and certainly more important, is the fact that this method fulfills the Pauli principle by construction. Even though the HF methods typically recovers more than 98% of the exact ground state total energy of the system, the remaining 2% is an enormous amount of energy, which is much larger than, for example, the energy of chemical bonds. This remainder is called correlation energy, E_{c}, and is defined as $E_{\mathrm{c}} \coloneqq E_0 - E_{\mathrm{HF}}$.

Accurate simulations that make use of more advanced wave-function-based are methods globally called under the name 'post-Hartree-Fock' techniques. Loosely speaking, try to capture the missing 2%. Some of them are briefly discussed in the next section.

2.3.2 Post-Hartree-Fock Methods

As mentioned before, the HF ground state wave function is the Slater determinant formed by the n lowest energy orbitals or 'occupied orbitals'. It is also possible to build other Slater determinants replacing one or more 'occupied orbitals' by the same amount of 'unoccupied orbitals'. Considering the electrons as effective single particles, the interchange between orbitals can be interpreted as electronic excitations since one or more electrons are being promoted from the 'occupied orbitals' in the HF ground state to 'unoccupied' ones. Moreover, it is possible to prove that the exact ground state wave function can be written as a linear combination of all possible determinants, i.e the HF ground state and all the possible excitations. The application of the variational method to find all the corresponding coefficients of such expansion is extremely computational demanding and rarely used. If all the possible electronic configurations are considered in the description of the wave function, this method is called full-configuration interaction (full-CI). In addition to

the computational cost, the truncation of the expansion by including excitations only up to a fixed number of electrons causes size-consistency problems, i.e., the energy of two non-interacting molecules is not twice the energy of one of them calculated at the same level of approximation.

A perturbative treatment, known as second-order Møller-Plesset (MP2), appears as a simple alternative to the full-CI approach[103]. It is the lowest non-vanishing correction term to HF, straightforward to implement, relatively efficient, and has advantages and pitfalls that are well understood and documented[104]. Among its most important disadvantages, one can find that MP2 does not follow a variational principle, meaning that it is possible to find a total energy lower than the exact energy given by the BOA. Furthermore, it overestimates the correlation energy in systems containing strongly electronegative atoms, transition metals, or anions[105], and cannot be applied to metallic system.

A different approach is the coupled cluster (CC) theory in which the wave function ansatz is expressed as,

$$\Phi_{\mathrm{CC}} = e^{\hat{T}}\Phi_0^{\mathrm{HF}} = (1 + \hat{T} + \frac{\hat{T}^2}{2!} + \frac{\hat{T}^3}{3!} + \dots)\Phi_0^{\mathrm{HF}}, \tag{2.18}$$

where $\hat{T}$ is the 'excitation operator' and can be grouped in contributions coming from single, double, triple or higher order electronic excitations ($\hat{T} = \hat{T}_1 + \hat{T}_2 + \hat{T}_3 + \dots$). The action of $\hat{T}_1$ can be expressed as

$$\hat{T}_1\Phi_0^{\mathrm{HF}} = \sum_{a}^{\text{occ.}} \sum_{r}^{\text{unocc.}} t_a^s \Phi_a^s, \tag{2.19}$$

where Φ_a^s represents an Slater determinant were the 'occupied orbital' a was replaced by the 'unoccupied' orbital s, and t_a^s are coefficients to be determined. The other $\hat{T}_n$ operators are defined analogously. This theory does not follow a variational principle but, unlike MP2, it is size extensive. The most used expansion is the so-called CCSD(T) where 2.19 is solved for $\hat{T} = \hat{T}_1 + \hat{T}_2$ and triple excitations, $\hat{T}_3$, are added perturbatively a posteriori. It formally scales as $O(M^7)$, where where M is a measure of the size of the system, making this method extremely expensive. Educated approximations can sensibly reduce its computation cost, and close to linear scaling has been proposed[99,106,107]. The quantum chemistry community often refers to it as the 'gold-standard', and it is widely distributed in commercial computational packages. However, since it only contains a single reference Slater determinant, the so-called static correlation effects, needed to describe multiple electronic configurations present in some bond-breaking processes, degenerate electronic states or electronically excited states, cannot be captured[108]. Multireference-CC methods have been proposed and are currently under active development[109].

Current progress in other promising wave-function-based approaches like Quantum Monte Carlo[110] or machine-learning-based methods[111,112] may compete with CCSD(T) as the standard 'reference method' in the not so distant future. When feasible, CCSD(T) is used as a benchmark to validate lower level and more efficient calculations based on approximations to density functional theory (DFT), which is the main electronic structure method used in this thesis and, therefore, it is presented in the next section.

2.3.3 Density Functional Theory

A completely different approach to solve Eq. 2.5 can be traced back to the ideas of Thomas and Fermi [b]. They proposed that instead of placing the many-body wave function as the central quantity to describe the electronic ground state, the electron density defined as

$$\rho(\vec{r}) = \int d\sigma_1 d\mathbf{X}_2 \dots d\mathbf{X}_n |\Phi(\mathbf{R}, \mathbf{r})|^2, \tag{2.20}$$

could be used. In the previous equation, the dependence on $\mathbf{R}$ is only parametric and it has been omitted in the left-hand side of the equation. The main motivation of making this transition is that total number of degrees of freedom has been reduced to only three, the coordinates of the vector $\vec{r}$. These ideas were not seriously considered until Hohenberg and Kohn (HK) put them on firm and rigorous foundations through their two well-known theorems [113].

It is instructive to come back to the original problem in Eq. 2.4 and Eq. 2.12, and rewrite it in a slightly different way. First, the electron-nucleus interaction can be easily written as density functional,

$$\langle \Psi | \hat{V}_{\text{nuc-e}} | \Psi \rangle = -\sum_I^N Z_I \int d\vec{r} \frac{\rho(\vec{r})}{|\vec{r} - \vec{R}_I|} \coloneqq \int d\vec{r} \rho(\vec{r}) v_{\text{ext}}(\vec{r}) \coloneqq F_{\text{ext}}[\rho] \tag{2.21}$$

where $F_{\text{ext}}[\rho]$ is the external energy density functional, and v_{ext} has been defined for reasons that will become clear later. Then, the variational principle can be reformulated as [114]

$$\begin{aligned}
E_0 &= \min_{\Phi} \langle \Phi | \hat{H}_{\text{e}} | \Phi \rangle \\
&= \min_{\rho} \left\{ \min_{\Phi \to \rho} \langle \Phi | \hat{H}_{\text{e}} | \Phi \rangle \right\} \\
&= \min_{\rho} \left\{ \min_{\Phi \to \rho} \langle \Phi | \hat{T}_{\text{e}} + \hat{V}_{\text{e-e}} + \hat{V}_{\text{nuc-e}} | \Phi \rangle \right\} \\
&= \min_{\rho} \left\{ \min_{\Phi \to \rho} \langle \Phi | \hat{T}_{\text{e}} + \hat{V}_{\text{e-e}} | \Phi \rangle + \langle \Phi | \hat{V}_{\text{nuc-e}} | \Phi \rangle \right\} \\
&= \min_{\rho} \left\{ \min_{\Phi \to \rho} \langle \Phi | \hat{T}_{\text{e}} + \hat{V}_{\text{e-e}} | \Phi \rangle + F_{\text{ext}}[\rho] \right\} \\
&= \min_{\rho} \Big\{ F[\rho] + F_{\text{ext}}[\rho] \Big\},
\end{aligned} \tag{2.22}$$

where $F[\rho]$ is given by,

$$F[\rho] = \min_{\Phi \to \rho} \langle \Phi | \hat{T}_{\text{e}} + \hat{V}_{\text{e-e}} | \Phi \rangle, \tag{2.23}$$

and the symbol $\min_{\Phi \to \rho}$ should be interpreted as a constrained minimization among the wave functions Φ that yield the density ρ. The only requirement imposed on ρ is that it is associated to an asymmetric wave function, which is usually refereed as the N-representable condition. Levy [114]

[b] The numerous references can be found in chapter 3 in Ref. 88.

and Lieb [115] showed that: i) $F[\rho]$ exists, ii) when it is fed with the ground state density, $\rho_0(r)$, and added to $F_{\text{ext}}[\rho_0]$, delivers E_0, and iii) it fulfills the following variational principle,

$$F[\rho_0] \leqslant F[\rho], \tag{2.24}$$

for any N-representable ρ. Thus, the HK theorems can be seen in some extent as the particular case of the previous three statements applied to v-representable densities, i.e. densities associated with non-degenerate antisymetric ground state wavefunctions defined by an external potential, v_{ext}. More specifically, Hohenberg and Kohn proved that: i) there is a unique mapping between v_{ext} and $\rho_0(r)$, apart from a trivial additive constant, which proves the existence of $F[\rho]$, and ii) $\rho_0(r)$ minimizes $F[\rho]$, and therefore fulfills the variational principle in Eq. 2.24.

$F[\rho]$ can formally be written as the sum of three density functionals representing the electronic kinetic energy, $F_{\text{kin}}[\rho]$, the exchange and correlation energy, $F_{\text{xc}}[\rho]$, and the classical electrostatic interaction of the n electrons or Hartree energy, $F_{\text{H}}[\rho]$,

$$F[\rho] = F_{\text{kin}}[\rho] + F_{\text{xc}}[\rho] + F_{\text{H}}[\rho]. \tag{2.25}$$

While the exact and general analytic formulae of the first two density functionals are still unknown, even though their existence is guaranteed, the last functional is explicitly given by

$$F_{\text{H}}[\rho] = \frac{1}{2}\int\int d\vec{r}\,\vec{r\prime}\frac{\rho(\vec{r})\rho(\vec{r\prime})}{|\vec{r}-\vec{r\prime}|} \coloneqq \frac{1}{2}\int d\vec{r}\rho(\vec{r})v_{\text{H}}(\vec{r}), \tag{2.26}$$

where the Hartree potential, $v_{\text{H}}(\vec{r})$, has been defined in the last equality. Finally, combining Eq. 2.21, 2.25 and 2.26, the total energy density functional can be written as

$$E[\rho] = F_{\text{kin}}[\rho] + F_{\text{xc}}[\rho] + F_{\text{H}}[\rho] + F_{\text{ext}}[\rho]. \tag{2.27}$$

It is possible to minimize the equation 2.27 w.r.t. to the density subjected to the constrain $\int d\vec{r}\rho(\vec{r}) = n$, and get the following Euler equation

$$\mu = \frac{\delta F_{kin}[\rho]}{\delta\rho} + v_{\text{H}} + v_{\text{xc}} + v_{\text{ext}}, \tag{2.28}$$

where the exchange-correlation (XC) potential, $v_{\text{xc}} = \frac{\delta F_{\text{xc}}[\rho]}{\delta\rho}$ has been defined, and μ is the Lagrange multiplier which turns to be the chemical potential.

So far all the equations are exact within the BOA, and in order to proceed further, approximations to F_{kin} and F_{xc} are required. The most adopted scheme to solve these equations in practice is known as the Kohn-Sham (KS) scheme, proposed by Kohn and Sham in 1965 [116], and it is reviewed in the next section.

Kohn-Sham Equations

The KS method proposes to solve 2.12 through an auxiliary more manageable problem of non-interacting particles. The corresponding Hamiltonian reads

$$\hat{H}_{\mathrm{KS}} = \hat{T}_{\mathrm{s}} + \hat{V}_{\mathrm{s}}, \tag{2.29}$$

where $\hat{T}_{\mathrm{s}}$ and $\hat{V}_{\mathrm{s}}$ represent the kinetic energy operator of non-interacting particles and the effective external potential energy operator, respectively. The only condition imposed on $\hat{V}_{\mathrm{s}}$, and due to the HK theorems determines it uniquely, is that the solution of Eq. 2.29 should give the same ground state density as the solution of Eq. 2.4. The existence of $\hat{V}_{\mathrm{s}}$ is not guaranteed for any v-representable density, but for all practical purposes this fact does not represents a problem since there is a non-interacting v-representable density which is arbitrary close to it [c].

Similarly to Eq. 2.27, and assuming that ρ is a non-interacting v-representable density, the energy functional can be expressed as

$$E^{KS}[\rho] = T_{\mathrm{s}}[\rho] + F_{\mathrm{s}}[\rho] = T_{\mathrm{s}}[\rho] + F_{\mathrm{H}}[\rho] + F_{\mathrm{xc}}^{\mathrm{KS}}[\rho] + F_{\mathrm{ext}}[\rho], \tag{2.30}$$

where $F_{\mathrm{H}}[\rho]$ and $F_{\mathrm{ext}}[\rho]$ are the same as in Eq. 2.27, $T_s[\rho]$ is the kinetic energy density functional of the non-interacting system (see Eq. 2.32 below), and $F_{\mathrm{xc}}^{\mathrm{KS}}[\rho]$ is defined as the remaining part which absorbs all quantum-mechanical many-body effects, i.e. the exchange and correlation energy and the part of the real electronic kinetic energy that is not captured by $T_s[\rho]$. This definition implies that $F_{\mathrm{xc}}^{\mathrm{KS}}[\rho]$ is not the same as $F_{\mathrm{xc}}[\rho]$.

The wavefunction corresponding to the KS non-interacting system can be written as a Slater determinant composed by the KS spin-orbitals, and, equivalent to Hartree-Fock theory, the KS Hamiltonian is reduced to n single-particle equations,

$$\hat{h}^{\mathrm{KS}}\psi_i^{\mathrm{KS}}(\vec{r}) = [-\frac{1}{2}\vec{\nabla}^2 + v_{\mathrm{s}}]\psi_i^{\mathrm{KS}}(\vec{r}) = [-\frac{1}{2}\vec{\nabla}^2 + v_{\mathrm{H}} + v_{\mathrm{xc}}^{\mathrm{KS}} + v_{\mathrm{ext}}]\psi_i^{\mathrm{KS}}(\vec{r}) = \epsilon_i^{\mathrm{KS}}\psi_i^{\mathrm{KS}}(\vec{r}), \tag{2.31}$$

where $\hat{h}^{\mathrm{KS}} = -\frac{1}{2}\nabla^2 + v_{\mathrm{s}}$, $v_{\mathrm{s}}[\rho] = \frac{\delta F_{\mathrm{s}}[\rho]}{\delta\rho}$, $v_{\mathrm{xc}}^{\mathrm{KS}}[\rho] = \frac{\delta F_{\mathrm{xc}}^{\mathrm{KS}}[\rho]}{\delta\rho}$, and ψ_i^{KS} and ϵ_i^{KS} are the KS spatial orbitals and the orbital energies, respectively. $\hat{T}_{\mathrm{s}}[\rho]$ is then given by

$$T_{\mathrm{s}}[\rho] = -\frac{1}{2}\sum_i^n \int d\vec{r}(\psi_i^{\mathrm{KS}})^*(\vec{r})\vec{\nabla}^2\psi_i^{\mathrm{KS}}(\vec{r}), \tag{2.32}$$

and the density by,

$$\rho(\vec{r}) = \sum_i^n |\psi_i^{\mathrm{KS}}(\vec{r})|^2. \tag{2.33}$$

[c] See section 3.2 in Ref. 90 for a deeper discussion.

The total energy can be computed in terms of the eigenvalues as [?]

$$E^{\mathrm{KS}}[\rho] = \sum_{i}^{n} \epsilon_i^{\mathrm{KS}} - \frac{1}{2}\int d\vec{r}\rho(\vec{r})v_{\mathrm{H}}(\vec{r}) - \int d\vec{r}\rho(\vec{r})v_{\mathrm{xc}}(\vec{r}) + F_{\mathrm{xc}}^{\mathrm{KS}}[\rho], \tag{2.34}$$

where the last tree terms on the right hand-side of the equation avoid double-counting coming from the bare sum of the eigenvalues.

One more time, the equations have to be solved self-consistently since v_{s} depends on the ρ, which in turn depends on the orbitals, which are the part of the solution itself. In Fig. 3, a sketch of the KS scheme is presented.

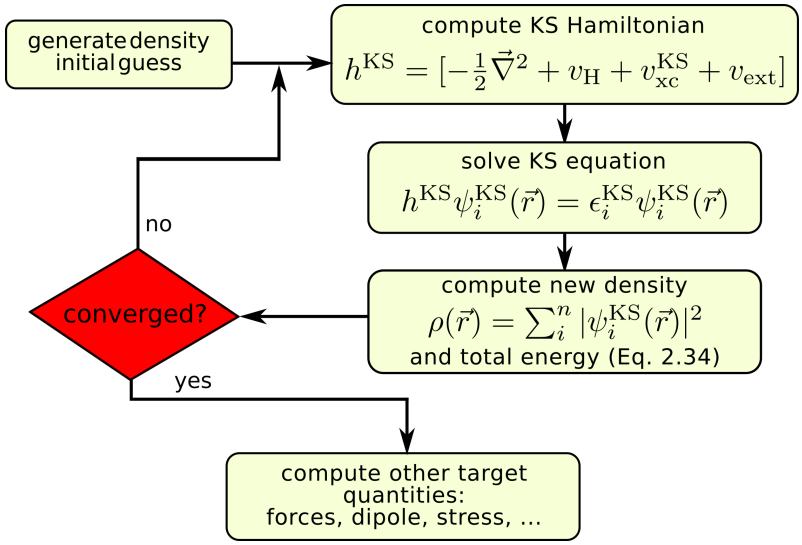

Figure 3: Workflow of a KS self-consistent calculation.

The success of the KS method resides on the important fact that it accurately describes most of the kinetic energy, which, by the virial theorem, has to be of the same order of magnitude as the potential energy. The computational expense of solving the KS equations is similar to the Hartree method and below the HF method since, in contrast to the non-local operator that appears in the HF equations, v_{s} is often approximated by a (semi-)local operator. Unfortunately, the KS scheme loses the original idea of Thomas-Fermi of representing the solution with only three variables, even though it provides a considerable efficient scheme that includes correlation effects and formally scales only as $O(M^3)$. As Kohn noted in his Nobel lecture, DFT "has been most useful for systems of very many electrons where wave function methods encounter and are stopped by the exponential wall." Other approaches that have tried to come back to the origins are the orbital-free density functional theory methods [117,118] but, at the moment, its popularity is rather low in comparison to the KS scheme.

The sets of spatial orbitals, $\{\psi_i^{\mathrm{KS}}\}$, and eigenvalues, $\{\epsilon_i^{\mathrm{KS}}\}$, that appear in Eq. 2.31 are by definition only a mathematical construction whose only physical meaning is given by the density they generate [d]. However, it has been shown that in many cases, they represent a much better

[d] The Janak's theorem is an exception of this [119].

description than HF orbitals, and, when their approximate nature is not overlooked, they serve as a useful tool to gain a deeper understanding of the system under study [120,121].

XC Functionals

DFT is an exact theory, and it does not present breakdowns. The deficiencies that appear in practical applications are due to the the imperfect available approximations to $F_{\mathrm{xc}}^{\mathrm{KS}}$, which at the same time, make possible any realistic density functional calculation, and ultimately, define its accuracy. For this reason and hereafter, the actual calculations are going to be named by DFA, density functional approximation, to make a clear distinction with the exact theory behind it. The exact functional is still unknown, but different exact, impractical, and useful expressions have been derived [122,123], as well as many of the constraints that it must fulfill [124].

A discussion about the different types and versions of XC functionals with their exact definitions and historical background is far beyond the scope of this chapter, and the interested reader is referred to Ref. 121, 125–129, and references therein. Instead, a short description of the XC functionals used in this work with their established overall performance is provided:

- PBE

  In order to overcome the severe limitations that the local density approximation (LDA) functionals presents in the chemistry domain, the community devised a new generation of functionals where an explicit dependence on the density gradient was introduced: the generalized gradient approximation or GGA. The GGA XC functionals are expressed as

$$F_{\mathrm{xc}}^{\mathrm{GGA}}[\rho] = \int d\vec{r}\rho(\vec{r})\epsilon_{\mathrm{x}}^{\mathrm{HEG}}(\rho(\vec{r}))f_{\mathrm{xc}}(\rho(\vec{r}), \nabla\rho(\vec{r})), \tag{2.35}$$

  where $\epsilon_{\mathrm{x}}^{\mathrm{HEG}}$ is the exchange-density functional of the homogeneous electron gas (HEG), and f_{xc} is the so-called factor enhancement, which varies across the different GGA parametrizations. Arguably the most used GGA XC functionals is the one suggested by Perdew, Burke, and Ernzerhof (PBE) [130]. PBE is a non-empirical functional, meaning that all parameters were derived from considering exact limits, and do not depend on experimental data. It presents a fair accuracy among molecules and solids [131,132]. In most of the cases improves several basic molecular properties, like atomization energies, electron affinities and ionization potentials, and reaction energies w.r.t LDA XC functionals [126]. Regarding solids, it is known to overestimatimate equilibrium lattice constants by approx. 1%, and presents an overall trend to under-bind systems [133]. Of particular interest to the present thesis, and due to the fact that self-interaction and delocalization errors over-stabilize delocalized states, hydrogen bonds are systematically artificially strengthened. As a consequence, most of the GGA XC functionals lead, for example, to a more structured liquid water and an underestimations of hydrogen transfer barriers [134,135].

- B3LYP and PBE0

  B3LYP[136–139] and PBE0[140] are among the used XC that belong to the hybrid XC functionals class. In this category, a fraction of the HF exchange is included in the XC functional, with the following general kind of linear mixing

$$F_{\mathrm{xc}}^{\mathrm{hybrid}}[\rho] = a_0 F_{\mathrm{x}}^{\mathrm{HF}}[\rho] + a_1 F_{\mathrm{x}}^{\mathrm{LDA}}[\rho] + a_2 F_{\mathrm{x}}^{\mathrm{GGA}}[\rho] + a_3 F_{\mathrm{c}}^{\mathrm{GGA}}[\rho], \tag{2.36}$$

  where the subindex 'x' and 'c' refer to exchange and correlation functionals, respectively. Even though this inclusion leads to a sensible increase of the computational cost due to the necessity to evaluate the HF exchange non-local operator, the rewards are worthy. More specifically, the self-interaction and delocalization errors are in a large extent reduced which tends to provide more accurate results. The B3LYP formulation has three empirical parameters obtained by a fitting procedure, while PBE0 has only one parameter based on a more sound theoretical basis[140]. For this reason, B3LYP is mainly used for molecules, for which it has been fitted and where it benefits from error cancellation. It is normally avoided for solids in general, and metals in particular, where the inhability to capture the homogeneous electron gas limit and the lack of long-range screening effects of the Coulomb operator leads to a poor performance[141,142]. For these reasons, when performing hybrid DFA calculations B3LYP will be used exclusively for molecular systems, and PBE0, and its related version with an screened Coulomb potential, HSE06[143], will be employed when surfaces are present in the system under consideration.

- VdW corrections

  The long-range van der Waals (vdW) dispersion interaction is an attractive interaction between atoms that originates from the correlation of electronic density fluctuations at distant positions in space. More specifically, it stems from the long-range part of the electronic correlation, and since its leading term is the instantaneous dipole - induced dipole interaction, the resulting energy has the well known $1/R^6$ asymptotic decay with the interatomic separation R. For the considered XC functionals, it can be shown that the interaction of two neutral atoms, in the limit of large separation, decays in the same way that their density overlap does, i.e. exponentially. The reason for this artificial long-range behavior stems from the incomplete description of the electronic correlation energy which uses only (semi-)local information of the electronic density[144,145].

  Several strategies have been developed to tackle this problem. The most common and efficient way to achieve it is by using an empirical pairwise corrections to the DFA energy with the following functional form

$$E_{\mathrm{DFA+vdW}} = E_{\mathrm{DFA}} - \frac{1}{2}\sum_a \sum_b f(R_{ab}) C_6^{ab} / R_{ab}^6, \tag{2.37}$$

where R_{ab} is the interatomic distance between the atoms a and b, f is an empirical damping function that that couples the (semi-)local and long-range contributions of the electron correlation, and C_6^{ab} are empirical parameters that have to be determined. A two widespread adopted schemes to perform such determination comes from Grimme *et al.*[146] and Tkatchenko *et al.*[147] which includes some kind of information about the atomic environment. Both methods contain a high degree of empiricism, and for example, they can be slightly modified to capture many-body collective long-range response of solids (known also as screening) to achieve higher accuracy when dealing with molecules on surfaces[148,149]. Other more general approaches like the many-body dispersion[150] and non-local vdW functionals[151,152] are also available and can deliver greater accuracy in some situations at the price of an increased computational effort. Overall, and independent of the particular vdW correction chosen, it is nowadays accepted that they are required to reach a reasonable accuracy for weakly bonded systems[134,145,153].

The accuracy of the approximations discussed is nowadays well-documented, and in most of the cases their domains of applicability are established. However, when applied to a particular problem, its accuracy cannot be trusted blindly, and their results should be verified against experimental results in well-defined environments or validated with higher theory methods when possible.

Solving Kohn-Sham Equations in Practice

One way to solve Eq. 2.31 is to expand the single-particle orbitals into a set of basis functions, $\{\phi_j\}$, as

$$\psi_i^{\mathrm{KS}}(\vec{r}) = \sum_j C_{ij}\phi_j(\vec{r}). \tag{2.38}$$

Inserting the previous equation into Eq. 2.31, the following generalized eigenvalue problem is obtained

$$\sum_j h_{lj}^{\mathrm{KS}} C_{ij} = \epsilon_i^{\mathrm{KS}} \sum_j s_{lj} C_{ij}, \tag{2.39}$$

where $h_{lj}^{\mathrm{KS}} = \langle\phi_l|\hat{h}^{\mathrm{KS}}|\phi_j\rangle$, and $s_{lj} = \langle\phi_l|\phi_j\rangle$ is the overlap matrix element. A KS calculation starts with the calculation of the overlap matrix and an initial guess for the C_{ij} coefficients which defines the corresponding initial guess for the density. Afterwards, the following three steps are repeated until the difference between the old and the new density and total energy are below a certain threshold:

- calculate the KS Hamiltonian by computing all the matrix elements $\langle\phi_l|\hat{h}^{\mathrm{KS}}|\phi_j\rangle$
- solve the eigenvalue problem in Eq. 2.39 to obtain the new C_{ij}
- calculate the new density using Eq. 2.38 and Eq. 2.33, and the total energy using Eq. 2.34

After the calculation converges, other quantities, besides the density and the total energy, are often computed. Normally, the atomic forces are computed since they are needed to carry out geometry optimizations or many other algorithms which displace the nuclear positions (see next section). The standard procedure to perform such calculation is by using the Hellmann-Feynman theorem[154]. Additionally, when the basis set depends on the nuclear positions, the so-called Pulay terms, which accounts for incomplete nature of any basis set used in practical applications, have to be computed[155].

The selection of the basis set is at the very heart of DFA and many other *ab initio* methods. For a given chosen XC functional, it determines the final accuracy of the calculation and the computational cost. The basis functions adopted in the field of DFA and quantum-chemistry software packages can be categorized in two groups: extended or localized ones. Plane waves are prominent example of first group while Gaussian orbitals of the second one. Most of the calculations in this thesis were performed using the FHI-Aims software[156]. It as an all-electron, full-potential electronic structure code which uses numeric atom-centered orbitals (NAOs). The NAOs in FHI-aims are expressed as

$$\phi_j(\vec{r}) = \frac{g_j(|\vec{r}|)}{|\vec{r}|} Y_{lm}(\Omega) \tag{2.40}$$

where Y_{lm} refer to the real parts ($m = 0, \ldots, l$) and imaginary parts ($m = -l, \ldots, -1$) of complex spherical harmonics, Ω is the angular spherical coordinate of $\vec{r}$, and $g_i(r)$ are numerically tabulated radial functions, which are obtained by solving the radial 1D Schrödinger-like equation.

Even though the formal scaling of DFA is $O(M^3)$, modern DFA codes which take advantage of the nearsightedness principle have a much more favorable scaling. The nearsightedness principle states that the density change at a point $\vec{r_0}$ caused by a potential change at point $\vec{r}$ far away from it is small and decays to zero for $|\vec{r_0} - \vec{r}| \to \infty$[157–159]. This electronic localization is particularly useful in the operations required for density update and the integration of matrix elements h_{ij}, leading to close to linear scaling in calculations up to thousands of atoms[160–163]. Even for non-local operators, like the exchange integral required for the hybrid XC functionals, linear scaling implementations have been reported[164,165].

When a periodic calculation is performed, the Bloch theorem is the crucial tool that makes possible to deal with the in principle infinite amount of atoms. It states that the eigenfunctions of a single-particle Hamiltonian with a periodic potential need to satisfy

$$\Psi_{n,\vec{k}}(\vec{r} + \vec{L}) = e^{\mathrm{i}\vec{k}\vec{L}} \Psi_{n,\vec{k}}(\vec{r}), \tag{2.41}$$

where $\vec{L}$ is a lattice vector, $\vec{k}$ is a wave vector confined to the first Brillouin zone, and n is the band index, which labels the different solutions for a fixed $\vec{k}$[166]. As a consequence, the eigenfunctions can also be written as

$$\Psi_{n,\vec{k}}(\vec{r}) = e^{\mathrm{i}\vec{k}\vec{r}} u_{n,\vec{k}}(\vec{r}), \tag{2.42}$$

where $u_{n,\vec{k}}(\vec{r})$ is a periodic function with the same periodicity as the Hamiltonian. Then, for a fixed $\vec{k}$ value, it is sufficient to solve for $u_{n,\vec{k}}$ within the unit cell only. Nonetheless, the total wave function requires the sampling of the $\vec{k}$-space, which is generally performed by a discrete grid of the symmetry-irreducible part of the first Brillouin zone.

2.4 Methods to Solve the Nuclear Problem

2.4.1 Rewriting the Problem

The equation 2.11 is harder to solve than it would seem at first glance. Let's consider a system with N nuclei. Trying to solve the exact TISE naively, would first require to get the full PES or at least several values from where to interpolate it. Considering only 20 discretization points per coordinate would lead to 20^{3N-6} electronic structure calculations that rapidly becomes intractable. On top of that, the ground state nuclear wave function does not encode all the needed information. At thermal equilibrium, and considering the nuclei as indistinguishable particles, all the states are populated with a population weight proportional to the Boltzmann factor, $e^{-\beta E_n}$, where E_n is the energy of the corresponding state, $\beta = 1/k_{\mathrm{B}}T$, k_{B} is the Boltzmann constant and T is the temperature[167]. Unlike the electronic states, whose energy difference is $\approx$ 30.000 K, the energy separation of the nuclear states ranges between a few thousand K down to few K. The available thermal energy can be comparable to the spacing of energy levels, and, consequently, many sates may become more populated and their contributions to a given observable increase.

The two arguments presented above make clear that, if the goal is to study systems composed by more than few atoms at thermal equilibrium, a different strategy has to be taken. Such strategy can be based on the theory of statistical mechanics. Again, the wave function is taken away from its central role to describe the system properties, and it is replaced by the so-called partition functions. These functions contain all the thermodynamic information, and even though they cannot be accessed for systems beyond simple models, they serve as a theoretical ground where practical methods are built on. Unless specified, we will focus almost exclusively in situations where the thermodynamic control variables are the number of particles, the volume and the temperature, a.k.a the canonical ensemble. The explicit dependency on the first two will be omitted for clarity.

2.4.2 Classical Equilibrium Properties

When considering nuclei as classical particles, the corresponding classical partition function, $Q^{\mathrm{CL}}(\beta)$, can be expressed as[91,167]

$$Q^{\mathrm{CL}}(\beta) = \frac{1}{(2\pi\hbar)^{3N}} \int d\mathbf{R} d\mathbf{P} e^{-\beta H_{\mathrm{nuc}}(\mathbf{R},\mathbf{P})}, \tag{2.43}$$

where $H_{\mathrm{nuc}}(\mathbf{R},\mathbf{P})$ is the classical counterpart of $\hat{H}_{\mathrm{nuc}}$ in Eq. 2.11, $\mathbf{R} = \{\vec{R}_1, \ldots, \vec{R}_N\}$ and $\mathbf{P} = \{\vec{P}_1, \ldots, \vec{P}_N\}$ are the nuclear positions and conjugated momenta, respectively. The classical static properties of the systems can be calculated as integrals of the form

$$\langle A \rangle_{\mathrm{CL}} = \frac{1}{(2\pi\hbar)^{3N} Q^{\mathrm{CL}}(\beta)} \int d\mathbf{R} d\mathbf{P} A(\mathbf{R}, \mathbf{P}) e^{-\beta H_{\mathrm{nuc}}(\mathbf{R},\mathbf{P})}, \tag{2.44}$$

where A is an observable. Importantly, when A is a function of the nuclear positions exclusively, $A = A(\mathbf{R})$, the integral over the momenta in Eq. 2.44 can be done analytically since the exponential factor can be factorized ($e^{-\beta H_{\mathrm{nuc}}} = e^{-\beta T_{\mathrm{nuc}}} e^{-\beta V_{\mathrm{nuc}}}$), and the so-called classical configurational integral is obtained

$$\langle A \rangle_{\mathrm{CL}} = \frac{1}{Z(\beta)} \int d\mathbf{R} A(\mathbf{R}) e^{-\beta V_{\mathrm{nuc}}(\mathbf{R})}, \tag{2.45}$$

where

$$Z(\beta) = \int d\mathbf{R} e^{-\beta V_{\mathrm{nuc}}(\mathbf{R})}. \tag{2.46}$$

The ergodic hypothesis states that averages over time are equal to the averages over the statistical ensemble[92]. Thus, a convenient and general algorithm to evaluate the integral in Eq. 2.45, which is an ensemble average, is by employing the molecular dynamics (MD) technique. In MD simulations, the nuclear positions are evolved according to the Hamilton equations of motions generated by $H_{\mathrm{nuc}}(\mathbf{R}, \mathbf{P})$

$$\dot{\vec{R}}_I = \frac{\partial H_{\mathrm{nuc}}}{\partial \vec{P}_I}, \tag{2.47}$$

and

$$\dot{\vec{P}}_I = -\frac{\partial H_{\mathrm{nuc}}}{\partial \vec{R}_I}. \tag{2.48}$$

These equations generate trajectories that keep the energy constant and therefore sample a microcanonical distribution. In order to get constant temperature simulations, and sample the canonical distribution, a reservoir of energy, i.e., a thermostat, is coupled to the system. The most common ones can be based on deterministic[168,169] dynamics or stochastic dynamics[170,171]. Assuming ergodicity, the thermodynamical average of the observable A, $\langle A \rangle_{\mathrm{CL}}$, is computed as the average of the function $A(\mathbf{R}, \mathbf{P})$ along the generated trajectory. If $A(\mathbf{R}, \mathbf{P})$ does not depend on time, other methods can be used as well[172,173].

In Eq. 2.43 the assumption that the nuclei are classical particles is of central importance. This approximation is well justified in cases where the system's largest characteristic frequency, ω, fulfills the relation $k_{\mathrm{B}}T/\hbar\omega >> 1$. For typical nitrogen-hydrogen or oxygen-hydrogen bonds, with a frequency corresponding to a few thousand K, it is not appropriate anymore. In the remaining of this chapter, a possible methodology to tackle the situations where the quantum nature of the nuclei cannot be ignored is presented.

2.4.3 Quantum Equilibrium Static Properties and Classical Isomorphism

In order to introduce the remaining concepts in this chapter, a 1D Hamiltonian, $\hat{H} = \hat{T} + \hat{V}$, is considered. The multidimensional generalization for distinguishable particles is straightforward, and can be found in the references provided at the beginning of the chapter. The quantum canonical partition function for distinguishable particles, $Q(\beta)$, is given by

$$Q(\beta) = \mathrm{Tr}[e^{-\beta\hat{H}}] = \sum_n e^{-\beta E_n}, \tag{2.49}$$

where Tr refers to the trace operation, E_n are the eigenvalues of $\hat{H}$, and the last equality has been obtained by evaluating the trace in the basis of the eigenfunctions of $\hat{H}$. Since the trace is invariant w.r.t. the representation, it can be expanded in any complete set of states. For instance, in the position representation, it reads

$$Q(\beta) = \int_{-\infty}^{+\infty} \langle x|e^{-\beta\hat{H}}|x\rangle dx. \tag{2.50}$$

While the potential energy operator can be easily evaluated in this basis, the kinetic energy operator is not. Therefore, the Boltzmann operator, $e^{-\beta\hat{H}}$, which in quantum mechanics cannot be factorized as $e^{-\beta\hat{T}}e^{-\beta\hat{V}}$ since $\hat{T}$ and $\hat{V}$ do not commute, cannot be evaluated straightforwardly. It is, however, possible to write the Boltzmann operator with the help of the Trotter theorem as

$$\begin{aligned} Q(\beta) &= \lim_{P\to\infty} \int_{-\infty}^{+\infty} \langle x|e^{-\beta\hat{H}}|x\rangle dx \\ &= \lim_{P\to\infty} \int_{-\infty}^{+\infty} \langle x|[e^{-\beta\hat{V}/2P}e^{-\beta\hat{T}/P}e^{-\beta\hat{V}/2P}]^P|x\rangle dx \\ &:= \lim_{P\to\infty} \int_{-\infty}^{+\infty} \langle x|\hat{\Omega}^P|x\rangle dx, \end{aligned} \tag{2.51}$$

where $\hat{\Omega}$ is defined in the last equality. Inserting the identity operator in the form of

$$\hat{I}_k = \int dx|x^{(k)}\rangle\langle x^{(k)}| \tag{2.52}$$

between each $\hat{\Omega}$ operator, and following the standard derivation presented elsewhere[91], the next important equations are obtained

$$Q(\beta) = \lim_{P\to\infty} Q_P, \tag{2.53}$$

and

$$Q_P = (\frac{mP}{2\pi\beta\hbar^2})^{P/2} \int dx^{(1)} \dots dx^{(P)} e^{-\beta_P U_P(x^{(1)},\dots,x^{(P)})}, \tag{2.54}$$

where $\beta_P = \beta/P$, m is the particle mass, and U_P is given by

$$U_P(x^{(1)}, \ldots, x^{(P)}) = \sum_{k=1}^{P} \frac{1}{2} m\omega_P^2 (x^{(k+1)} - x^{(k)})^2 + V(x^{(k)}), \tag{2.55}$$

with $\omega_P = (\beta_P \hbar)^{-1}$ and $x^{(P+1)} = x^{(1)}$, as consequence of the trace operation.

The expectation value of an operator which does not depend on momenta, $\hat{A} = A(\hat{x})$, can be written as

$$\langle A \rangle = \frac{1}{Q(\beta)} Tr[\hat{A} e^{-\beta \hat{H}}] = \frac{1}{Q(\beta)} \int dx \langle x | e^{-\beta \hat{H}} | x \rangle A(x), \tag{2.56}$$

and following similar steps as before, it can be rewritten as

$$\langle A \rangle = \lim_{P \to \infty} \frac{1}{Q_P} \left(\frac{mP}{2\pi\beta\hbar^2}\right)^{P/2} \int dx^{(1)} \ldots dx^{(P)} \left[\frac{1}{P} \sum_{k=1}^{P} A(x^{(P)})\right] e^{-\beta_P U_P(x^{(1)}, \ldots, x^{(P)})}, \tag{2.57}$$

The Eq. 2.55 represents the potential energy of a closed necklace composed of P linked 'beads' or ring polymer. Each bead is connected to its immediate neighbors by harmonic springs with a spring constant equal to $m\omega_P^2$, and it is subject to the action of the physical potential V. The spring terms emerge from the factorized kinetic energy operators in the position representation, and the spring constant is proportional to the mass and the square of the temperature. In the classical limit of infinite mass or temperature, the ring polymer collapses, and becomes a point particle, i.e., a classical particle. In this way, the finite spatial extension of the ring polymer can be seen pictorially as a measure of the particle delocalization. The configurational integral in the Eq. 2.57 reduces to the classical configurational integral in Eq. 2.45 when $P = 1$ providing a direct connection between exact quantum statistical mechanics for indistinguishable particles and its classical counterpart[e]. In Fig. 4, these concepts are summarized in a visual representation.

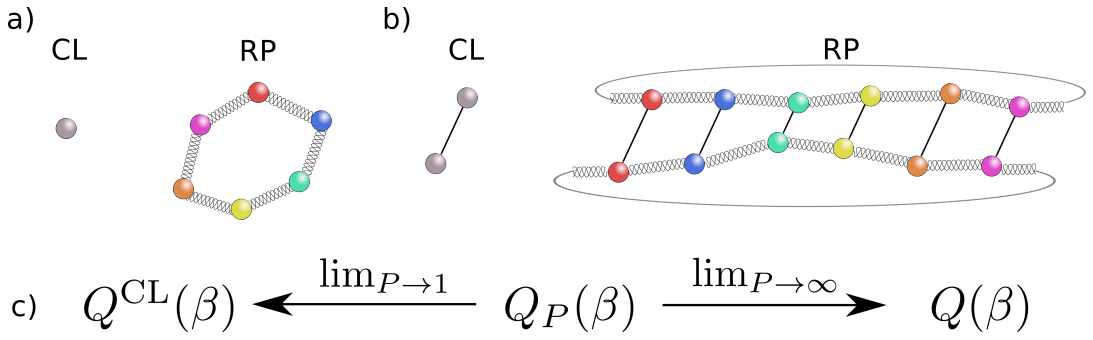

Figure 4: Classical (CL) and ring polymer (RP) representation of monoatomic (a) and diatomic (b) molecules . In both cases, the ring polymer is made of 6 beads ($P = 6$), and each color represents a different imaginary time slice (see main text). Fig. c) shows how the ring polymer partition function, $Q_P(\beta)$, works as an interpolation function between the classical partition, $Q^{\mathrm{CL}}(\beta)$, function for $P = 1$, and the quantum partition function, $Q(\beta)$ for $P \to \infty$.

[e] Important progress in path integral simulations for indistinguishable particles has been recently reported [174,175].

The remarkable result of the previous expressions is that the *quantum* static expectation value of a given position-dependent operator can be computed by a *classical* configurational integral on an extended position space. This famous relation is known as the 'classical isomorphism'[176]. One of the greatest strengths of this formulation is that the multi-dimensional generalization is trivial, and it only requires to add an extra index to each bead that runs over the Cartesian coordinates of each particle. As a result, the computational schemes based on this formulation have the desirable feature of presenting a linear scaling w.r.t. the dimensionality.

In a broader view, the Boltzmann operator in Eq. 2.50 can be thought as a time-evolution operator, $e^{-i\hat{H}\tau/\hbar}$, but in imaginary time, $\tau = -i\beta\hbar$, also known as Wick Rotation[177]. Thus, the ring polymers are discrete representations of cyclic paths in imaginary time with time length equal to $\beta\hbar$, and the integral in Eq. 2.54 performs a sum over all such paths assigning to each one a weight of $e^{-S_P/\hbar}$, where S_P is a discretized version of the Euclidean action and it is given by

$$S_P/\hbar = \beta_P U_P. \tag{2.58}$$

For this reason, this formalism is usually named as 'imaginary time path integral' to differentiate it from the 'real time path integral' one, which can be used to describe the dynamics of quantum systems.

Theoretically, the limit of $P \to \infty$ has to be taken in the previous equations. In practice, the P value has to be increased until convergence is obtained, which usually happens at a small integer multiple of $k_{\mathrm{B}}T/\hbar\omega_{\max}$, with $\omega_{\max}$ being the highest characteristic frequency of the system under study. The configurational integral in the Eq. 2.57 can be sampled with Monte Carlo algorithms, but a more elegant idea was proposed by Parinello and Rahman in the 1980s[178]. They reintroduced the momenta in the equation 2.54 to obtain a Hamiltonian, H_P, which reads

$$H_P(x^{(1)}, \ldots, x^{(P)}) = \sum_{k=1}^{P} \frac{(p^{(k)})^2}{2m^{(k)}} + U_P(x^{(1)}, \ldots, x^{(P)}), \tag{2.59}$$

where $p^{(k)}$ represents a fictitious conjugated momenta, and $m^{(k)}$ is a fictitious mass assigned to the k-th bead that can take any convenient value. In the most general case, it is represented by a matrix which does not need to be diagonal, and it is known as the Parrinello-Rahman mass matrix. The classical dynamics generated by the equations of motion of H_P at a temperature $P \times T$ provides a practical algorithm to evaluate the classical isomorphic configurational integral. As pointed by the authors in the same paper, the trajectories generated by this approach do not have any real meaning, and are simply a computational sampling device. Nowadays, this method is a standard methodology, and it is known as path integral molecular dynamics or PIMD.

2.4.4 Reducing the Computational Cost of PIMD Simulations

As stated above, each step in a PIMD simulation requires P evaluations of the physical potential. Since these evaluations are normally what determines the major portion of the total computational

effort, PIMD simulations are in principle roughly P times more costly than the corresponding classical MD simulations, where only one evaluation of the physical potential is performed per step. However, several techniques have been developed in the last decades to considerably reduce the overhead associated with the inclusion of NQE[179].

The techniques can be classified into three groups. The first group exploits the fact that PIMD simulations are MD simulations in an extended phase space. Automatically, all the methodologies developed to enhance the sampling procedure, and therefore, reduce the length of the simulations, such as, replica-exchange MD[180], metadynamics[181], and hyperdynamics[182], as well as techniques that aim to reduce the number of force evaluations, like multiple-time steps algorithms[183,184], can be applied directly to PIMD without significant modifications.

The second group contains methods that aim to reduce the number of beads needed to obtain a target property within the desired accuracy. One example of such methodologies are techniques that, instead of applying the second-order Trotter factorization in Eq. 2.51 which has an $O(P^{-2})$ error, apply higher-order factorization schemes with the more attractive $O(P^{-4})$ error scaling[185]. The major technical issue of these methods, which was the need of calculating the Hessian matrix at each simulation step, has been solved[186], and nowadays, they constitute an appealing approach, especially for low temperatures or high-accurate simulations. Approaches based on perturbation theory, which improves the convergence of the second-order and high-order schemes by the calculation of improved estimators without requiring additional computational efforts, have been also reported[187,188]. The second considerably successful example in this group makes use of colored noise thermostat based on the generalized Langevin equation (GLE)[189,190]. In this approach, each bead is attached to an independent instance of the same specially constructed GLE thermostat. The thermostat is constructed in an extended momentum space so that the non-Markovian process described by the GLE equation can be replaced by a Markovian one, and the need to keep track of the trajectory history is avoided. Their construction is done in such a way that the expectation values of the quantum kinetic and potential energy are exact in the harmonic limit for any number of replicas. Typically, the construction works as follow. First, the corresponding frequency-dependent fluctuations of the desired estimators are obtained in the harmonic limit, and the constrains that have to be enforced on them determined. Second, the merit functions that will measure the quality of the thermostat performance are defined, and finally, the optimization to obtain the thermostat parameters is performed. Even though the thermostats are optimized to reproduce the harmonic limit, they have shown excellent performance for anharmonic systems as well, where the required number of beads to obtain converged results is normally reduced by a factor of around five. The main drawbacks of this approach are that it is not guaranteed an improvement in the convergence for observables not considered during the optimization, even though the asymptotic convergence with P is ensured, and that it cannot be easily combined with re-weighting techniques, since the probability of finding an specific configuration during the simulation cannot be written as a simple function of the instantaneous positions.

Finally, the last group tries to reduce the number of force evaluations without sacrificing too

much the accuracy of H_P. The key observation to accomplish this goal resides on the fact that long-range forces are less sensitive to the specific position of the beads inside each ring polymer, and therefore, can be evaluated in a contracted ring polymer with fewer beads. The most elegant contraction scheme is the one that uses the ring-polymer normal modes to reduce the number of beads by Fourier interpolation[191,192], and it was coined with the name of ring polymer contraction or RPC. Initially designed for force-field calculations, where the short-range and long-range contribution can be easily separated, the *ab initio* extension was recently devised[193–195]. The method relies on finding an appropriate reference potential, V_{ref}, which has a low computational cost and captures the short-range component of the true potential. Then, it is possible to write

$$\sum_{k=1}^{P} V(x^{(k)}) \approx \frac{P}{P'} \sum_{k=1}^{P'} \left[V(q^{(k)}) - V_{\text{ref}}(q^{(k)}) \right] + \sum_{k=1}^{P} V_{\text{ref}}(x^{(k)}), \tag{2.60}$$

where $q^{(k)}$ are the bead positions in the contracted ring polymer. The term inside of the square brackets contains desirably only long-range components of the potential and therefore it is suitable to be evaluated in a contracted ring polymer, with $P' < P$. In the best case scenario, $P' = 1$ can be taken, and, if the reference potential has a negligible computation cost, the classical cost is reached. In practice, convergence w.r.t to P' has to be inspected. Moreover, since the long-range components tend to vary slowly in time, multiple-time step algorithms can be used in combination to reduce even further the number of force evaluations. Since it has a well defined conserved quantity, RPC can be combined with all the methods already described.

The main limitation to apply the Eq. 2.60 is to find a proper reference potential that fulfills the required properties, which severely limits its application. In the frame of this thesis, a new type of approximation that extends the previous ideas, and overcomes the need of having a reference potential when dealing with weakly bounded systems, like molecules on surfaces, has been proposed. Taking into account that molecules typically have much higher characteristic frequencies than surfaces, the new scheme proposes to describe the molecules fully quantum-mechanically and the surface and molecule-surface interaction with a 'more classical' description. This imprecise definition can be recast rigorously into the path integral formalism: the molecule is treated with a larger number of beads than the surface. Formally, the approximation is expressed as

$$\sum_{k=1}^{P} V(x^{(k)}) \approx \frac{P}{P'} \sum_{k=1}^{P'} \left[V(q^{(k)}) - V_{\text{mol}}(q_{\text{mol}}^{(k)}) \right] + \sum_{k=1}^{P} \left[V_{\text{mol}}(x_{\text{mol}}^{(k)}) \right] \tag{2.61}$$

where again $q^{(k)}$ refers to the coordinates of a contracted ring polymer containing only P' beads with $P' \leqslant P$ and the label 'mol' refers that the potential and the positions vector neglects the degrees of freedom corresponding to surface atoms. In Fig. 5 a schematic representation of the equation 2.61 is shown. The first sum goes up to P' and should be seen as a 'more classical' description of the full system, while the second sum can be understood as a quantum correction that only affects the molecular fluctuations.

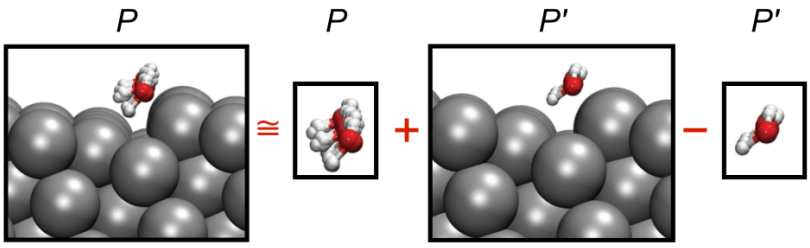

Figure 5: Graphical representation of the SL-RPC approximation applied to water adsorbed on Pt(221). Reprinted from Litman *et al.* J. Chem Phys. **148**, 102320 (2018), with the permission of AIP Publishing.

Since the scheme is a RPC that is spatially localized, this approximation is named SL-RPC. Beyond the conceptual insight that it provides, the attractiveness of SL-RPC is related to the reduction in computational cost. Commonly, the cost associated with the simulation of the bare adsorbates is minor in comparison to the one associated with the full system. Thus, the saving in cost is roughly given a factor of P'/P, and, in the best case scenario, when $P' = 1$, quantum results are obtained at a classical cost without requiring any reference potential. SL-RPC has two additional desirable features, like any other RPC based approach: First, the approximation is systematically improvable by increasing the value of P', and second, since only the RP Hamiltonian is being approximated, it can be coupled to any of the techniques already discussed.

A neat way to estimate the error induced by Eq. 2.61, and to extract a 'rule of thumb' whether this approximation is good or bad, is to consider a harmonic model (see section II.D in **Paper VI**). The main result that arises from this analysis is that the meaning of 'weak' or 'strong' interaction in this context can be easily addressed. In essence, the adsorbate harmonic frequencies of the fully relaxed system (adsorbate + surface) should be compared with the frequencies of the bare adsorbate at the same geometry. When the difference in the high-frequency modes, which are the highly quantized ones, is smaller than $10 - 15\%$, the interaction is considered weak and, as will be shown in chapter 4, SL-RPC works exceptionally well. Conversely, when the interaction is considered strong, the SL-RPC approximation is rather poor and should not be used. This characterization is also proposed to give a more rigorous and quantitative definition of what is usually named chemisorption and physisorption, respectively.

2.4.5 Approximate Quantum Time Dependent Properties I: (Thermostatted) Ring Polymer Molecular Dynamics

So far, only calculations of equilibrium time independent properties have been discussed. The access to real time properties with the path integral formalism requires, in principle, the use of real time rather than imaginary time techniques. Unfortunately, the real time propagator presents the severe problem of having oscillatory integrands, which makes extremely challenging to converge the calculations. The final result usually emerges from a massive cancellation of terms, the so-

called 'interference effects', and approximations in order to suppress them lead naturally to a less accurate description of the quantum dynamics. The problem of oscillatory integrals is relevant to other fields of applied mathematics, and is known as the 'sign problem'.

Several methods have been considered to tackle the complex and open problem of nuclear quantum dynamics. Methods that make use of the numerically exact imaginary time information, and try approximately to reconstruct the real time information, like the maximum entropy numerical analytical continuation [196,197] are highly accurate in the short time dynamics. However, information for times longer than $\beta\hbar$ requires simulations with statistical errors below one part in a thousand [198]. Other methodologies like linearized semiclassical-initial value representation (LSC-IVR) [199–201], or forward-backward semiclassical dynamics [202], despite of being exact in the short-time limit, the limit of a harmonic potential, and the high-temperature limit, since the quantum Boltzmann distribution is not conserved, they present an unphysical energy flow from the high-frequency modes to low frequencies ones, known as the ZPE leakage problem [203,204]. In this thesis, the focus is set in a method which does conserve the quantum mechanical equilibrium distribution and, due to its efficient nature, can be easily coupled with *ab initio* electronic structure calculations.

Dynamical properties, like diffusion constants, IR absorption spectra, or chemical reaction rates, can be related to an important family of functions called time correlation functions (TCF). Given two operators, $\hat{A}$ and $\hat{B}$, the 'standard' quantum TCF, $c_{\mathrm{AB}}(t)$, is defined by

$$c_{\mathrm{AB}}(t) = \frac{1}{Q} Tr[e^{-\beta\hat{H}}\hat{A}e^{i\hat{H}t}\hat{B}e^{-i\hat{H}t/\hbar}], \tag{2.62}$$

and its corresponding classical analog reads

$$c_{\mathrm{AB}}^{\mathrm{CL}}(t) = \frac{1}{2\pi\hbar Q^{\mathrm{CL}}(\beta)} \int dxdpA(x(0),p(0))B(x(t),p(t))e^{-\beta H(x(0),p(0))}, \tag{2.63}$$

where $x(0)$ and $x(t)$ are the positions evaluated at time 0 and time t respectively, and analogous definition holds for $p(0)$ and $p(t)$. Unlike in classical mechanics, where $c_{\mathrm{AB}}^{\mathrm{CL}}(t)$ is the only TCF that can be defined, in quantum mechanics, there are several equivalent ways to formulate it. One important TCF is the so-called Kubo TCF, $\tilde{C}_{\mathrm{AB}}(t)$,

$$\tilde{C}_{AB}(t) = \frac{1}{\beta}\int_0^\beta d\lambda Tr[e^{-(\beta-\lambda)\hat{H}}\hat{A}e^{-\lambda\hat{H}}e^{+i\hat{H}t/\hbar}\hat{B}e^{-i\hat{H}t/\hbar}]. \tag{2.64}$$

All the quantum TCF are related by simple formulae in Fourier space, but unlike others, $\tilde{C}_{\mathrm{AB}}(t)$ shares particular properties with the classical TCF. For position-dependent Hermitian operators, both TCF are real and even functions of time, satisfy $\tilde{C}_{\mathrm{AB}}(t) = \tilde{C}_{\mathrm{BA}}(t)$ [205], and their expressions of the fluctuation-dissipation theorem are isomorphic [206]. For these reasons, the classical TCF seems to be an approximation to $\tilde{C}_{\mathrm{AB}}(t)$ more than to any other quantum TCF or, in other words, $\tilde{C}_{\mathrm{AB}}(t)$ is the 'more classical' among the quantum TCF.

With these considerations in mind, Craig and Manolopoulos[205] suggested that choosing the fictitious mass equal to real particle mass in PIMD simulations ($m^{(k)} = m$ in Eq. 2.59), would generate classical trajectories with meaningful approximate quantum dynamical information. More specifically, the trajectories generated by the Hamiltonian 2.59 can be used to compute an approximation to the quantum Kubo TCF as

$$\tilde{C}_{AB}(t) \approx \lim_{P\to\infty} \langle AB(t)\rangle_P^{\mathrm{RP}}, \tag{2.65}$$

where

$$\langle AB(t)\rangle_P^{\mathrm{RP}} = \frac{1}{(2\pi\hbar)^P Q_P} \int\int d\mathbf{x}d\mathbf{p}\left[\frac{1}{P}\sum_{k=1}^{P} A(x^{(k)}(0))\right]\left[\frac{1}{P}\sum_{j=1}^{P} B(x^{(j)}(t))\right] e^{-\beta_P H_P(\mathbf{x}(0),\mathbf{p}(0))}, \tag{2.66}$$

and the abbreviate notations $(\{x^{(1)},\ldots,x^{(P)}\},\{p^{(1)},\ldots,p^{(P)}\}) = (\mathbf{x},\mathbf{p})$, $\int d\mathbf{x} = \int dx^{(1)}\ldots dx^{(P)}$, and $\int d\mathbf{p} = \int dp^{(1)}\ldots dp^{(P)}$ are used for clarity. The method was named ring polymer molecular dynamics (RPMD) since, after all, what it is being simulated are the dynamics of classical ring polymers. The symmetry considerations were not the only motivations to propose Eq. 2.65, and other properties supported the idea that it can be a reasonable short-time approximation to real time quantum dynamics. Specifically, RPMD gives the exact quantum mechanical correlation function at time zero, is exact in the short time limit for position and velocity correlation functions[205], gives the exact high-temperature limit, is exact for harmonic potentials when either $\hat{A}$ or $\hat{B}$ are a linear position-operator, and, arguably the most important property, satisfies the quantum mechanical equilibrium distribution and detailed balance condition.

Short after its foundation, RPMD was investigated as a tool to simulate vibrational spectra, and a particularly severe deficiency was put in evidence. It turns out that spectra, specially at low temperatures, present spurious peaks due to the fictitious dynamics of internal modes of the ring polymer[207–209]. Moreover, when one of these fictitious frequencies is close to a physical one, their coupling produces a splitting of the peak, which is completely unphysical, and it is known as the 'resonance problem'. The issue is less severe at high temperatures, since the lowest ring polymer internal frequencies increase with temperature and eventually is beyond the region of interest. A closely related method to RPMD is the so-called centroid molecular dynamics (CMD)[210–212]. In this case, the ansatz is to replace the classical potential energy function with an imaginary time centroid potential of mean force. Different from RPMD, CMD does not have the resonance problem, but unless simulated in curvilinear coordinates[213], it carries the 'curvature problem', which produces the high-frequency peaks to broaden and to red-shift at low-temperatures[209,214]. One decade later, Rossi *et al.* found a compromise between the two methods which fixes both the resonance and curvature method. The authors noted that there is a freedom of attaching a thermostat to the non-centroid degrees of freedom without violating any of the proven properties for RPMD[215], and proposed the so-called thermostated RPMD or TRPMD. Initially, a white noise Langevin

thermostat was used to 'damp' the fictitious internal oscillations. While an optimal choice of the friction coefficient solves the described problems, the method introduces an artificial broadening of the high-frequency peaks, which depending on the application at hand, can be relevant or not. More recently, on the same lines, and in order to minimize the broadining effect, a GLE thermostat was proposed where the shape, the width, and the shift of the peaks are used as merit functions in the optimization of the thermostat parameters[216]. The results obtained by this approach are quite satisfactory, and the broadening is significantly reduced but not completely removed since no real time coherence information is included in neither in RPMD nor in TRPMD. The authors also reported an unphysical blue-shift on the rotational and librational modes which, in most of the temperatures of interest, can be well captured by classical MD since NQE are expected to be small in this region of the spectrum.

The other established application of RPMD and related methods is the calculation of thermal reaction rates[217,218]. It has been shown to provide a good approximation to adiabatic rates and also, by combination with other path integral based methods, provides access to non-adiabatic rates in the full temperature range[219,220]. It is an attractive multidimensional theory that captures all the anharmonicity and recrossing effects together with tunneling and ZPE, and, when real time coherence does not play a major role, it provides estimates within a factor of 2 when compared to exact results for specific models[221,222]. RPMD has a deep connection with the instanton semi-classical theory[223] (see Section 2.4.6) when describing situations where tunneling contributions to the reaction rate are dominant. Remarkably, RPMD allows to define a quantum transition state theory (RPMD-TST)[218] which is, in fact, identical to the unique version of a quantum TST (the $\lim \to 0^+$ of the flux side correlation function) which has positive-definite quantum statistics[224,225], and gives the exact quantum rate in absence of recrossing[226]. Its main drawback is that usually thousand of trajectories are needed to get converged reaction rates[217,227]. Even though RPMD is among the most accurate available methods to compute approximate quantum chemical rates on multidimensional systems, the next section shows that under some well defined circumstances, there is a more efficient method which facilitates the rate calculation on costly *ab-initio* PES.

For more than a decade (T)RPMD was investigated and used as an *ad hoc* hypothesis until Hele and coworkers, starting from the quantum Liouville equation, and performing a truncation in the ring polymer normal-mode derivatives in the limit $P \to \infty$, arrived to a new type of Boltzmann conserving classical dynamics that yields quantum statistics called Matsubara dynamics[228]. Moreover, they showed that RPMD and CMD methods can be derived from Matsubara dynamics providing the theoretical background that was missing[229], being the latter its mean field approximation. The main shortcoming of this theory is that, due to the presence of a phase, it presents the 'sign problem', and therefore, it is not suitable for practical applications. Nevertheless, its theoretical importance is not diminished by that fact. It is worth to emphasize that even though Matsubara dynamics is a bridge which provides a first-principles derivation, and shows which terms have to be neglected in order to get the RPMD and CMD formulae, there is not a physical justification for those approximations to be made. Thus, the use of those methods are justified as much as by

the exact limits they fulfill, as by the empirical verification of their accuracy when more accurate results are available.

2.4.6 Approximate Quantum Time Dependent Properties II: Instanton Ring Polymer Rate Theory

As mentioned before, RPMD rate theory works exceptionally well in predicting thermal rates including tunneling and ZPE effects. However, long simulations are required in order to statistically converge RPMD results, which hampers its combination with *ab initio* PES. Since in the context of this thesis only reactions with well defined reactant and product states are studied, is it possible to compute thermal rates using more efficient methods that still capture NQE?

The simplest approach is the Eyring transition state theory (TST) where the rate constant, k, is approximated by

$$k_{\mathrm{TST}}(\beta) = A_{\mathrm{TST}}(\beta) e^{-\beta V^{\ddagger}}, \tag{2.67}$$

where A_{TST} is a prefactor that can be approximated by harmonic partition functions, and $V^{\ddagger}$ is the potential energy at the top of the barrier which divides reactants and products, known as transition state geometry. In most of the cases, it represents a first order saddle point of the PES, where the normal mode associated to the imaginary frequency (negative eigenvalue) describes the reactive coordinate. While this theory includes harmonic ZPE effects in the prefactor, its huge disadvantage is that it completely neglects tunneling effects.

Semiclassical instanton rate theory is a semiclassical theory that describes tunneling using classical dynamics in imaginary time[230,231], and can be seen as a generalization of TST[232,233]. Its thermal version was originally derived from the 'Im F' premise where the rate process is described by the decay of reactants into products by tunnelling through an energy barrier. The rate is expressed as the imaginary part of the complex system's free energy, F,[234]

$$k(\beta) \approx \frac{2}{\beta\hbar} \frac{\mathrm{Im}\, Q(\beta)}{\mathrm{Re}\, Q(\beta)} = -\frac{2}{\beta\hbar} \mathrm{Im}\, F \tag{2.68}$$

where $\mathrm{Im}\, Q(\beta)$ and $\mathrm{Re}\, Q(\beta)$ are the imaginary and real part of a 'complex partition function', respectively. It can be shown that $\mathrm{Re}\, Q(\beta)$ describes the reactant state and can be approximated by the reactant partition function, $Q_{\mathrm{R}}(\beta)$, while the imaginary part corresponds, in a loose sense, to the barrier region[235]. The usual way to evaluate the partition functions is by approximating the required integrals using the steepest descent (SD) method. This methods allows to approximate the integral of an exponential function without explicitly integrating it. In 1D it reads

$$\begin{aligned} \int_{-\infty}^{\infty} e^{-\beta S(x)/\hbar} dx &\approx \int_{-\infty}^{\infty} e^{-\beta [S(\bar{x}) + \frac{1}{2} S''(\bar{x})(x-\bar{x})^2]/\hbar} dx = \\ &= \sqrt{\frac{2\pi\hbar}{S''(\bar{x})}} e^{-\beta S(\bar{x})/\hbar} \end{aligned} \tag{2.69}$$

where $\bar{x}$ is a minimum of $S(x)$, and consequently $S^{'}(\bar{x}) = 0$ and $S^{''}(\bar{x}) > 0$. This approximation is based on the idea that the exponential of a function is governed by the region in which the function is minimal (See Fig. 6).

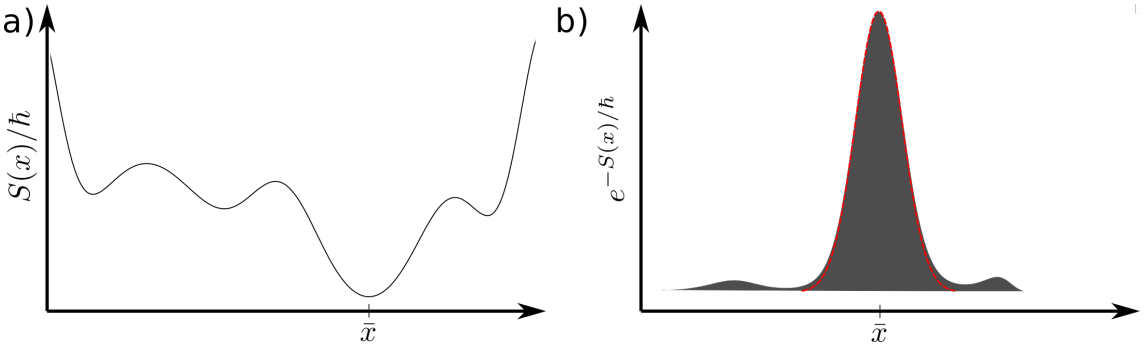

Figure 6: a) Function $S(x)/\hbar$ presents a minimum at $\bar{x}$. b) Function $e^{-S(x)/\hbar}$ presents a peak at $\bar{x}$. The integral, $\int dx e^{-S(x)/\hbar}$ (gray area) it is dominated by a Gaussian center at $\bar{x}$ (red dashed line)

A convenient way to evaluate both partition functions is to use the path integral expression given by the Eq. 2.54. The application of the SD method to compute $Q_{\mathrm{R}}(\beta)$ is straightforward, and leads to the harmonic approximation of the reactant partition function[236]. In order to apply the SD method to $\mathrm{Im}\,Q(\beta)$, the stationary points in the barrier region have to be found. Setting the gradient of Eq. 2.55 equal to zero gives,

$$m\frac{(x^{(k+1)} - x^{(k)}) - (x^{(k)} - x^{(k-1)})}{\beta_P^2\hbar^2} = V^{'}(x^{(k)}), \tag{2.70}$$

which can be seen as a finite-difference approximation to Newton's equation of motion with a time step $\beta_P\hbar$ in the inverted potential $-V(x)$. The reason behind this connection is two fold. First, as mentioned in section 2.4.3, the partition function can be thought as the time propagator in imaginary time. Second, since the ring polymer potential is a discretized version of the path action, Eq. 2.58, the stationary points of U_P describe paths with stationary action, i.e. classical paths, which can be described by Newton's equations. Considering classical pathways has both practical and conceptual advantages. On the practical side, one has linear scaling w.r.t. the system size and, at the conceptual level, the method gives trajectories that are easy to interpret and analyze, providing an intuitive view of the dynamical process.

A trivial solution of Eq. 2.70 is given by placing all the beads at the top of the barrier. However, there is a particular temperature called cross over temperature, T_{c}, at which the trivial solution becomes a second-order saddle point meaning that there is another solution where the positions of the beads are delocalized in imaginary time which leads to a smaller action, and therefore will be dominant in evaluating the integral by the SD method. This solution is called instanton pathway, instanton geometry, or solely instanton. It describes a periodic and stationary trajectory in imaginary time with time length $\beta\hbar$ which crosses the reaction barrier and folds back on itself.

Moreover, it represents a first-order saddle point in the ring polymer PES, where only the reactive coordinate has a negative curvature, and it is the trajectory with least action that connects reactant and products. Since each path has a weight proportional to $e^{-S_P/\hbar}$ (Eq. 2.54), the instanton represents the optimal tunneling pathway.

The task of finding the instanton pathways sounds simpler than it is. Indeed, it was among the main reasons that prevented instanton-based methods to be applied for multidimensional systems. The idea to replace functional integrals and continuous pathways by the discretized version of them, as it was described above, was first reported by Arnaldsson[237], and later popularized and extended by Richardson[223,236]. Moreover, it can also be derived from first principles by considering the semiclassical approximation to the imaginary time propagator and a series of steepest-descent approximations[236,238]. This theory is nowadays known as ring polymer instanton (RPI) rate theory, and it represents a practical method to evaluate thermal tunneling rates for multidimensional systems. Its efficiency relies in the fact that, instead of having to sum over all the paths as required by the exact theory, or perform complex functional derivatives to find stationary trajectories, the instanton trajectory can be found by using a first-order saddle point optimizer in the ring polymer potential.

When the instanton geometry is found, the $\mathrm{Im}\,Q(\beta)$ can be calculated and the rate computed. The negative mode is evaluated by an analytical continuation into the complex plane[239], the mode associated with the cyclic permutation of the beads by the Faddeev and Popov method[240], and the rest of the orthogonal modes by the SD approximation. The interested reader can find a step-by-step derivation elsewhere[235]. The reaction rate constant is then given by TST-like formula

$$k_{\mathrm{inst}}(\beta) = A_{\mathrm{inst}}(\beta) e^{-S_{\mathrm{inst}}(\beta)/\hbar}, \tag{2.71}$$

where the prefactor, A_{inst}, and the Euclidean action, S_{inst}, are evaluated at the instanton trajectory. The prefactor is a measure of the fluctuations around the instanton pathway, and its expression for indistinguishable particles in multidimensional systems will be given in chapter 3. Since the instanton rate becomes exact exact in the limit $\hbar \to 0$, it is belong to the so-called 'semiclassical' methods.

Above the T_c, TST with shallow tunneling corrections based on parabolic barrier approximations give highly accurate predictions[241,242], while below it, tunneling becomes dominant when compared to 'hop over the barrier' mechanism. For this reason, the regime of temperatures below T_c is called the deep-tunneling regime. Unlike the TST, the instanton pathway in multidimensional systems often does not follow the minimum energy pathways (MEP). Instead, it takes the path that extremize the action, which is usually shorter but has excursions across points of the PES with higher potential energy than the MEP. This effect is shown in the Fig. 7, and it is known as corner-cutting.

The applied approximations used to derive the RPI rate theory in multidimensional systems give rise to well-known limitations of the method. First, the instanton approach cannot be applied

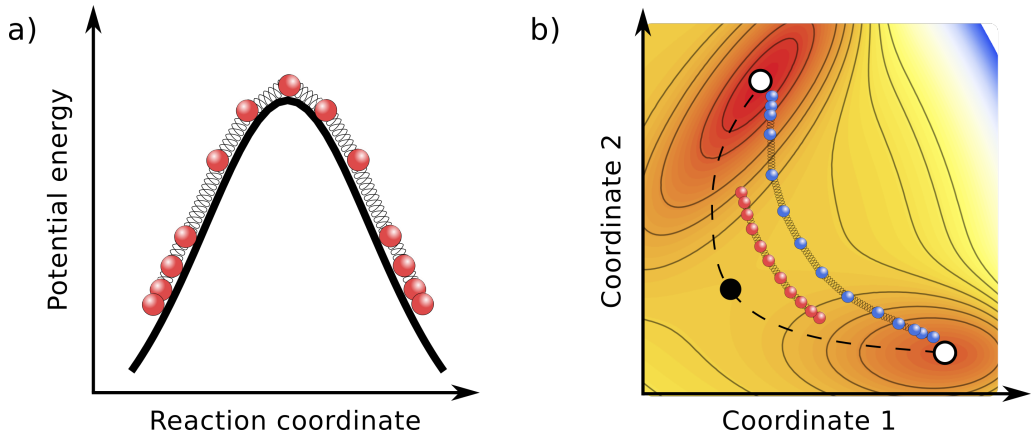

Figure 7: a) Instanton geometry along a 1D reaction coordinate. b) Instanton geometry along a 2D reaction coordinate. The MEP and isoenergetic curves are represented by dashed and solid lines, respectively. The black and white circles represent the transition state and local minima positions, respectively. Instanton pathways at two different temperatures are shown. The instanton depicted with red balls represents a higher temperature than the blue one. Both temperatures are below T_c. It can be seen that the lower the temperature, the more the instanton pathways departs from the MEP. Thus, the instanton takes a shorter path than the one specified by the MEP which is usually refereed as corner-cutting. Note that this effect is not possible in 1D.

to reactions where reactants and products states are not well defined as it happens in the case of proton transfer in solutions, reducing its domain of applicability. Second, no dynamic recrossing is considered. This is somewhat irrelevant since, in the deep tunneling regime, the recrossing tends normally to be non-significant. Finally, perpendicular modes along the reaction pathway are considered to be purely harmonic, which influences the fluctuation factor and reduces the method accuracy. However, because the full anharmonicity along the reaction pathway, which enters in the exponential part of the formula, is included, overall accurate results are obtained. RPI has been shown to predict rates within a factor of 5 for systems in which exact results are available, and to be more accurate than exact methods when the system size is too big and dimensional reduction techniques would be required[243–245]. Based on a similar instanton formulation, a closely related approach that describes coherent tunneling and allows to compute the ground state tunneling splittings of isolated molecules or clusters also exists, but it is not discussed here[246].

It is instructive to rewrite the 2.71 formula in the following way

$$k(\beta) = A_{\text{inst}} e^{-W(E_{\text{inst}})/\hbar} e^{-\beta E_{\text{inst}}/\hbar}, \tag{2.72}$$

where $E_{\text{inst}} = \frac{1}{\hbar}\frac{\partial S_{\text{inst}}}{\partial \beta}$, and $W(E_{\text{inst}}) = S_{\text{inst}} - \beta\hbar E_{\text{inst}} = \oint_{\text{inst}} dx\sqrt{2m(V(x) - E_{\text{inst}})}$. Eq. 2.72 shows that the energy of the most probable tunneling pathway, E_{inst}, is a result of a balance between the Boltzmann factor that favors low energy trajectories, and the microcanonical reaction probability, $e^{-W(E_{\text{inst}})/\hbar}$, which favors trajectories that have higher energies.

So far, the instanton approximation where the target quantity is the thermal rate, $k(\beta)$, has been discussed. However, there is another complementary and potentially more powerful theoretical

approach where the goal is to get the cumulative reaction probability, $P(E)$, i.e., the sum of the reaction transmission probabilities over all internal states of reactants and products at fixed energy. From it, the rate constant at a given a fixed energy, a.k.a. microcanonical rate, $k(E)$, can be easily computed as[247]

$$k(E) = \frac{1}{2\pi\hbar\tilde{Q}_r(E)} P(E), \tag{2.73}$$

where $\tilde{Q}_r(E)$ is the density of reactant states. This approach has several conceptual advantages. $P(E)$ can be directly related to reaction probabilities obtained from scattering calculations, and it can be Laplace transformed to get $k(\beta)$ at any temperature,

$$k(\beta) = \frac{1}{2\pi\hbar Q_r(\beta)} \int_0^{+\infty} P(E) e^{-\beta E} dE, \tag{2.74}$$

where $Q_r(\beta)$ is the reactant canonical partition function. Additionally, there are several situations where either a temperature cannot be defined, like reactions studied by astrochemists, or when a thermal equilibrium distribution of the reactants cannot be ensured, like reactions in the gas phase at very low pressures. In these cases, the microcanonical rate is the only meaningful rate. First reported by Miller in the 70s[232], and later proved by Althorpe to be equivalent to the thermal version of it[248], the semiclassical instanton approximation to $P(E)$ also considers periodic orbits with fix energy but variable path length. As occurred to other theories, it was hardly used in the community due to the lack of efficient algorithms to applied it. This deficiency is currently changing, and the proposed algorithms[249–251] seems to work, at least, for simple but realistic systems at not extreme temperatures. Still, much progress has to be made in this direction. At present, more robust and efficient algorithms have been developed for thermal instanton (see next chapter), and because of the systems treated in this thesis are within situations that can be tackled by it, unless specified, only the thermal theory will be considered.

In the next chapter, a description of the algorithm that makes possible calculations of tunneling rates for system up to ≈ 500 degrees of freedom and, together with its implementation in a package that deals with many types of other path integral based simulations is presented.

2.5 Summary

In this chapter, the theoretical background needed to carry out the work in this thesis was exposed. First, the many-body Hamiltonian was introduced together with the fundamental equations that need to be solved. Then, the Born-Oppenheimer approximation was presented, which allows to separate the electronic and nuclear problems, and to define the PES concept. Afterward, different strategies to tackle the electronic problem were discussed. Particular attention was given to the DFA method since it represents the method mostly used over this thesis. Having 'solved' the electronic problem, and having a practical method to evaluate the electronic energy and forces

for a particular nuclear configuration, the nuclear problem was addressed. For this purpose, and acknowledging the role played by the temperature, the nuclear problem was reformulated in the framework of statistical mechanics. Two cases were considered, namely, classical and quantum distinguishable nuclei. Practical methods to evaluate ensemble averages of time-independent observables were examined making emphasis on the MD and PIMD methods, and its connection through the 'classical isomorphism'. Several approaches to reduce the computational cost of the PIMD were also discussed, and a new approximation to simulate weakly bounded systems was presented. Finally, the calculation of time dependent properties when the nuclei are studied as quantum particles was discussed. Since no exact methods exist that can compute them for more than a few degrees of freedom, two approximations were introduced with their benefits and drawbacks. The first one is the (T)RPMD method that will be used to compute vibrational spectra, and the second one is the RPI rate theory that will be applied to compute tunneling rates.

Chapter 3

Instanton Calculations for High-Dimensional Systems

The basics of the thermal RPI method have been reported for more than ten years, but still nowadays, only a handful of groups perform instanton calculations. In the author's opinion, two elements can help to popularize this powerful method. First, an easy-to-use, open-source, efficient, and general implementation of it, and second, a set of guidelines that ease the introduction to researchers who are not familiar with the methodology. While some recommendations have been reported, they are too general or are scattered in pieces across the literature[236,243,252,253]. It is expected that this chapter, and the corresponding RPI implementation that is described in it, work as a catalyst and triggers the use of the RPI in the community. Even though only rate calculations are discussed, the same infrastructure can be used to obtained ground state tunneling splittings as well[236].

3.1 Thermal Ring Polymer Instanton Rate

The multidimensional version of the Euclidean action as defined in Eq. 2.55 and 2.58 and expressed in mass scaled coordinates, $y_i = \sqrt{m_i}x_i$, reads

$$S(\mathbf{y})/\beta_P\hbar = U_P(\mathbf{y}) = \sum_{i=1}^{f}\sum_{k=1}^{P}\frac{1}{2}\omega_P^2(y_i^{(k+1)} - y_i^{(k)})^2 + \sum_{k=1}^{P}V(y_1^{(k)},\ldots,y_f^{(k)}), \tag{3.1}$$

where $y_i^{(k)}$ corresponds to the mass scaled coordinates of the i-th degree of freedom of the k-th bead, f is the number of physical degrees of freedom for each bead, $\mathbf{y} = \{y_1^{(1)}, y_2^{(1)}, y_3^{(1)}\ldots, y_{f-2}^{(P)}, y_{f-1}^{(P)}, y_f^{(P)}\}$, and as before, $\omega_P = (\beta_P\hbar)^{-1}$. The corresponding Hessian matrix in mass-scaled coordinates, i.e dynamical matrix, D, that will be needed to perform the SD approximation, is given by

$$\begin{aligned} D_{i,i'}^{k,k'} &= \frac{\partial^2 U_P(\mathbf{y})}{\partial y_i^k \partial y_{i'}^{k'}} \\ &= \delta_{i,i'}\omega_P^2\big[-\delta_{k+1,k'} - \delta_{k-1,k'} + 2\delta_{k,k'}\big] + \delta_{k,k'}\frac{\partial^2 V(y_1^k,\ldots,y_f^k)}{\partial y_i^k \partial y_{i'}^{k'}}, \end{aligned} \tag{3.2}$$

and it has the following sparse structure,

$$D = \omega_P^2 \begin{pmatrix} A^{(1)} & -\mathbf{1} & \mathbf{0} & \cdots & -\mathbf{1} \\ -\mathbf{1} & A^{(2)} & -\mathbf{1} & \cdots & \mathbf{0} \\ \mathbf{0} & -\mathbf{1} & A^{(3)} & \cdots & \mathbf{0} \\ \vdots & \vdots & \vdots & \ddots & \vdots \\ \mathbf{0} & \mathbf{0} & \cdots & A^{(P-1)} & -\mathbf{1} \\ -\mathbf{1} & \mathbf{0} & \cdots & -\mathbf{1} & A^{(P)} \end{pmatrix}.$$

In the previous description, $\mathbf{0}$ and $\mathbf{1}$ are the zero matrix and the identity matrix of size $f \times f$, respectively, and $A^{(k)} = D^{(k)}/\omega_P^2 + 2 \times \mathbf{1}$, where $D^{(k)}$ corresponds to the mass-weighted Hessian matrix of the replica k.

The instanton reaction rate given by Eq. 2.71 in multidimensional systems can now be expressed as,

$$k_{\text{inst}}(\beta) Q_r(\beta) = \frac{1}{\beta_P \hbar} \sqrt{\frac{B_P(\bar{\mathbf{y}})}{2\pi\beta_P\hbar^2}} Q_{\text{trans}} Q_{\text{rot}} Q_{\text{vib}} e^{-S(\bar{\mathbf{y}})/\hbar}, \tag{3.3}$$

where

$$B_P(\bar{\mathbf{y}}) = \sum_{i=1}^{f} \sum_{k=1}^{P} (\bar{y}_i^{k+1} - \bar{y}_i^k)^2, \tag{3.4}$$

$$Q_{\text{rot}} = \sqrt{\frac{8\pi \det I}{\beta_P^3 \hbar^6}}, \tag{3.5}$$

$$Q_{\text{trans}} = \left(\frac{P \sum_{i=1}^{f/3} m_i}{2\pi\beta_P\hbar^2} \right)^{3/2}, \tag{3.6}$$

and

$$Q_{\text{vib}} = \frac{1}{\beta_P \hbar |\eta_1|} \prod_{k=f_0+3}^{Pf} \frac{1}{\beta_P \hbar \eta_k}. \tag{3.7}$$

The $\bar{\mathbf{y}}$ refers to the instanton optimized geometry. I, Q_{rot} and Q_{trans} are the moment of inertia tensor, classical rotational partition function, and classical translational partition function of the ring polymer considered as a 'super-molecule' with $P \times f/3$ atoms, and η_k are the $P \times f$ eigenvalues of D. The modes associated with translational and rotational invariance of the 'super-molecule', $\eta_3 \dots \eta_{f_0+2}$, give rise to f_0 zero eigenvalues and are accounted in Q_{rot} and Q_{trans}. The eigenvalue corresponding to the mode describing the cyclic permutation of the beads, η_2, is also zero, and its contribution is described by the B_P factor[240]. Finally, the negative eigenvalue, η_1, and all the positive ones, $\eta_{f_0+3} \dots \eta_{Pf}$, are considered in the product that appears in Q_{vib}. The reactant partition function, $Q_r(\beta)$, is evaluated similarly as a product of translation, rotational and harmonic vibrational partition functions considering that the ring polymer is collapsed at the reactant geometry. It is important to evaluate the latter with the same amount of replicas used to compute

the instanton partition function in order to benefit from error cancellation. Similar but equivalent expressions can be found elsewhere [243,252].

Finally, combining Eq. 3.3 to 3.7, we get the expression for the rate,

$$k_{\mathrm{inst}}(\beta)Q_r(\beta) = \frac{1}{\beta_P\hbar}\sqrt{\frac{8\pi\det I}{\beta_P^3\hbar^6}}\left(\frac{P\sum_{i=1}^{f/3} m_i}{2\pi\beta_P\hbar^2}\right)^{3/2}\sqrt{\frac{B_P(\bar{\mathbf{y}})}{2\pi\beta_P\hbar^2}}\prod_k{}' \frac{1}{\beta_P\hbar|\eta_k|}e^{-S(\bar{\mathbf{y}})/\hbar}, \tag{3.8}$$

where the prime indicates that the product is taken over all modes except the ones with zero eigenvalue.

3.2 i-PI program

The i-PI program is an open software written in Python that performs atomistic simulations within the BOA [253,254]. Initially designed to perform PIMD simulations, the current scope has been broadened towards becoming a universal force engine. In this sense, not only PIMD and related methods are available, but also several other classes of algorithms like geometry optimization or advanced harmonic analysis [255].

i-PI takes the most advantage of the BOA and fully decouples the nuclear dynamics from the solution of the electronic problem. In this sense, i-PI takes care exclusively of the nuclear displacement under the algorithm of choice, and the task of evaluating the energy and forces for a given nuclear configuration is left to specialized *ab initio* or force-field external codes, usually referred as client codes. A suitable interface that deals with the required communication between i-PI and the client codes achieves this purpose. Among others, FHI-AIMS [156],CP2K [256], DFTB+ [257], Lammps [258] and Siesta [259] have a working interface to i-PI and can be used out-of-the-box. Particularly tailored to couple with *ab initio* codes, i-PI is designed considering that the bottleneck of the simulations emerges from the evaluation of the energy and forces by the external code and that the nuclear evolution adds a negligible computational overhead. Thus, in several places, the code readability prevails over code efficiency.

In Fig. 16, a simplified representation of the i-PI architecture is shown. The core element in i-PI is the *system* class which includes four subclasses:

- *initialize* class: sets up the number of system replicas (beads), the atomic positions, the simulation cell, and other required quantities that defines the system under consideration.
- *ensemble* class: handles the thermodynamic variables, like temperature or pressure, which determine the ensemble that is going to be simulated and any potential energy bias that may be present.
- *forces* class: it connects to the *forcefield* class (described later) and handles how the different potential and force components should be combined in order to get the system energetics and the total atomic forces. This approach is specially suitable when multiple time steps or

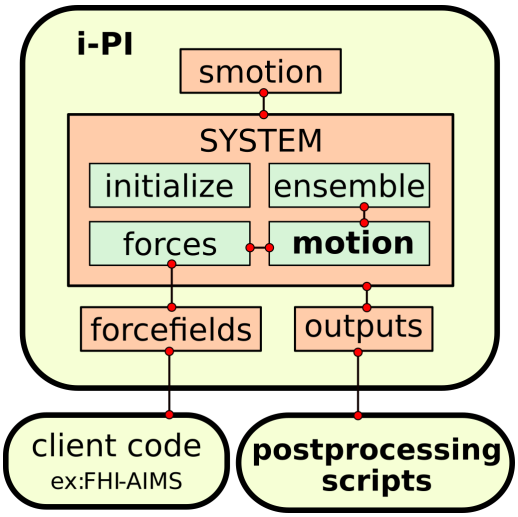

Figure 8: A simplified schematic representation of the i-PI architecture. Rounded yellow boxes identify programs while orange and green rectangle boxes represent python classes. The circle-ended-lines denote, in a broad sense, information exchange. The *motion* class and the postprocessing script are in bold representing the main areas where the new devolpment has taken place. Figure adapted from Ref.[253].

ring polymer contraction like algorithm are used, and the final energies and forces are linear combination of different force and energy 'pieces'.

- *motion* class: handles the actual algorithm that is going to be used to evolve the nuclear positions, like Monte Carlo, MD, PIMD, energy optimization, etc. It is tightly bounded to the *forces* and *ensemble* classes which provide the required information when needed.

The class *forcefields* should not be confused with the *force* class described earlier. Its main tasks are to receive atomic coordinates, communicate them to the external code, and, to receive from the client code the energies, forces, and other possible required quantities, like dipole or stress tensor. When performing path integral simulations, this class allows having as many clients codes as number of beads, making it appealing for its use in today's high-performance computers. Other two important classes are *outputs* and *smotion*. The first one controls which information is going to be saved in output files and how, while the second one allows performing replica exchange simulations by swapping ensembles among parallel systems[180] or metadynamics[181] simulations by updating the ensemble bias.

A minimalistic and simplified code that represents the code flow follows,

```
system.initialize()
while nstep < total_steps:
    for system in system_list:
        system.step()
    smotion.step()
    output.write()
```

where 'nstep' is an integer that keeps track of the step number, 'total_steps' is another integer that specifies the number of total steps, 'system_list' is a list that contains all the simulated systems, and python syntax has been assumed.

An interesting and advanced feature of i-PI are the so-called dependencies. For the sake of this explanation lets consider that the force, f, depends only on the atomic position, x, and not in the velocity, v. The velocity verlet algorithm which propagates the particle with mass, m, from the initial state $\{x(t), v(t)\}$ to the final state $\{x(t+dt), v(t+dt)\}$ reads[91]

$$v(t+0.5dt) = v(t) + 0.5\frac{f(t)}{m}dt$$
$$x(t+dt) = x(t) + v(t+0.5dt)dt$$
$$\text{compute new forces}$$
$$v(t+dt) = v(t+0.5dt) + 0.5\frac{f(t+dt)}{m}dt.$$

The dependency infrastructure removes the need to call the force calculation on the third line explicitly. More specifically, when the force at time $t+dt$ in line four is needed, the program checks if any of the dependencies, in this case only the position, have changed or not. If the codes detects that at least one of them has changed, the force calculation is automatically triggered to get the updated value. This architecture represents a curse for the unfamiliar developer that would face a steep learning curve, but at the same time, it is a blessing for the familiarized one, who only has to focus on the algorithms because all the required quantities are automatically computed upon necessity.

3.3 Instanton implementation and practical guidelines

The instanton implementation coded in the frame of this thesis required to create a new *motion* class and the corresponding postprocessing scripts since the i-PI infrastructure takes care of the rest of the tasks. Most importantly, the new implementation inherits from i-PI the ability to communicate with several different clients, avoiding the burden of making a specific implementation for each of those codes. For this purpose, the optimization routines were revised and improved, since, after all, an instanton calculation is a geometry optimization in an extended phase space. A global description of the procedure is presented below, and a detailed discussion of the involved steps follows later.

In Fig. 9 a diagram of the calculation workflow is presented. First of all, since the instanton folds back on itself, the optimization can be carried out with only half of the replicas. The starting geometry of the half ring polymer is normally, but not necessarily, generated by elongating the transition state geometry along the mode with imaginary frequency. The starting temperature is approx. 10% below T_c. This choice ensures a fast convergence, since the instanton pathway does

not depart too much from the transition state at that temperature, and only a reduced amount of beads is required. The optimization is accomplished by quasi-Newton methods [260], which are usually preferred in the cases where a good Hessian approximation is available. After converging the first optimization, the temperature can be further reduced, and a new optimization should be started. As the temperature descends, an increased number of beads will be needed to avoid numerical instabilities in the optimization algorithm. In those cases, the previous instanton geometry and approximate Hessian matrix can be interpolated to the desired new amount of beads (See for example, supporting information in Ref. 261). It is important to stress that no recalculation of the Hessian matrix is required at this point, which would otherwise make the calculation unusable for real applications due to the required computational cost. The procedure continues until the target temperature is reached. The standard procedure requires at this point to compute the instanton Hessian, which, as shown in Eq. 3.2, requires the calculation of the physical Hessian matrix for each replica, and only afterwards, the calculation of the rate using Eq. 3.8. In principle, one should increase the number of beads, re-optimize the instanton at the same temperature, compute the costly instanton Hessian again, and finally get the new rate. Then, both rates are compared to check for convergence, and the last step is repeated if needed. A simple way to avoid more than one Hessian calculation is to rely on calculations on similar systems where a cheap potential is available, and a convergence analysis provides the required number of beads that guarantees the desired accuracy.

Before starting a deeper discussion about each of the steps one by one, there is one caveat to mention. All the suggestions are tailored for *ab initio* calculations where the computational cost is an important variable to consider and can be crucial in the decision of performing this type of simulation or not. The idea of "haste makes waste" will be used here [a]. Accordingly, the advice provided in the next sections will be rather conservative but deliver a predictable performance. Unless specified, all the recommended algorithms are coded and available in i-PI.

The guidelines are based on the experience gained from investigating a small but representative set of the hydrogen tunneling reactions, where the description of the underlying PES, the dimensionality, the number of tunneling particles, the shape of the barrier, and the nature of the reaction (intramolecular vs. intermolecular) are explored. Details of such calculations with the description of the systems under consideration can be found in the Appendix.

3.3.1 Initial guess

In most of the cases, it is desirable to have the transition state geometry associated to the reaction under study. Its imaginary frequency, ω_{TS}, can be used to estimate the cross over temperature as $T_{\mathrm{c}} = \hbar\omega_{\mathrm{TS}}/2\pi k_{\mathrm{B}}$, and its geometry can help to build a good initial guess. There are several algorithms to find the transition state geometry, among others, the dimer method [262], the nudge elastic band [263,264] and the string method [265,266]. As mentioned earlier, at T_c the instanton collapses into the transition state geometry, and only below that temperature the springs are sufficiently

[a] The reader might be familiar with the similar phrase "*dress me slowly I am in a hurry*".

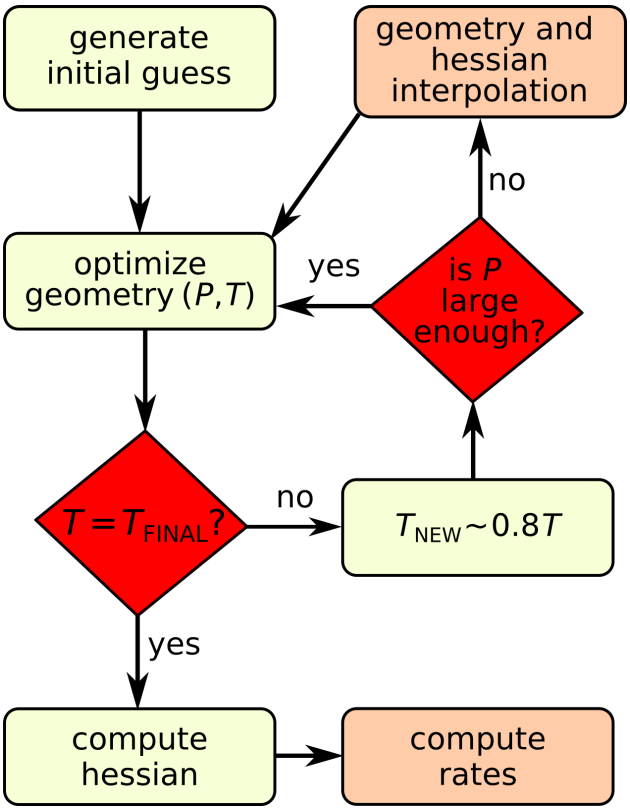

Figure 9: Schematic representation of the workflow for an instanton calculation. The rounded boxes refers to actions or calculations, while the red diamonds to logical decisions. Yellow boxes are performed automatically by the code, and orange boxes require the use of an external script provided with the code. P and T refer to the number of replicas and temperature, respectively.

weak such that the ring polymer finds favorable to stretch over the barrier (Fig. 7). For this reason, it is not surprising that the elongation of the ring polymer geometry along the unstable mode represents an excellent initial guess. The beads can be distributed equidistant or by a cosine function[252] with similar results. The recommended value for total elongation between the extremes of the half ring polymer is 0.1 a.u. Slightly smaller or greater values can be used as well, but a large deviation from it can create either a pretty extended geometry, which will be either too far from the solution, or a geometry that is too close to the transition state geometry which also represents a stationary point, albeit not the desired one. Another important piece is the initial instanton Hessian matrix. Ideally, one should compute the Hessian for all the replicas of the initial geometry, but experience has shown that just assigning to all beads the transition state Hessian matrix does a reasonable job too. Since the transition state Hessian is needed to estimate T_c, and decide if the tunneling is going to be relevant at the target temperature, this choice does not entail any additional calculation. A generic Hessian, like the proposed in Ref. 267, 268, may represent a good starting point, but it has not been tested for this work. In all tested cases, starting the optimization at a temperature 20K below T_c with 20 beads [b] guarantees convergence in less than

[b] The optimization is performed for half of the ring polymer, but always the total number of beads is mentioned to avoid confusion.

ten steps.

3.3.2 Optimization algorithm

As a consequence of the fact that at any temperature there is available a good initial guess for the geometry, and a reasonable approximation to the Hessian, a simple mode following algorithm proposed by Nichols[269] and modified by Richardson[270] works exceptionally well in this context. The reader should be aware that this represents a clear distinction from more standard scenarios where no such initial information is available[264,271]. Nichols' idea is straightforward to understand. At each step of the optimization, the gradient is computed, and the ring polymer mass-weighted Hessian is diagonalized. Next, the component of the gradient along the eigenvector with negative curvature is inverted to obtain the step direction, and the step length is chosen depending on the sign and magnitude of the lowest two eigenvalues. This procedure ensures that the new step is upwards in energy along the imaginary mode and downwards w.r.t all the modes orthogonal to it. Additionally, as a typical safety measure, the maximum step is restricted to 0.1-0.2 a.u. with little impact on the optimization performance. Convergence is considered to be achieved when the maximum force and step component are below 1×10^{-4} a.u. and 1×10^{-3} a.u., respectively. Finally, the Hessian is updated along the optimization according to the Powell formula[272].

Other methods have been considered in the context of instanton optimization such as the dimer method, the partitioned-rational function optimizer and the Newton-Raphson (NR) method. In Ref. 252, the authors found that the NR algorithm performed much better than the other algorithms in all the tested cases. However, NR is designed to converge quadratically to the closest stationary point, which is not always a first-order one. It was suggested that after the converged geometry is reached, and the final Hessian recomputed, the eigenvalue spectrum will confirm whether the desired stationary point is obtained or not. In cases where expensive potentials are used, this is a cost that must be avoided, and it is preferred a slightly less efficient algorithm which ensures the correct solution. Consequently, the mode following algorithm mentioned previously is recommended. Nonetheless, when an optimized geometry has been found, and a further re-optimization with an increased number of beads at the same temperature is needed, the NR method should be adopted since it will require a smaller amount of steps, and it converges to the correct solution.

As mentioned earlier, only half of the ring polymer has to be optimized. The corresponding Hessian is a banded matrix equivalent to the one in Eq. 3.2 but without the non-diagonal blocks. For intermediate systems sizes, the banded nature helps the diagonalization required during the calculation, and algorithms tailored for banded matrices are helpful. However, for systems with more than 100 atoms and 200 replicas, this task may last more than 1 hour if it is not appropriately parallelized[c]. As i-PI works with the premise that the algorithms which evolve the nuclear positions have an insignificant cost in comparison to the force evaluation, this represents a prob-

[c] In an desktop computer with a Intel(R) Core(TM) i7-7820HQ CPU @ 2.90GHz and using numpy (Python 3.7.3, Anaconda distribution), the diagonalization of a matrix corresponding to a system with 90 atoms and 100 beads lasts approx. 64 minutes.

lem that had to be addressed. Noting that actually only the lowest two eigenvalues and associated eigenvectors are needed to project the gradient and compute the next displacement vector, a modified Nichols algorithm, where a Lanczos-type iterative method replaces the unnecessary full matrix diagonalization task, has been also implemented.

3.3.3 Cooling procedure

Practical guidelines tested in the model systems are now described. These guidelines are not optimal for each individual system but rather optimal for the full set (see Appendix). More importantly, it has a predictable efficiency, expressed in the number of steps, which is expected to help other researches estimate the required computational cost before performing any calculation.

The recommend optimization path starting from the transition state geometry down to $0.2 \times T_c$ follows:

1. Converge the first instanton geometry at $T_{\text{initial}} = T_c - 20K$ with $P = 20$.
2. Start the new optimization at $T_{\text{new}} = 0.80 \times T_{\text{old}}$, and with an increased number of beads, such that, $P \times T_{\text{new}}/T_c \approx 20$.
3. Continue until the target temperature is reached.

The proposed route along the '$P-T$' plane resulted for all tested cases in optimizations shorter than twenty steps, and in most of the cases, shorter than ten steps. Other routes are also possible, but either they have a higher computational cost, or they admit a less predictable efficiency which may produce optimization failures in some cases (see Fig. 10).

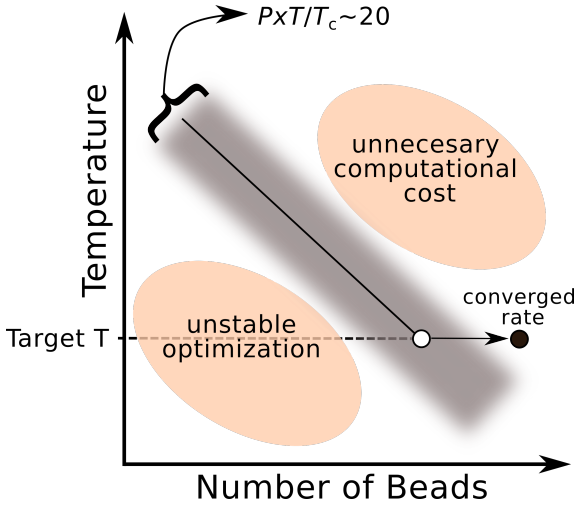

Figure 10: Graphical suggested optimization pathway during an instanton rate calculation. The gray area represents the path were a trade-off between the number of beads required to have an stable optimization, and a minimal computational cost is assured. After the optimization reaches the target temperature, white circle, additional optimization with more beads may be required to achieve the desired accuracy for the final reaction rate.

3.3.4 Interpolation

The geometry and Hessian interpolation required to restart a calculation with an increased amount of replicas presents no difficulties. Spline interpolations procedures and Fourier interpolation based on the RPC scheme[261] were tested. Both approaches show comparable optimization performance, the latter being implemented in i-PI and only marginally superior.

3.3.5 Number of Force Evaluations

Because of the classical nature of the instanton trajectory, the replicas tend to aggregate at the turning points of the periodic orbit, causing that the physical potential is evaluated several times at similar structures. Methods that try to reduce this redundancy could potentially reduce the computational cost considerably. By rederiving the instanton formulae using a non-uniform imaginary time discretization, Rommer *et al.* obtained an instanton formulation which produces a more uniform sampling of the imaginary time axes and, in principle, requires a reduced amount of replicas[273]. Unfortunately, in order to obtain converged rates, the number of replicas has to be increased up to a similar value as the one required by the standard methodology cutting most of the efficiency gain. A simpler numerical based method was implemented in i-PI to address this issue. At each step of the optimization, the potential energy of contiguous replicas is compared. Only replicas whose energy difference is above a certain threshold are computed in the next step, and the rest are obtained by spline interpolation. Careful tests have to be performed, but a threshold value of 4 meV represents a rather conservative choice and delivers an efficiency gain up to a factor of 10 at low temperatures. Similar interpolation ideas have also been suggested in literature[274].

3.3.6 Rate Evaluation and Convergence

After the converged instanton geometry is obtained at the target temperature, the Hessian approximation at hand cannot be used directly to compute the rate, and a new one has to be computed. Until this point, only one Hessian corresponding to the transition state geometry has been explicitly computed. Since the calculation of the ring polymer Hessian is by far the most computationally demanding part, one would like to do it only once with the required number of beads, especially when working with costly PES. In the appendix, convergence tests at different temperatures for all the tested systems are provided. Overall, for $P \times T/T_c \approx 20$ an error up to a factor of 2 can be expected, while for $P \times T/T_c \approx 40$ the error goes down to 10 % or below in all cases. Additionally, there is no necessity to compute the physical Hessian matrix for all the replicas, and similar interpolation strategies, that rely on in the proximity of geometries, can be adopted.

Last but not least, comes the diagonalization of the full ring polymer Hessian needed to compute the fluctuation factor. Since it is not banded, this task can be problematic for systems above 100 atoms at low temperatures where more than 256 beads would be needed. The straightforward solution is to apply a diagonalization program that can be parallelized in several CPUs. A small repository that contains scripts and examples that make possible to perform parallel matrix diago-

nalization in python using the 'Eigenvalue SoLvers for Petaflop-Applications' (ELPA) [275] has been created for this purpose [276]. An alternative solution has recently been reported by Pierre *et al.* where a 'divide and conquer approach' was proposed [277]. The authors used standard semiclassical relations to reformulate the problem in such a way that the instanton pathway is divided into several segments, and a smaller matrix diagonalization has to be carried out for each of those. The method has been tested only for rather small systems, and even though there is no reason to believe it will not work for big systems, its performance has still to be proved.

3.3.7 Other Considerations

Some other considerations for particular situations are worth documenting:

- When dealing with systems of more than 50 atoms, it is usually the case that not all the atoms have a significant displacement along the instanton pathway. It is then possible to fix those degrees of freedom in order to reduce the size of the problem and help the optimization. Later, the constraint can be released, and the full-dimensional calculation performed. The only caveat is that all the atoms which are clearly relevant to the tunneling pathway have to be included. Normally this selection presents no difficulties.

- it is desirable in many cases to re-evaluate the instanton action at a higher level of theory after the optimization is finished since its accuracy has an exponential impact on the rate [278]. The i-PI infrastructure makes this procedure trivial just by connecting a different client code, or the same one with different internal settings.

- The above guidelines assume that the transition state geometry is a first-order saddle point. For second-order saddle points, like the *trans*→*trans* reaction for the gas phase porphycene molecule or the DHT in the formic acid dimer, a slight modification has to be made. At sufficiently low temperature the instanton pathway stretches enough along the reactive coordinate and it becomes a first-order saddle point. Hence, the question is how to reach such temperature starting from T_c and an initial geometry guess close to the transition state geometry. One possible solution is to modify the Nichols' algorithm to search for second-order saddle points [d], and apply the cooling procedure described above until the second negative frequency disappears. Afterwards, the optimization continues with the standard algorithm. Tests on 2D models and the reaction in the porphycene molecule mentioned before showed the convenience of this approach in comparison to others where the optimization starts directly at low temperatures.

3.4 Summary

A new RPI rate theory implementation inside the universal force engine i-PI has been described, and it can be already used in combination with dozens of *ab initio* codes. The implementation

[d] In the notation of the original paper [269] one has to take $\alpha = 1$ and $\lambda = (h_2 + h_3)/4$.

includes several improvements which reduce the amount of force evaluations with no accuracy reduction, and make possible RPI calculations for the biggest systems that make sense to compute within this theory in the field of chemical reactions. Practical guidelines were also presented and discussed. This effort represents a major step towards the adoption of RPI rate calculations as routine simulations across the community.

Chapter 4

Summary

The main results of this thesis are presented now in a coherent manner rather than a chronological one. Methodological details and secondary outcomes are left out of this summary, and can be found in the corresponding manuscripts presented in the following chapter. The main goal of this thesis is the study of quantum equilibrium and dynamical properties of molecules on metallic surfaces where hydrogen bonds and hydrogen transfer events are relevant. The main simulation techniques were described in the previous chapters and all rely on the BOA allowing to resolve the electronic and nuclear problems separately. DFA was used to tackle the first one, while imaginary time path integral based techniques were employed to deal with the second. To perform the simulations FHI-AIMS[156] and i-PI[253] were used.

Paper I describes an efficient implementation to compute tunneling rates using the RPI rate theory, and it has been discussed in detail in chapter 3. The next four papers present a systematic study of the hydrogen dynamics of the porphycene molecule in the gas phase (**Paper II** and **III**) and adsorbed on metal surfaces (**Paper IV** and **V**). Lastly, **Paper VI** broadens the scope and presents a novel approximation to include NQE on molecules on surfaces, and applies it to study the water dissociation on Pt(221).

Vibrational spectroscopic techniques such as IR and Raman spectroscopy are useful tools to study nuclear dynamics. Particularly, the strength of HBs are often characterized by the position and width of the corresponding stretching band. For this reason, in **Paper II**, a systematic study of the porphycene molecule vibrational spectra was performed starting from the harmonic approximation, followed by MD simulations, which capture the anharmonicity of the PES and the intermode coupling at finite temperature, and ultimately, TRPMD simulations, which approximately include dynamical NQE, as dicussed in section 2.4. In all cases, electronic energies, atomic forces, and dipole moments were obtained from the DFA using the B3LYP XC functional augmented by vdW dispersion corrections[147].

The high-frequency part of the IR spectra is shown in Figure 11a. The agreement between experiments and theoretical predictions improves when the complexity of the simulation is increased. It is interesting to note that the harmonic approximation, and anharmonic classical-nuclei dynam-

ics give a poor approximation to the peak position and broadening, which proves the importance of the anharmonic nuclear quantum dynamics. The results of these simulations resolved the long standing question about the localization and correct interpretation of the NH stretching band discussed in chapter 1.

The simulated IR spectra allowed an in-depth analysis of the fine structure of the NH stretching band. The application of a simple adiabatic model that couples a low-frequency with a high-frequency mode provides general and interesting insights[279] (see also supporting information in **Paper II**). The principal model parameters are the high-frequency (Ω) and the low-frequency (ω) values, as well as the strength of the coupling between them (α). As shown in Fig. 11b, the agreement between the model and the TRPMD IR spectra is satisfactory for 2680 $cm^{-1} < \omega <$ 2750 cm^{-1} and 100 $cm^{-1} < \Omega <$ 115 cm^{-1}. This model has no predictive capacity since a prior simulation has to be performed to fit the model parameters. Nevertheless, it helps to illustrate an important point: the fine structure of the NH stretch band most probably stems from the coupling of the high-frequency modes with the low frequencies ones around 100 cm^{-1}. As we will see later, these couplings are crucial to explain the temperature dependence of the DHT rates.

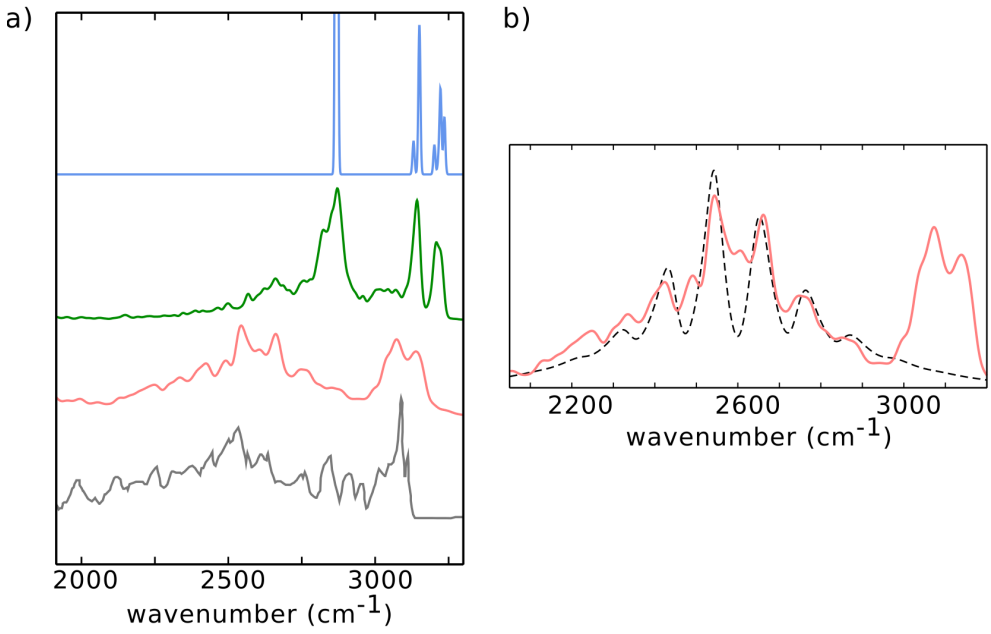

Figure 11: a) High-frequency region of IR spectra of porphycene molecule. From top to bottom: harmonic approximation, clasical MD simulations at 290 K, TRPMD simulations at 290K and experimental measurement in a KBr matrix at 290K. See details in methods section in **Paper II**. b) TRPMD simulations (red lines) superimposed with the adiabatic model results with $\Omega = 110 cm^{-1}$ and $\omega = 2745 cm^{-1}$ (dasehd black lines).

In **Paper III**, the temperature dependence of the vibrational spectra of porphycene molecule was studied. For this purpose, and in order to obtain converged spectra needed to observe small temperature differences, non-linear fitting techniques, commonly known under the name of machine

learning, were used. They allowed to obtain cheap and yet reliable approximations of the PES and the dipole surface. The PES was fitted using high-dimensional neural networks (HDNNP) developed by Behler and Parrinello[280], and the dipole surface using Kernel Ridge Regression (KRR)[281]. The combination of those techniques made it possible to perform several nanoseconds of TRPMD simulations from 400K down to 50K. When considering the required amount of beads at each temperature, the total simulation time amounts to approximately 0.5 microseconds, which is beyond the current capabilities of conventional *ab initio* simulations.

Once again, the focus is set at the NH stretch band region which encodes the intriguing hydrogen dynamics of this molecule. Its temperature dependence obtained by TRPMD and classical MD simulations is shown in Fig. 12. The results of the simulations with quantum-nuclei appear almost 300 cm^{-1} red-shifted w.r.t. to the simulations with classical-nuclei. This behavior is not surprising, and it is mainly explained by ZPE effects. The nuclear quantum fluctuations of high-frequency modes correspond to approximately 2000 K which is much larger than the thermal energy available in classical simulations at the temperatures considered. Therefore, in the quantum description, high-frequency modes like the NH one sample areas of the PES that are further away from the global minimum in comparison to the ones sampled by the classical simulations. Those areas exhibit a high degree of anharmonicity, which generates the observed red-shift.

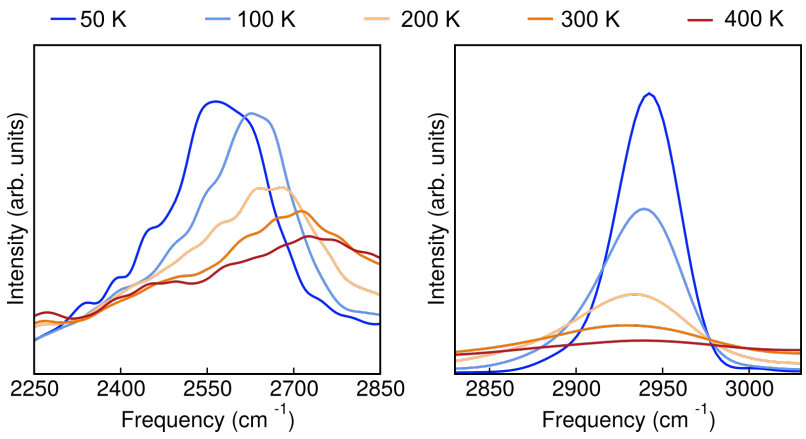

Figure 12: Vibrational density of states obtained by TRPMD (left) and classical MD (right) simulations.

More intriguing is the temperature dependence of the peak positions. While the classical simulations predict a red-shift with an increase of the temperature, the TRPMD simulations predict a blue-shift. The classical outcome is a conventional and well-established result for Morse-like anharmonic potentials. The more thermal energy the system has, the more anharmonic areas of the PES are sampled, and consequently, the further the peak is red-shifted. When the quantum nature of the nuclei is considered, one would expect that a temperature increase of 300K has a negligible effect on the high-frequency modes, which, as mentioned before, already have several thousand K only due to ZPE. Indeed, the NH average distance increases with temperature in the classical simulation while it does not change in the quantum one (see Fig. 13a). In **Paper IV**, it is shown that a temperature dependent 1D double-well potential can qualitatively explain this behavior. The

key consideration is that the inner cage of the porphycene molecule, represented by the average nitrogen-nitrogen (NN) distance in Fig. 13b, expands with temperature. More precisely, the DHT barrier becomes higher with the increase of the temperature because the NN distance gets larger, and, as a consequence, the HBs weaken. The magnitude of the temperature modulation of the barrier is fairly small but sufficient to have a decisive impact. In the classical simulations, the increase of the sampling with temperature has a stronger effect, and the previous argument that explains the red-shift with temperature holds (see filled areas in Fig. 13c and 13d). On the contrary, in the quantum simulations, the only effect is the barrier modulation by temperature. As shown in Fig. 13c and 13d, the increase of the barrier height with temperature increases the energy difference between the vibrational ground state and first excited level, which in turn determines the vibrational transition energy, and leads to the observed blue-shift. It is worth stressing that the 1D effective model only pursues the goal of understanding the system, the 'physics viewpoint' mentioned in the introduction. As such, it lacks any quantitative predictive power that can only be accessed by the full-dimensional calculation, which, once more highlights the inherent multi-dimensionality of the problem at hand.

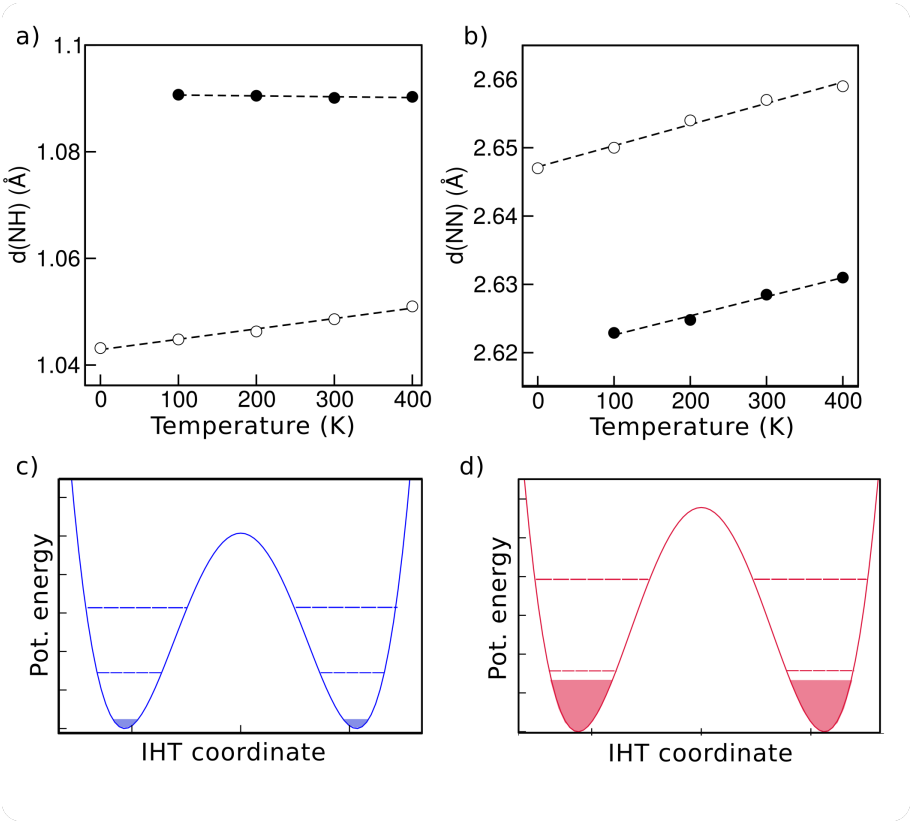

Figure 13: Average NH (a) and NN (b) distances at different temperatures obtained from classical MD (black circles), and PIMD (white circles) simulations. Fig. c) and d) show schematic representations of the effective double-well potential at low (blue) and high (red) temperatures respectively. The bottom of the two curves were set at 0 for the sake of comparison. Dashed lines represents the lowest two vibrational states obtained by solving the TISE, and the filled areas correspond to the energies accessible by 98% of the thermal population at the corresponding temperature.

The second important question addressed for the gas phase porphycene molecule is its DHT mechanism, for which neither experiments nor theoretical simulations had a conclusive answer (see discussion in chapter 1). The second part of **Paper II** tackles this problem using the RPI rate theory, that surpasses previous theoretical approaches applied to this system, and it is able to quantitatively describe multidimensional tunneling at finite temperatures. The fact that measurements in different solvents give approximately the same DHT rates shows that the solvent molecules act as an unspecific bath which ensures thermalization, and justifies the comparison with RPI gas-phase calculations.

The total DHT rate is computed as the combination of the rates arising from both concerted and stepwise mechanism. Each one has its associated instanton pathway and therefore needs an independent instanton calculation. The simulations were done using the same setup as the vibrational spectra. Even though the B3LYP XC functional does a better job in describing the DHT energy barriers than GGA XC functionals, its accuracy is not enough to quantitatively reproduce experimental results. For this reason, the barrier heights were scaled to match the values obtained at the CCSD(T) level of theory. The required simulations were done using the new RPI implementation coded in i-PI which made possible to get converged results efficiently. The obtained DHT rates are $2.19 \times 10^{11} \mathrm{s}^{-1}$ at 150 K and $0.63 \times 10^{11} \mathrm{s}^{-1}$ at 100 K, and compare satisfactorily with experimental observations, $1.62 \times 10^{11} \mathrm{s}^{-1}$ and $1.09 \times 10^{11} \mathrm{s}^{-1}$ at the same temperatures. More exciting results appear when the contribution of the concerted mechanism to the total rate is computed. While at 100 K it represents 95 % of the total DHT rate, at 150K its contribution goes down to 63 %, and decreases further at higher temperatures. These results reveal a transition from concerted to stepwise mechanism at approximately 150K, and disproves the accepted behavior of a single mechanism at all temperatures. A schematic representation of the temperature dependence of the mechanism is depicted in Fig. 14a.

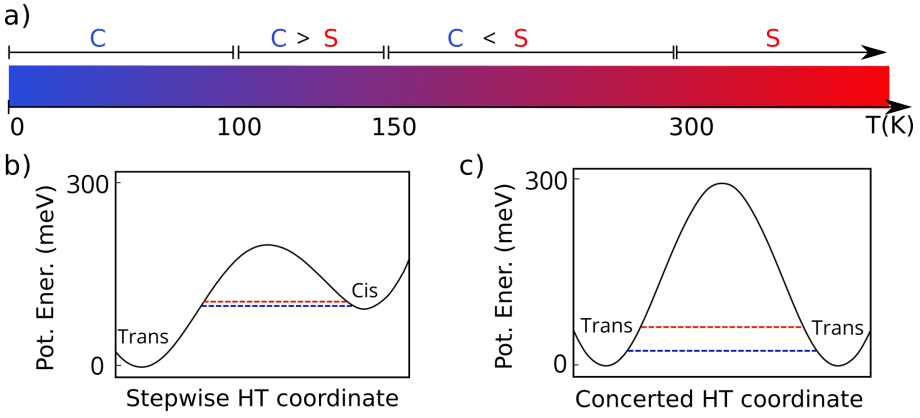

Figure 14: a) Temperature dependence of the DHT mechanism. C and S refer to concerted and stepwise mechanism respectively. b) and c) show 1D cuts of the MEP along the reactive coordinates for stepwise and concerted mechanism respectively. Dashed lines represent the corresponding instanton energies at 100 K (blue) and 150 K (red).

In order to get more information about how the rate changes with temperature, the experimental

rates were modeled by a sum of exponential functions[58]. While two activation energies of 23 meV and 108 meV could be extracted, their atomistic interpretation is far from being trivial. In **Paper II**, it is demonstrated that those activation energies correspond to the concerted and stepwise mechanism. Again, the 1D approach is considered to illustrate and explain the key ideas. The instanton potential energy superimposed with the MEP along the reactive coordinate is shown in Fig. 14b and 14c. The stepwise mechanism is considered first. The instanton energy does not change with temperature, and it coincides with the relative energy of the product, the *cis* conformer in this case. After all, no tunneling can take place below the relative energy of the product ground state. The Eq. 2.72 shows that since the energy at which the tunneling takes place changes only slightly in the considered temperature range, the microcanonical reaction probability is constant, and therefore, the temperature dependence of the rate is governed mainly by the Boltzmann factor. Because of this, the effective activation energy is the ZPE-corrected energy difference between reactants and products. This result is different to the often used transition state theory, where the predicted activation energy corresponds to the barrier height, i.e., the energy difference between the transition state and reactant configurations. The predicted value is 100 meV, and it compares extremely well with the experimental observation. On the contrary, the concerted mechanism shows a different behavior, and the instanton energy changes with temperature. In order to explain this observation, the geometry at which the tunneling takes place is analyzed. This geometry represents the so-called turning point when the instanton is seen as a classical trajectory in the inverted potential (see Eq. 2.70). Projecting the displacement vector between the geometry at the bottom of the reactant well and the instanton turning point into the *trans* conformer normal modes, shows a remarkable result: more than 80% of the displacement is performed along a low-frequency mode that modulates the cage size. Moreover, it has an energy of 25 meV, which coincides with the observed activation energy in experiments, and it can be easily thermally activated. This coupling has been suggested previously based on energy matching[56], but only now, through the analysis of the main tunneling pathways, was unambiguously assigned.

In summary, **Paper I** and **II** studied the IR and DHT rates for the porphycene molecule in the gas phase. In both cases, the mechanism for the corresponding non-trivial temperature dependence was elucidated and thoroughly explained. While the atomistic mechanisms are particular to this molecule, the methodological framework is general, and may help to achieve a deeper physical understanding in other complex systems where the dynamics of high-frequency quantized modes are determined to a great extent by its coupling with a bath of low-frequency modes. To the best of the author's knowledge, this is the first time that the temperature dependence of a reaction rate is extracted directly from the analysis of the instanton pathways. The results also highlight the importance of the anharmonic NQE and the multidimensional nature of the DHT process.

Since a reliable gas-phase molecule description requires the inclusion of all these effects, it is expected that they will also be relevant when the molecule is adsorbed on a surface. In **Paper IV** and **Paper V** the porphycene molecule is placed on 111 and 110 metal surfaces, increasing the theoretical challenge considerably. Unlike in gas-phase simulations, where ultimately CCSD(T)

delivers a reliable PES reference, and quantitative predictions without any experimental input can be performed, now the DFA cannot be easily benchmarked, and its validation comes in great extent from its ability to reproduce reliable experimental results in well-control environments. Although only semi-quantitative results are expected for these kind of systems, the atomistic insight that DFA simulations can complement the experiments, and therefore, has a significant scientific value.

Paper IV is the result of a collaboration with the experimental group of Takashi Kumagai. Porphycene molecule adsorbed on surfaces of Cu(111), Ag(111) and Au(111) was studied, and the DHT rate was measured for the first two. On Au(111), the different conformers could not be experimentally resolved, which was attributed to the fact that either the DHT rates are greater than the instrument resolution, or simply because both tautomers present similar STM images. On the other two surfaces, the experiments clearly show that the *trans* molecule is the thermodynamically stable tautomer, which is consistent, within the expected error bars for the employed DFA calculations (PBE XC functional with vdW dispersion corrections[148]). Even though the 111 surface seems to be quite flat and smooth, the minimum energy geometries were only found after an exhaustive grid search by translating the center of mass of the molecule and rotating them among all the possible locations. Surprisingly, several local minima that only differ by a small rotation or buckling of the molecule led to energy differences up to 100 meV. The geometries of the most stable local minima are dictated by the interaction of the imine nitrogen (nitrogen without NH bond) with the surface atoms underneath. Since the amine nitrogen (nitrogen with NH bond) has a weaker interaction with the surface in comparison to the imine nitrogen, the molecule buckles considerably. This observation differs from the gas-phase situation, where the molecule remains flat. This distortion, in turn, determines the tautomerization energy barrier leading to slower DHT rates on Cu(111) by two and 14 orders of magnitude w.r.t the rates observed on Ag(111) and gas-phase, respectively.

At this point, it is worth clarifying a concept that is sometimes misinterpreted or overlooked. The key factor determining how much the DHT rates are reduced upon adsorption is not the bare surface-molecule interaction strength, but rather its inhomogeneity and the consequent molecular geometry distortions that it generates. A clear example to illustrate this point is to consider placing a porphycene molecule on an ideal flat surface with a large and homogeneous molecule-surface interaction. Since the interaction is homogeneous, the adsorbed molecule would adopt a flat conformation, and the DHT rates are going to be identical to the gas phase rates, where the highest values are observed. Then, the only consequence of varying the strength of the homogeneous interaction would be the temperature at which the molecule desorbs.

In **Paper V** the dynamics of the DHT on 110 metal surfaces was addressed. Unlike in gas phase or 111 surfaces, the *cis* conformation is the most stable tautomer on these surfaces. The DHT rates for the Cu(110) and Ag(110) were computed using the RPI rate theory representing the most challenging simulations performed in this thesis. The several improvements of the standard RPI methodology described in the previous chapter made possible to carry out the required simulations which otherwise would have not been feasible.

The calculated DHT rates on Cu(110) are in good agreement with the experimental results[29] across several orders of magnitude (Fig. 15a). The calculations shed light into the DHT mechanism and unambiguously identified the stepwise mechanism as the dominant one at the considered temperatures. This conclusion could not be obtained from the experimental observations since the residence time for the *trans* intermediate was too short to be evidenced. Moreover, the effective activation energy predicted by the simulations has a value of 190 meV which compares reasonably well with the value of 168 ± 12 meV reported by experiments. Similarly to what observed in the gas phase, the harmonic estimation of the energy difference between reactant and product, 172 meV, delivers a good approximation of the effective activation energy.

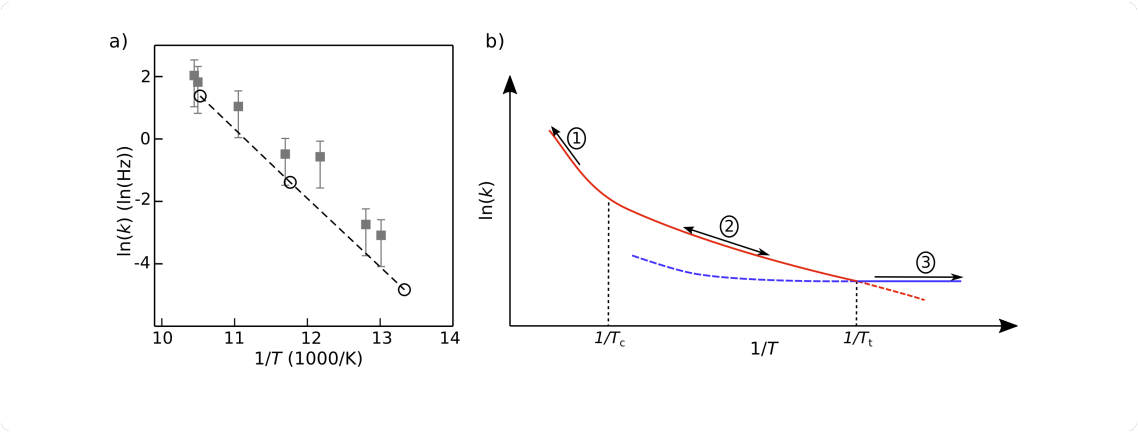

Figure 15: a) Calculated DHT rates, k for porphycene molecule on Cu(110) surface (white circles) compared to experimental data (grey squares). b) Scheme that illustrates the proposed three regimes for the DHT of porphycene molecule on metal surfaces. Red a blue lines represent stepwise and concerted mechanism, respectively. Thick (dashed) lines denotes the dominant (minor) mechanism at each temperature. T_c T_t are the cross-over and transition temperatures, respectively. The numbers 1, 2 and 3 illustrate the three different temperature regimes of the DHT process, see text.

In the case of the Ag(110) surface, the DHT rates are substantially faster than on Cu(110) but still slower than in the gas phase[61]. Unlike the Cu(110) situation, the experimental results evidence two distinctive regimes. The first one, above 15 K, where an Arrhenius behavior with an effective activation barrier of 15 meV is observed, and the second one at lower temperatures, where the rate does not significantly change anymore. RPI calculations were performed for the Ag(110) surface for both reaction mechanisms to get their behavior in the low temperature limit. The effective activation barrier for the stepwise mechanism was found to be 45 meV which compares reasonably well with the experimental result when considering that small values normally present higher relative errors. More interestingly, close to 10 K the instanton pathway for the concerted mechanism starts at the reactant minimum indicating that tunneling takes place from the reactant vibrational ground state. As a result, the rates for the concerted mechanism do not change with temperature below this point, and the concerted mechanism becomes dominant at approx. 8.5 K and below. Therefore, the simulation results provide an explanation to the transition between the

two regimes of temperature dependence observed in experiments and propose that it should be interpreted as a change in the DHT mechanism.

Performing RPI calculations with the surface atoms fixed at the reactant position and comparing them with the calculations without constraints made possible to address the impact that the motion of the surface atoms have on the DHT dynamics. While on Ag(110) they produce an increase by a factor of 4 of the DHT rates, on Cu(110) where the molecule-surface interaction is stronger and the porphycene molecule buckles more, the rate increases by more than two orders of magnitude. These results can be understood analyzing the instanton pathway. It can be observed that not only the hydrogen atoms participate in the tunneling process but also heavier atoms like carbon and nitrogen, and in some extent the surface atoms, contribute as well. This is manifestation of the multidimensional nature of the tunnelling process and makes it clear that reducing the dimensionallity of the problem is inappropriate[282–284]. Nonetheless, these results should not hide the fact that changes in the PES landscape upon adsorption have even a greater impact, since at the same temperatures the DHT rate in the gas phase are ten orders of magnitude faster.

The behaviour of the DHT rates with temperature can be generalized to other metallic 110 surfaces. **Paper V** shows a way to estimate the different temperature regimes for the DHT dynamics by using only easy-to-compute values. The required values are the energy barrier for the concerted and stepwise mechanism, the energy difference between the *cis* and *trans* tautomers, and the cross-over temperature of the stepwise reaction, T_c. The expected Arrhenius plot, i.e. ln(rate) vs. $1/T$, has mainly three regimes (Fig 15b). At high temperatures the reaction behaves classical and goes mainly trough the lower barrier which is normally the stepwise route (label 1). Considerably below T_c, the low temperature limit of the stepwise reaction is achieved and the slope can be approx. by the energy difference between product and reactant in the same manner as it was done before (label 2). Finally, and at sufficiently low temperatures, the concerted mechanism takes the lead and the curve becomes flat (label 3). The transition temperature, T_t, between the last two regimes can be estimated by relating the low temperature limit of the concerted rate with an hypothetical tunneling splitting computed using a 1D model (see details in **Paper V** supporting information). The first conclusion that emerges from this analysis is that, for all the considered surfaces, the T_c values are close to 260K, which shows not only the similarity of the DHT process across surfaces with varying interaction strength, but also the importance of nuclear tunneling at considerably high temperatures. The second important conclusion is that, while the concerted mechanism should dominate at temperatures close to 20K and below, only on Ag(110) the DHT rate is fast enough to be observed in STM experiments.

In summary, the static and dynamical properties of the porphycene molecule adsorbed on several 110 and 111 metallic surfaces were studied in **Papers IV** and **V**. The obtained results provided a comprehensive understanding of the DHT process at surfaces and helped to clarify several puzzling experimental observations regarding the DHT rates. In particular, its temperature dependence and atomistic mechanism in different scenarios were established, and the important role of the surface fluctuations was identified.

The last work of this thesis, **Paper VI**, proposes a new type of approximation denominated SL-RPC that reduces the computational cost associated with PIMD simulations on weakly bounded systems like molecules on surfaces (see section 2.4.4). Among other applications, this approximation becomes particularly relevant to study hydrogen transfer, where the RPI method can no longer be applied since the reaction is rarely determined by only few specific pathways, and the need for a sampling procedure cannot be circumvented.

Paper VI studies the dissociation of water at Pt(221) surface. The reason to investigate this model was three-fold: In the first place, this surface has stepped geometry representing a good model of realistic surface defects where most of the surface reactions take place due to its high reactivity in comparison to close-packed surfaces[285]. Indeed, the water molecules are strongly adsorbed at the surface steps, and water wires can be experimentally isolated[286]. In the second place, it has been suggested that that NQE may play a crucial role in favoring the water dissociation[287], and last but not least, water clusters have a complex conformational space ideally suited to benchmark the SL-RPC approximation.

MD and PIMD simulations, augmented by the SL-RPC when possible, were performed for intact and dissociated structures of the water molecules bringing finite temperature insight to the 0 K studies available in the literature[287–289]. The simulations were performed at 160K and 300K in order to enable comparison with experimental measurements[286,290]. Energies, forces and electronic properties were calculated through the DFA using the PBE XC functional with vdW dispersion corrections[148]. As expected, the conformational space explored by the system has several competing local minima, many of which had not been reported before. Inclusion of ZPE, by the Eyring TST, leads to an increase of dissociation rates by three orders of magnitude while tunneling effects are of minor importance at those temperatures. Performing quantum to classical thermodynamic integrations[291], it was found that the nuclear quantum contributions to the dissociation free energies favor the dissociated states by 150 meV per water dimer. These effects can be traced back to the different strength of the covalent bonds in the dissociated and intact structures. Mainly, a red-shift of more than 1000 cm^{-1} of the vibrational frequency going from an OH bond on one water molecule to the newly formed Pt-H bond, formed by the detached hydrogen atom, explains the lowering of ZPE upon dissociation.

The SL-RPC approximation was carefully tested for both intact and dissociated structures by tracking the expected value of the quantum kinetic energy for each atom. For the intact case, $P' = 1$ was sufficient to convergence within the statistical error. Since the water molecule forms a hydrogen bond with the surface atoms, this system represents a strict test in comparison to other weakly bound adsorbates. In contrast, for the dissociated structures, the SL-RPC performs poorly when $P' = 1$ is used, and only for $P'/P > 0.8$, the results approach the reference values (see Eq. 2.61). As anticipated, since the detached hydrogen forms a bond with the Pt atom underneath, and the remaining H_5O_2 fragment is partially charged, the molecule-surface interaction can not be considered as a weak one, and the assumptions of the approximation break down. The two cases presented exemplify the situation described above by chemisorption and physisorption, showing

the strengths and limitations of the SL-RPC scheme.

The electronic properties of the system at finite temperature were also investigated. Due to the different adapted conformations by the water molecules in the MD and PIMD simulations, the observed electronic properties considerably differ from the ones corresponding to the minimum energy structures. Particularly, the work function change (WFC), defined as the work function of the full system minus the bare surface work function, is significantly impacted by both the temperature and NQE. Inclusion of classical anharmonicity and temperature effects reduce WFC by 0.3 eV w.r.t to the static estimates, and inclusion of NQE reduces it even further by 0.2 eV. These changes on WFC are predominately dominated by the change in orientation of the molecular dipoles w.r.t to the surface normal. Even though smaller differences are expected for less flexible molecules, these results challenge the direct comparison of static WFC theoretical values with experimental results[292]. Finally, since NQE affect the WFC of different structures differently, it is proposed that deuteration experiments can help to experimentally verify the structure of water wires on Pt(221) and in other metallic stepped surfaces, where direct experimental confirmation of the positions of the hydrogen atoms is exceptionally challenging to obtain[293].

In summary, in **Paper VI** the water dissociation on Pt(221) was studied. The significance of temperature, anharmonicity, and quantum fluctuations on the equilibrium and dynamical properties was addressed, demonstrating their decisive role in the dissociation reaction. Finally, a novel approximation to perform PIMD simulations for weakly bound systems at almost classical cost was proposed and comprehensively evaluated.

Chapter 5

Publications

The content of this chapter are the scientific manuscripts published in the context of this thesis. The publications are ordered thematically rather chronologically. Together with the manuscript, an introductory page containing the publication title, authors' names, reference, DOI number, URL, and authors' contributions is provided.

5.1 Paper I

"i-PI 2.0: A universal force engine for advanced molecular simulations"

V. Kapil, M. Rossi, O. Marsalek, R. Petraglia, **Y. Litman**, T. Spura, B. Cheng, A. Cuzzocrea, R. H. Meißner, D. M. Wilkins, B. A. Helfrecht, P. Juda, S. P. Bienvenue, W. Fang, J. Kessler, I. Poltavsky, S. Vandenbrande, J. Wieme, C. Corminboeuf, T. D. Kühne, D. E. Manolopoulos, T. E. Markland, J. O. Richardson, A. Tkatchenko, G. A. Tribello, V. Van Speybroeck and M. Ceriotti.

Comp. Phys. Comm. ***236****, 214-223 (2019)*

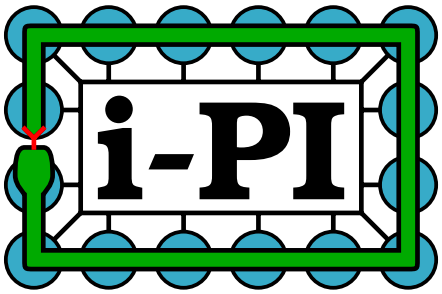

Figure 16: i-PI logo

URL: `https://doi.org/10.1016/j.cpc.2018.09.020`

DOI: 10.1016/j.cpc.2018.09.020

Author contributions: I implemented and benchmarked the instanton rate and tunneling splitting calculations in i-PI with input from J. Richardson and M. Rossi. The instanton calculations and related figures presented in the paper were performed by myself. M. Rossi, J. Richardson and myself wrote the instanton implementation description in the manuscript. I also contributed with the implementation of the geometry optimizers in the code, which is mentioned in the manuscript.

5.2 Paper II

"Elucidating the Nuclear Quantum Dynamics of Intramolecular Double Hydrogen Transfer in Porphycene"

Y. Litman, T. Kumagai, J. O. Richardson, M. Rossi.

J. Am. Chem. Soc. ***141***, *2526-2534 (2019)*

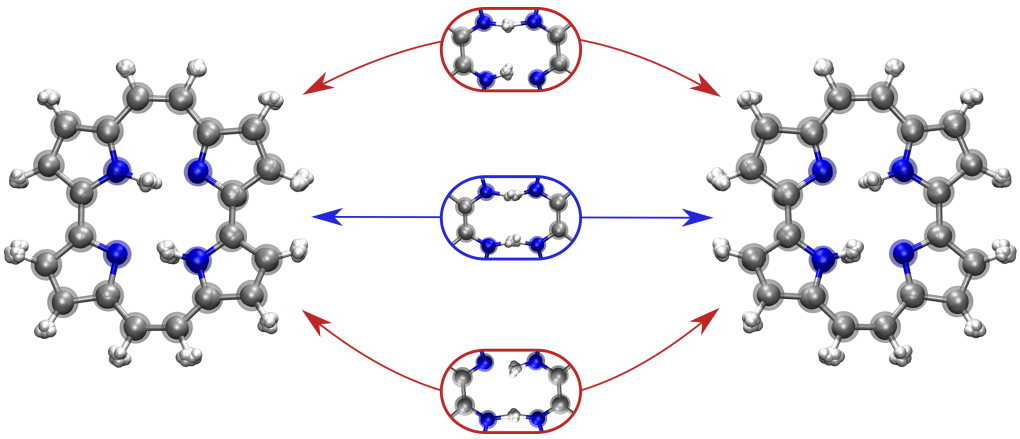

Figure 17: Adaptation of Paper II graphical abstract for this thesis.

URL: `https://doi.org/10.1021/jacs.8b12471`

DOI: 10.1021/jacs.8b12471

Author contributions: M. Rossi and I designed the research. The electronic structure calculations and the RPI simulations were performed by myself. M. Rossi, J. Richardson and I analyzed the simulation results. MR and I performed the TRPMD simulations. I implemented the adiabatic model and performed the corresponding calculations. All the authors contributed to the writing of the manuscript.

5.3 Paper III

"Temperature dependence of the vibrational spectrum of porphycene: a qualitative failure of classical-nuclei molecular dynamics "

Y. Litman, J. Behler, and M. Rossi

Faraday Discuss., ***221***, *526-546 (2020)*

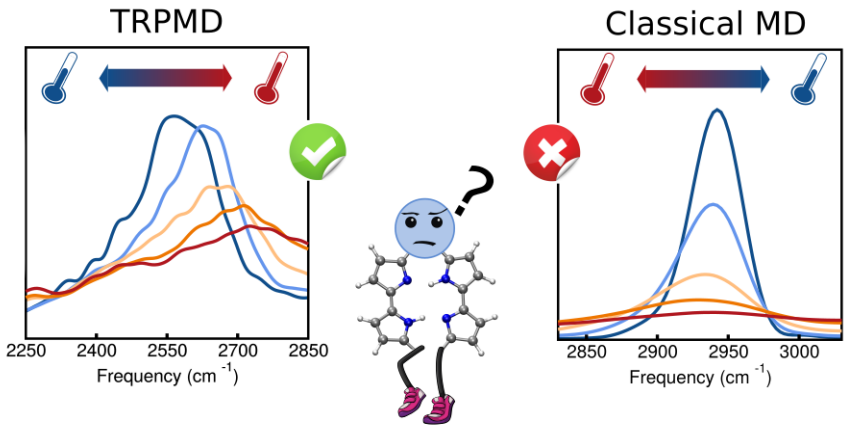

Figure 18: Paper III graphical abstract. Reprinted from Litman *et al.*[294] with permission from The Royal Society of Chemistry.

URL: `http://doi.org/10.1039/C9FD00056A`

DOI: 10.1039/C9FD00056A

Author contributions:

M. Rossi and I designed the research. J. Behler helped me to perform the training of the high-dimensional neural networks and supervised it. I performed all simulations presented in the manuscript. All the authors contributed to the writing of the manuscript.

5.4 Paper IV

"Quantum tunneling in real space: Tautomerization of single porphycene molecules on the (111) surface of Cu, Ag, and Au"

T. Kumagai, J.N. Ladenthin, **Y. Litman**, M. Rossi, L. Grill, S. Gawinkowski, J. Waluk and M. Persson.

J. Chem. Phys. ***148****, 102330 (2018)*

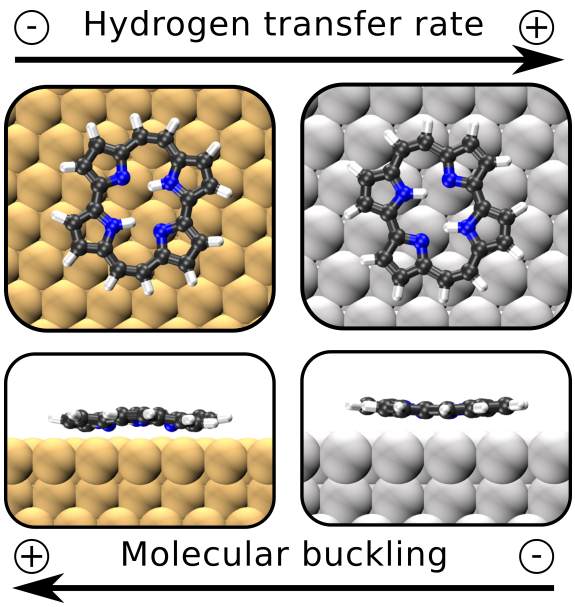

Figure 19: Paper IV graphical abstract created for this thesis.

URL: `https://doi.org/10.1063/1.5004602`

DOI: 10.1063/1.5004602

Author contributions: I performed the DFA simulations with PBE + vdW^{surf} presented in the manuscript. M. Persson performed the calculations with the other XC functionals. M. Rossi, M. Persson, and I discussed the simulation results and wrote the theoretical part of the manuscript. All the authors contributed the final version of the manuscript.

5.5 Paper V

"Multidimensional Hydrogen Tunneling in Supported Molecular Switches: The Role of Surface Interactions "

Y. Litman, and M. Rossi

Submitted

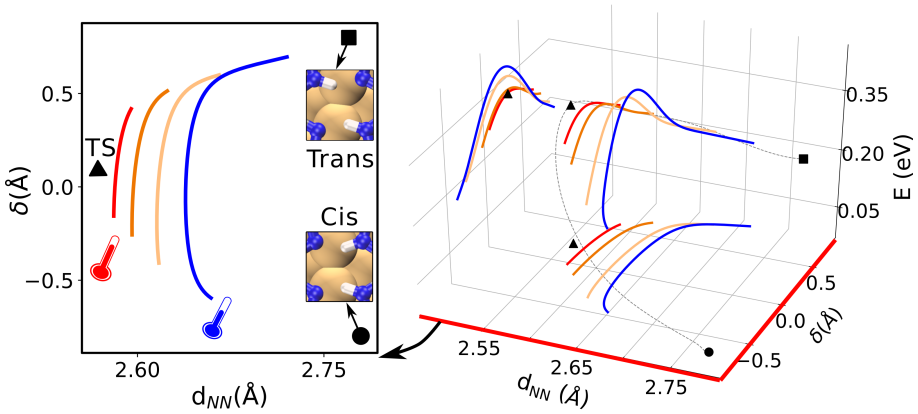

Figure 20: Paper V graphical abstract created for this thesis.

Author contributions: M. Rossi and I designed the research. I performed the DFA and RPI simulations and implemented several improvements in the RPI module of i-PI required for this work. Both authors discussed the results and wrote the manuscript.

Multidimensional Hydrogen Tunneling in Supported Molecular Switches: The Role of Surface Interactions

Yair Litman*
Fritz Haber Institute of the Max Planck Society, Faradayweg 4–6, 14195 Berlin, Germany and Institute for Chemistry and Biochemistry, Freie Universität Berlin, Arnimallee 22, 14195 Berlin, Germany

Mariana Rossi†
Fritz Haber Institute of the Max Planck Society, Faradayweg 4–6, 14195 Berlin, Germany and MPI for the Structure and Dynamics of Matter, Luruper Chaussee 149, 22761 Hamburg, Germany

(Dated: May 19, 2020)

The nuclear tunneling crossover temperature (T_c) of hydrogen transfer reactions in supported molecular-switch architectures can lie close to room temperature. This calls for the inclusion of nuclear quantum effects (NQE) in the calculation of reaction rates even at high temperatures. However, standard computations of NQE relying on parametrized dimensionality-reduced models, quickly become inadequate in these environments. In this letter, we study the paradigmatic molecular switch based on porphycene molecules adsorbed on metallic surfaces with full-dimensional calculations that combine density-functional theory for the electrons with the semi-classical ring-polymer instanton approximation for the nuclei. We show that the double intramolecular hydrogen transfer (DHT) rate can be enhanced by orders of magnitude due to surface fluctuations in the deep tunneling regime. We also explain the origin of an Arrhenius temperature-dependence of the rate below T_c and why this dependence differs at different surfaces. We propose a simple model to rationalize the temperature dependence of DHT rates spanning diverse fcc [110] surfaces.

PACS numbers: 82.20.Xr, 82.37.Np, 71.15.Mb, 68.43.Fg

Nuclear tunneling is an inherently quantum-mechanical process that can strongly impact the properties of matter in a wide variety of situations, ranging from biological enzymes to organic-based technologies [1–4]. In complex environments, it has been recognized that signatures of tunneling on rate processes are often not well captured by textbook theories [5, 6] and in particular, in hydrogen transfer reactions, the small mass of hydrogen makes tunneling pronounced [7]. Still, a theoretical description of nuclear tunneling that goes beyond a simple one-dimensional approximation and considers anharmonic coupling between many degrees of freedom in larger-scale systems remains a challenge [8–10]. To build up a systematic understanding of multidimensional rate processes in the deep tunneling regime and the impact of the environment on hydrogen dynamics, a fully *ab initio* treatment of simple, yet non-trivial, reactions in well controlled conditions is desired.

Tetrapyrrole macrocycles, like porphyrin, naphtalocianine, and porphycene, show a remarkable diversity of functional properties [11–15], and were proposed, among others, as molecular switches [16–18]. The intramolecular hydrogen transfer reaction that occurs in the inner cage of these molecules, known as tautomerization, can be triggered remotely by different external stimuli [19–24]. Moreover, because the reaction takes place without a pronounced conformational change, these molecules can be incorporated in nanoscale devices. Within this area, controlling the dynamical properties of these molecules is central to advance rational design. Molecular diffusion and rotations have been more often addressed [25–29], while key aspects of the hydrogen transfer reaction mechanism and its temperature dependence remain poorly understood. This is especially due to the challenges in the description of multidimensional quantum dynamics that cannot be captured by perturbative treatments of anharmonic couplings [5, 30–33].

In this Letter, we study the effect of tunneling on the double intramolecular hydrogen transfer (DHT) of two representative systems, namely porphycene on Cu(110) and Ag(110) surfaces. In these reactions, the tunneling crossover temperature, which represents the temperature below which tunneling becomes greater than classical hopping over the barrier ($T_c = \hbar\omega_b/2\pi k_B$, where ω_b is the imaginary frequency of the unstable mode at the transition state geometry [34]) lies close to room temperature. Specifically, we i) identify the multi-dimensional DHT mechanisms at different temperatures, ii) clarify their temperature dependence, and iii) elucidate the role of surface fluctuations in the deep tunneling regime. The results we obtain are able to explain puzzling experimental measurements [4, 21] that showed an unexpected temperature dependence of the DHT. In addition, they show that instead of acting only as a passive observer of the reaction, in certain situations the surface takes a prominent role in the tunneling event.

We here employ a combination of density-functional theory (DFT) for the electronic degrees of freedom with the ring polymer instanton (RPI) approximation [35, 36]

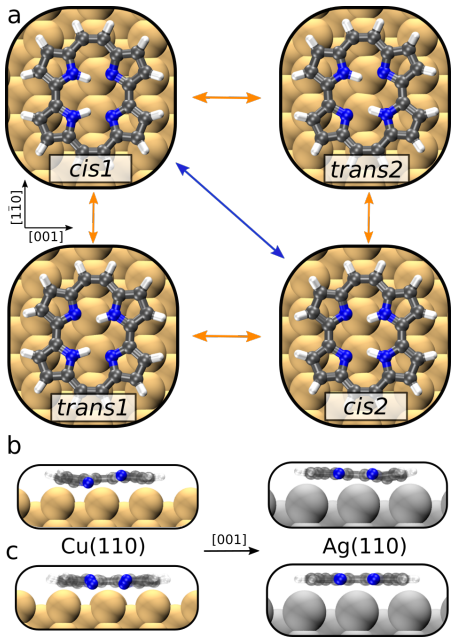

FIG. 1. (a) Top view of the local minima of porphycene on Cu(110). Concerted and stepwise DHT mechanisms are represented by blue and orange arrows, respectively. Lateral view of the *cis* (b) and *trans* (c) conformers, of porphycene on Cu(110) and Ag(110).

for the nuclear degrees of freedom. RPI can be viewed as an extension of Eyring [37] transition state theory (TST) which includes tunnelling and captures anharmonic contributions along the reaction pathway. It is a semi-classical method that uses discretized closed Feynman path (CFP) integrals to evaluate tunneling rates in the deep tunneling regime. This approximation finds the dominant stationary pathways in the CFP that connect reactants and products, the instanton pathways. Then, a series of steepest descent approximations to evaluate the flux-side correlation function leads to the instanton approximation for thermal reaction rates k_{inst} [38]. The rate can be expressed as

$$k_{\mathrm{inst}}(\beta) = A_{\mathrm{inst}}(\beta) e^{-S[\mathbf{x}_{\mathrm{inst}}(\beta)]/\hbar}, \qquad (1)$$

where A_{inst} accounts for the harmonic fluctuations around the instanton pathway $\mathbf{x}_{\mathrm{inst}}$, S is the Euclidean action, and $\beta = 1/k_{\mathrm{B}}T$ with k_{B} the Boltzmann constant and T the temperature. In the discretized CFP space, $\mathbf{x}_{\mathrm{inst}}$ is a first order saddle point. Albeit approximate, this method shows the best tradeoff in situations where the quantum exponential wall would prevent a full dimensional evaluation of the exact tunneling rate [6, 39].

Within the Born-Oppenheimer (BO) approximation, evaluating Eq. 1 requires the BO energies and forces. We here employ the most accurate level of theory affordable for the system size and number of system replicas required. We employ DFT with the Perdew-Burke-Ernzerhof (PBE) exchange-correlation functional [40] including the Tkatchenko-Scheffler [41] dispersion correction modified to treat physisorption on surfaces [42]. We thereby ensure a good description of the anisotropic electron density redistribution upon porphycene adsorption [43, 44]. At this level of theory, we do not expect reaction barriers to be quantitatively accurate [45], but expect to capture qualitative trends and the correct physics. In the supporting information (SI), we report selected geometries calculated with a range-separated hybrid functional for comparison. These calculations were enabled by the combination of the FHI-aims [46] all-electron code and the i-PI [47, 48] universal force engine. Details and convergence tests are provided in the SI.

In porphycene, the inner-cage hydrogen atoms can adopt different configurations, giving rise to two stable tautomers, coined *cis* and *trans*. Each tautomer is two-fold degenerate and their structures on Cu(110) and Ag(110) are shown in Fig. 1. On these surfaces, the *cis* tautomer is more stable than the *trans* tautomer by 172 and 20 meV, respectively. Indeed, on the same surfaces, experiments observe almost exclusively the *cis* tautomer [4, 23, 49]. The DHT of the *cis*→*cis* reaction can happen through two possible mechanisms. The concerted mechanism, where the hydrogen atoms are transferred together, without the existence of a stable intermediate and passing through a second-order saddle point, and the stepwise mechanism, where the hydrogen atoms are transferred sequentially and the reaction involves a *trans* intermediate.

We have recently studied the DHT of porphycene in the gas phase [33], and found that there is a competition between a concerted and a stepwise DHT at different temperatures. However, new effects arise due to the interaction between the molecule and the surface. In order to rationalize them, we divide the influence of the surface on the physisorbed molecule into static and dynamical effects. The static surface effects refer to the change in the potential energy landscape upon adsorption, and can affect both static and dynamical properties of the adsorbed molecule. For example, while the global minimum in the gas phase is the *trans* tautomer in a flat conformation, on Cu(110) and Ag(110) the relative tautomer stability is reversed and the molecule is buckled, as shown in Fig. 1b and 1c. This distortion changes the DHT energy barriers and consequently the hydrogen dynamics. Dynamical surface effects, on the other hand, refer to the impact that the motion of the surface atoms have on the molecular properties. As it will be shown, they can significantly influence the dynamics of the DHT.

On Cu(110), we calculate $T_c = 264$ K for the DHT and show the instanton tunneling rates of the *cis*→*cis* reaction in Fig. 2a. We show rates between 75 and 150 K because they lie well within the deep tunneling regime and we wish to compare with experimental results in the same temperature range [21], shown in the inset. In this

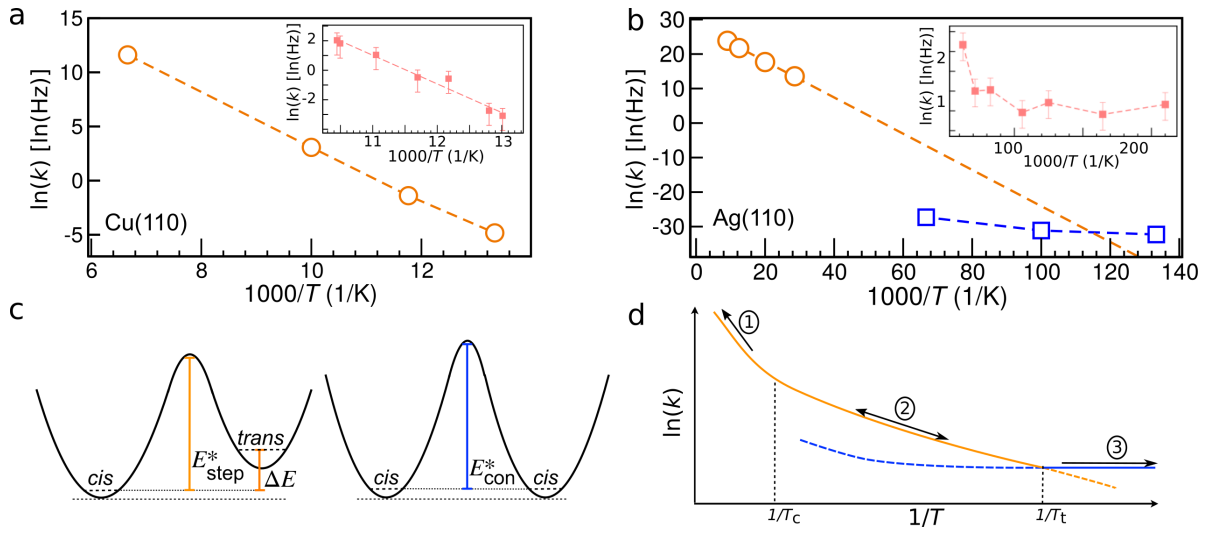

FIG. 2. (a) Calculated DHT rates k_{inst} for the *cis* → *cis* reaction of porphycene on Cu(110) between 75 and 150 K. At these temperatures, k_{inst} only includes contributions from the stepwise mechanism . The inset shows experimental results from Ref. [21]. (b) Calculated DHT k_{inst} for the *cis* → *cis* reaction of porphycene on Ag(110) between 7.5 and 110 K. Orange circles represent k_{inst} of the stepwise mechanism and blue squares of the concerted mechanism. The inset shows experimental results from Ref. [4]. (c) Schematic 1D potential energy surfaces of the stepwise (left) and concerted (right) reactions. The ZPE for reactant and products are shown, while the ZPE at the barrier top is not (but it was included in the multidimensional calculations). (d) Schematic representation of the different temperature dependence regimes of the stepwise (orange) and concerted (blue) DHT rate of adsorbed porphycene. Full/dashed lines represent the dominant/minor mechanism. The numbers 1, 2 and 3 illustrate the three different regimes, see text.

case, we find a very good agreement with experiment throughout the six-orders of magnitude variation of the rate. The calculated effective activation energy E_{A} is 190 meV. This compares well with the value of 168 ± 12 meV reported by experiments. Both the calculated rates and the measured ones show an Arrhenius-like temperature dependence even though tunneling is dominant at this temperature range. We proceed to explain the origin of this dependence.

The calculated DHT rates contain contributions almost exclusively from the stepwise mechanism, because at these temperatures it is several orders of magnitude faster than the concerted alternative. We propose that the *trans* intermediate was not observed because its predicted residence time is ≈ 0.1 ns, which lies beyond the time resolution of STM experiments (≈ 100 μs). The instanton trajectory provides an intuitive view of the reactive process by showing the main "instantaneous" tunneling configuration that the delocalized nuclei adopt. The trajectory is visualized in Fig. S1 at several temperatures. As the temperature is decreased, the reaction takes shorter pathways and crosses regions of higher PES energy. Moreover, we observe a considerable contribution from heavier atoms like C and N and, interestingly, even Cu atoms to the tunneling mechanism (see Tab. S11). These are manifestations of the multidimensional nature of the tunnelling process and prove that reducing the problem dimensionality is inappropriate [8, 50, 51].

Surface	T (K)	κ_{tun}	KIE_{inst}	KIE_{TST}	SFE
Cu(110)	100	1.0	21	89	34
Cu(110)	85	1.2	32	197	106
Cu(110)	75	2.4	66	397	464
Ag(110)	75	14.9	-	-	4

TABLE I. Tunneling enhancement factor (κ_{tun}), and kinetic isotopic effects (KIE) and surface fluctuations enhancement (SFE). See definitions and discussion in the text.

After these considerations, the observed E_{A} can be understood as follows. At low enough temperatures, when only the vibrational ground states (VGS) are populated and a further decrease of the temperature does not affect the vibrational populations, the *trans*→*cis* reaction will proceed from the VGS of the reactant and will be constant with temperature. As a consequence and because of detailed balance, the inverse reaction *cis*→*trans*, which is the rate-controlling step of the stepwise mechanism, must show E_{A} equal to the difference between the VGS energies of reactant and product, that we call ΔE (see Fig. 2c). The height and width of the barrier impact the absolute value of the rate, but they do not affect the Arrhenius slope in the low temperature limit of an asymmetric reaction. Indeed, a harmonic estimation of ΔE is 172 meV, which is very close to the calculated $E_A = 190$ meV from Fig. 2a.

We further analyze how tunneling manifests itself in

these reaction rates in Table I. A standard procedure to estimate the impact of tunneling is to compare $k_{\rm inst}$ with the rate predicted by the Eyring TST ($k_{\rm TST}$), since the latter neglects tunneling but includes ZPE. The tunnelling enhancement factor is $\kappa_{\rm tun} = k_{\rm inst}/k_{\rm TST}$ [52], which is reported in Tab. I. Surprisingly, because these factors are close to 1, they would seem to indicate that tunnelling plays a minor role. To understand this observation, we computed the kinetic isotope effect (KIE), defined as $k^{\rm H}/k^{\rm D}$, where $k^{\rm D}$ was obtained from calculations where the inner-cage hydrogen atoms were replaced by deuterium. If tunnelling would be a minor effect, the only difference in these rates should be ZPE, and since ZPE is captured by both $k_{\rm inst}$ and $k_{\rm TST}$, the KIE of both should be similar. However, as shown in Tab. I, these numbers are different. TST overestimates the KIE in this particular case, for reasons outlined in the SI, Section VII. We thus conclude that $\kappa_{\rm tun} \approx 1$ because of the following. On Cu(110) the ΔE (including harmonic ZPE) between reactants and products, which is a good estimate for E_A in $k_{\rm inst}$ as discussed above, happens to be similar to the energy difference between the ZPE corrected reactant and transition state, which defines E_A for $k_{\rm TST}$ (see Table II). Additionally, because close to T_c both rates are comparable, if E_A are similar, the prefactors also must be. This observation explains why TST fared reasonably well in these systems in the past, even without including the relevant physics of tunneling [44]. Thus, we propose that ${\rm KIE_{inst}}/{\rm KIE_{TST}}$ can be an alternative measure of tunneling contributions to hydrogen transfer reactions.

The investigation of the dynamical surface effects on the DHT required RPI calculations where we fixed the surface atoms at the reactant position. The rates obtained as a result of this constrained optimization lack all contributions from fluctuations of the surface degrees-of-freedom. We call the ratio between the rates with and without those constraints the "surface fluctuations enhancement" (SFE). The SFE for $k_{\rm inst}$ on Cu(110) are reported in Table I and can adopt surprisingly large values. The results show that the dynamical surface effects act on the opposite direction of the static ones, increasing the tunneling rates up to two orders of magnitude. Interestingly, the SFE become larger at lower temperatures because the contribution of heavy atoms to tunneling increases with decreasing temperature.

We then compare the Cu(110) with the Ag(110) substrate, a surface with a weaker static interaction. On Ag(110), porphycene is less buckled upon adsorption (see Fig. 1b) and the *trans* conformer lies only 20 meV above *cis*, but T_c is also 264 K. Accordingly, it was observed in experiments that the DHT rates are substantially faster on Ag(110) than on Cu(110) [4]. Unlike Cu(110), the measured rates show two distinct regimes [4], reproduced in the inset of Fig. 2b. Above $\sim$ 10 K there is an Arrhenius behaviour, while below $\sim$ 10 K the rate shows almost no temperature dependence. In Fig. 2b we show the calculated $k_{\rm inst}$ for the stepwise and the concerted mechanisms of the *cis*→*cis* DHT of porphycene at Ag(110) (see calculation details in the SI). We obtain an $E_{\rm A}$ of 45 meV for the stepwise mechanism, which compares reasonably well with the experimental E_A, which we estimate to be 12 ± 3 meV. The calculated harmonic value of ΔE is again close to $E_{\rm A}$ for this reaction. At 10 K the $\mathbf{x}_{\rm inst}$ for the concerted mechanism starts at the reactant minimum, indicating that tunneling takes place from the reactant VGS. As such, the rates for the concerted mechanism (which is symmetric) do not change with temperature below this point and it becomes dominant below 8.5 K. Hence, we can explain the two regimes observed in experiment by the change in the DHT mechanism. The lack of quantitative agreement between the calculated and measured, transition temperature and rate of the concerted mechanism comes most likely from the potential energy surface used in the calculations, but some dependence of the measured rates on the STM tip cannot be fully discarded. Finally, as shown in Table I, the SFE are smaller here than they were for Cu(110), accounting for a factor 4 increase of the rate at 75 K. This is consistent with the weaker adsorbate-surface interaction strength.

Surface	ΔE (meV)	T_c (K)	$E^*_{\rm step}$ (meV)	$T_{\rm t}$ (K)
Ag(110)	20	264	61	3 - 9
Au(110)	59	264	85	8 - 22
Cu(110)	172	264	222	15 - 41
Ni(110)	170	297	347	13 - 35
Pd(110)	148	293	326	12 - 34

TABLE II. Calculated energies (ΔE, $E^*_{\rm step}$), crossover temperatures (T_c) and estimated transition temperatures ($T_{\rm t}$) for the DHT of porphycene at several fcc 110 surfaces. See definitions in Fig. 2 and text. The $T_{\rm t}$ interval is given by considering calculated or experimental references for the Ag(110) case (see SI). The surface reconstruction of Au(110) [53] was ignored for the sake of comparison.

Building up on these considerations, the dependence of these DHT rates can be schematically understood as shown in Fig. 2d and predicted for other metallic fcc [110] surfaces. One needs to compute the ZPE-corrected energy difference between the *cis* and *trans* tautomers ΔE, the ZPE-corrected energy barrier for the stepwise $E^*_{\rm step}$ and the T_c of the stepwise reaction. At high temperatures the reaction behaves classically and proceeds by hopping over the lower barrier, which is normally the stepwise one, yielding a slope of $\approx E^*_{\rm step}$, labeled 1 in Fig. 2d. Considerably below T_c, the low temperature limit of the stepwise tunneling reaction is achieved and a slope of $\approx \Delta E$ should be observed (labeled 2). Finally, below a transition temperature T_t, the concerted mechanism becomes dominant and the rate becomes independent on temperature (labeled 3).

Using Ag(110) as a reference and building a 1D potential model for which it is necessary to calculate the barrier for the concerted mechanism $E^*_{\rm con}$ (see model in the SI), $T_{\rm t}$ can be estimated for other surfaces. In Table II the calculated values for different fcc [110] surfaces are reported, together with the corresponding estimation of $T_{\rm t}$. All T_c values are similar and close to 300 K, showing the importance of tunneling at considerably high temperatures. While the estimated T_t represent temperatures that can be achieved in different experiments especially for the stronger interacting surfaces, the resulting rates in Cu(110), Ni(110), and Pd(110) would be smaller than 10^{-10} Hz, which lies far beyond the STM detection limit.

To conclude, we have shown how surface interactions can impact tunneling within a prototype molecular switch based on porphycene molecules adsorbed on metallic surfaces. This study was able to show the inadequacy of dimensionality-reduction schemes on these problems, the counter-intuitive origin of different temperature-dependencies of the rates in the deep-tunneling regime, and the effects of surface interaction on the intramolecular hydrogen tunneling. Even though full-dimensional calculations are required to get quantitative results and understand the underlying processes, we could propose a simple estimator to predict the DHT temperature dependence on different metallic surfaces.

The methodology we presented can be straightforwardly applied to other molecules on surfaces where the calculation of internal hydrogen transfer rates are sought. Limitations in the RPI approximation may arise when several local minima of the adsorbate with similar energies are present [43].

The well-defined system addressed in this work allowed us to disentangle and quantify static and dynamic effects of the environment (in this case the metallic surface) on quantum hydrogen dynamics. We showed that dynamical effects of the environment can promote hydrogen tunneling. Such a quantification is normally not straightforward in condensed phase or biological systems. In this sense, this work shows how single-crystal substrates can be an ideal playground where cutting-edge theory and experiment can meet to provide a deeper understanding of quantum dynamics in fluctuating environments. These findings will help to address hydrogen dynamics in biology [54] and in functional materials [55], as well as guide the design and interpretation of future experiments.

The authors thank Stuart Althorpe, Aaron Kelly and Matthias Koch for fruitful discussions, and thank Takashi Kumagai and Jeremy Richardson for numerous discusssions and a careful assessment of the manuscript. The authors acknowledge financing from the Max Planck Society, and computer time from the Max Planck Computing and Data Facility (MPCDF) and the Swiss National Supercomputing Centre (CSCS) under project ID s883.

* litman@fhi-berlin.mpg.de
† mariana.rossi@mpsd.mpg.de

[1] J. P. Layfield and S. Hammes-Schiffer, Chem. Rev. **114**, 3466 (2013).
[2] Y. Jiang, X. Zhong, W. Shi, Q. Peng, H. Geng, Y. Zhao, and Z. Shuai, Nanoscale Horizons **1**, 53 (2015).
[3] N. J. van der Kaap, I. Katsouras, K. Asadi, P. W. M. Blom, L. J. A. Koster, and D. M. de Leeuw, Phys. Rev. B **93**, 140206(R) (2016).
[4] M. Koch, M. Pagan, M. Persson, S. Gawinkowski, J. Waluk, and T. Kumagai, J. Am. Chem. Soc. **139**, 12681 (2017).
[5] J. Meisner and J. Kästner, Angew. Chem. Int. Ed. **55**, 5400 (2016).
[6] M. Topaler and N. Makri, J. Chem. Phys. **101**, 7500 (1994).
[7] J. T. Hynes, J. P. Klinman, H. Limbach, and R. L. Schowen, *Hydrogen-Transfer Reactions* (Wiley-VCH Verlag GmbH and Co. KGaA, 2007).
[8] W. Fang, J. Chen, P. Pedevilla, X.-Z. Li, J. O. Richardson, and A. Michaelides, Nat. Comm. **11**, 1689 (2020).
[9] J. B. Rommel, Y. Liu, H.-J. Werner, and J. Kästner, J. Phys. Chem. B **116**, 13682 (2012).
[10] G. Mills, G. Schenter, D. Makarov, and H. Jnsson, Chem. Phys. Lett. **278**, 91 (1997).
[11] W. Auwärter, D. Écija, F. Klappenberger, and J. V. Barth, Nat. Chem. **7**, 105 (2015).
[12] A. Köbke, F. Gutzeit, F. Röhricht, A. Schlimm, J. Grunwald, F. Tuczek, M. Studniarek, D. Longo, F. Choueikani, E. Otero, P. Ohresser, S. Rohlf, S. Johannsen, F. Diekmann, K. Rossnagel, A. Weismann, T. Jasper-Toennies, C. Näther, R. Herges, R. Berndt, and M. Gruber, Nat. Nano. **15**, 18 (2020).
[13] K. Seufert, M.-L. Bocquet, W. Auwärter, A. Weber-Bargioni, J. Reichert, N. Lorente, and J. V. Barth, Nat. Chem. **3**, 114 (2011).
[14] T. E. Shubina, H. Marbach, K. Flechtner, A. Kretschmann, N. Jux, F. Buchner, H.-P. Steinrück, T. Clark, and J. M. Gottfried, J. Am. Chem. Soc. **129**, 9476 (2007).
[15] L. Grill, J. Phys.: Cond. Matt. **20**, 053001 (2008).
[16] J. L. Zhang, J. Q. Zhong, J. D. Lin, W. P. Hu, K. Wu, G. Q. Xu, A. T. S. Wee, and W. Chen, Chem. Soc. Rev. **44**, 2998 (2015).
[17] J. Waluk, Chem. Rev. **117**, 2447 (2017).
[18] X. H. Qiu, G. V. Nazin, and W. Ho, Phys. Rev. Lett. **93**, 196806 (2004).
[19] P. Liljeroth, J. Repp, and G. Meyer, Science **317**, 1203 (2007).
[20] J. Kügel, M. Leisegang, M. Böhme, A. Krönlein, A. Sixta, and M. Bode, Nano Lett. **17**, 5106 (2017).
[21] T. Kumagai, F. Hanke, S. Gawinkowski, J. Sharp, K. Kotsis, J. Waluk, M. Persson, and L. Grill, Phys. Rev. Lett. **111**, 246101 (2013).
[22] H. Böckmann, S. Liu, J. Mielke, S. Gawinkowski, J. Waluk, L. Grill, M. Wolf, and T. Kumagai, Nano Lett. **16**, 1034 (2016).
[23] J. N. Ladenthin, T. Frederiksen, M. Persson, J. C. Sharp, S. Gawinkowski, J. Waluk, and T. Kumagai, Nat. Chem. **8**, 935 (2016).
[24] S. Mangel, M. Skripnik, K. Polyudov, C. Dette, T. Wol-

landt, P. Punke, D. Li, R. Urcuyo, F. Pauly, S. J. Jung, and K. Kern, Phys. Chem. Chem. Phys. **22**, 6370 (2020).
[25] M. Eichberger, M. Marschall, J. Reichert, A. Weber-Bargioni, W. Auwärter, R. L. C. Wang, H. J. Kreuzer, Y. Pennec, A. Schiffrin, and J. V. Barth, Nano Lett. **8**, 4608 (2008).
[26] H. Marbach and H.-P. Steinrück, Chem. Commun. **50**, 9034 (2014).
[27] P. Shea and H. J. Kreuzer, J. Chem. Phys. **141**, 044124 (2014).
[28] F. Buchner, J. Xiao, E. Zillner, M. Chen, M. Rckert, S. Ditze, M. Stark, H.-P. Steinrück, J. M. Gottfried, and H. Marbach, J. Phys. Chem. C **115**, 24172 (2011).
[29] T. Sonnleitner, I. Swart, N. Pavliček, A. Pöllmann, and J. Repp, Phys. Rev. Lett. **107**, 186103 (2011).
[30] A. Warshel, J. Phys. Chem. **86**, 2218 (1982).
[31] S. Habershon, D. E. Manolopoulos, T. E. Markland, and T. F. Miller III, Annu. Rev. Phys. Chem. **64**, 387 (2013).
[32] W. Fang, J. Chen, Y. Feng, X.-Z. Li, and A. Michaelides, Int. Rev. Phys. Chem. **38**, 35 (2019).
[33] Y. Litman, J. O. Richardson, T. Kumagai, and M. Rossi, J. Am. Chem. Soc. **141**, 2526 (2019).
[34] M. J. Gillan, J. Phys. C: Solid State Phys. **20**, 3621 (1987).
[35] J. O. Richardson and S. C. Althorpe, J. Chem. Phys. **131**, 214106 (2009).
[36] A. Arnaldsson, *Calculation of quantum mechanical rate constants directly from ab initio atomic forces*, Ph.D. thesis, University of Washington (2007).
[37] H. Eyring, Chem. Rev. **17**, 65 (1935).
[38] J. O. Richardson, Int. Rev. Phys. Chem. **37**, 171 (2018).
[39] J. O. Richardson, Phys. Chem. Chem. Phys. **19**, 966 (2017).
[40] J. P. Perdew, K. Burke, and M. Ernzerhof, Phys. Rev. Lett. **77**, 3865 (1996).
[41] A. Tkatchenko and M. Scheffler, Phys. Rev. Lett. **102**, 073005 (2009).
[42] V. G. Ruiz, W. Liu, E. Zojer, M. Scheffler, and A. Tkatchenko, Phys. Rev. Lett. **108**, 146103 (2012).
[43] T. Kumagai, J. N. Ladenthin, Y. Litman, M. Rossi, L. Grill, S. Gawinkowski, J. Waluk, and M. Persson, J. Chem. Phys. **148**, 102330 (2018).
[44] J. Li, S. Yang, J.-C. Ren, G. Su, S. Li, C. J. Butch, Z. Ding, and W. Liu, J. Phys. Chem. Lett. **10**, 6755 (2019).
[45] V. Barone, L. Orlandini, and C. Adamo, Chem. Phys. Lett. **231**, 295 (1994).
[46] V. Blum, R. Gehrke, F. Hanke, P. Havu, V. Havu, X. Ren, K. Reuter, and M. Scheffler, Comp. Phys. Comm. **180**, 2175 (2009).
[47] M. Ceriotti, J. More, and D. E. Manolopoulos, Comp. Phys. Comm. **185**, 1019 (2014).
[48] V. Kapil, M. Rossi, O. Marsalek, R. Petraglia, Y. Litman, T. Spura, B. Cheng, A. Cuzzocrea, R. H. Meißner, D. M. Wilkins, B. A. Helfrecht, P. Juda, S. P. Bienvenue, W. Fang, J. Kessler, I. Poltavsky, S. Vandenbrande, J. Wieme, C. Corminboeuf, T. D. Kühne, D. E. Manolopoulos, T. E. Markland, J. O. Richardson, A. Tkatchenko, G. A. Tribello, V. V. Speybroeck, and M. Ceriotti, Comp. Phys. Comm. **236**, 214 (2019).
[49] T. Kumagai, F. Hanke, S. Gawinkowski, J. Sharp, K. Kotsis, J. Waluk, M. Persson, and L. Grill, Nat. Chem. **6**, 41 (2014).
[50] M. E. Tuckerman and D. Marx, Phys. Rev. Lett. **86**, 4946 (2001).
[51] C. Lin, E. Durant, M. Persson, M. Rossi, and T. Kumagai, J. Phys. Chem. Lett. **10**, 645 (2019).
[52] A. N. Beyer, J. O. Richardson, P. J. Knowles, J. Rommel, and S. C. Althorpe, J. Phys. Chem. Lett. **7**, 4374 (2016).
[53] W. Moritz and D. Wolf, Surf. Sci. **88**, L29 (1979).
[54] J. P. Klinman and A. Kohen, Annu. Rev. Biochem. **82**, 471 (2013).
[55] A. S. Tayi, A. Kaeser, M. Matsumoto, T. Aida, and S. I. Stupp, Nat. Chem. **7**, 281 (2015).

Supporting Information
Multidimensional Hydrogen Tunneling in Supported Molecular Switches: The Role of Surface Interactions

Yair Litman*

Fritz Haber Institute of the Max Planck Society, Faradayweg 4–6, 14195 Berlin, Germany, and Institute for Chemistry and Biochemistry, Freie Universitt Berlin, Arnimallee 22, 14195 Berlin, Germany

Mariana Rossi†

Fritz Haber Institute of the Max Planck Society, Faradayweg 4–6, 14195 Berlin, Germany, and MPI for the Structure and Dynamics of Matter, Luruper Chaussee 149, 22761 Hamburg, Germany

(Dated: May 21, 2020)

* litman@fhi-berlin.mpg.de

† mariana.rossi@mpsd.mpg.de

I. ELECTRONIC STRUCTURE CALCULATIONS

Density functional calculations were performed using the FHI-aims program [1]. The metal surface models were created using the atomic simulation environment ASE [2] and were represented by a slab with a 4×6 surface unit cell including 4 layers and a 70 Å vacuum in the direction perpendicular to the surface. We have only held the bottom two layers fixed and explicitly considered all other degrees of freedom. FHI-aims *light* basis sets and numerical settings were used in the production calculations. Calculations with standard *intermediate* settings were also performed for the Cu and Ag surfaces resulting in deviations smaller than 10 meV. Convergence results with respect to number of layers and k-point sampling of the reciprocal space for all surfaces that were studied are presented in Tab. S1-S7. The settings used in the main text are highlighted in the tables and are in good agreement with previously reported values in Ref. [3] using different exchange correlation functionals (optB86b-vdW, BEEF and vdW-DF-cx).

layers \ k-grid	3x3x1	6x6x1
4	**183**	188
6	194	-
8	188	-
4 (PBE + MBD-nl)	175	-
4 (HSE06 [4]+ vdW [5]	144	-

TABLE S1. Convergence of reaction energy, E(*trans*)-E(*cis*), for the Cu(110) surface. Values are expressed in meV. Unless otherwise specified, the PBE [6] exchange correlation functional augmented with vdW dispersion corrections [5] (vdW^{surf}) was used. MBD-nl refers to the non-local version of the many-body-dispersion method [7], and the exchange correlation functional HSE06 was used with $\omega = 0.11\text{bohr}^{-1}$ [4]. Lattice constant: 3.632Å.

layers \ k-grid	1x1x1	3x3x1	6x6x1
4	**24**	24	-
6	-	31	-
8	-	34	-
4 (PBE + MBD-nl)	-	24	-

TABLE S2. Same as in Tab. S1 but for the Ag(110) surface. Lattice constant: 4.152Å.

layers \ k-grid	3x3x1	6x6x1
4	**356 / 660**	185 / 313
8	346 / 646	-
4 (HSE06 +vdW^{surf})	380 /704	-

TABLE S3. Energy barriers for stepwise / concerted mechanism (respectively) at the Cu(110) surface with different simulation settings. Energies expressed in meV. Values reported for HSE06+vdW^{surf} were calculated at PBE+vdW^{surf} geometries.

layers \ k-grid	1x1x1	2x2x1	6x6x1
4	**188 / 313**	185 / 313	-
8	196 / 342	-	-
4 (HSE06 +vdW^{surf})	250 / 455	-	-

TABLE S4. Same as in Table S3, but for the Ag(110) surface.

layers \ k-grid	3x3x1	6x6x1
4	**72**	75
6	80	-

TABLE S5. Convergence of reaction energy, E(*trans*)-E(*cis*) for Au(110) surface. Lattice constant: 4.157Å. See caption in Tab. S1.

layers \ k-grid	3x3x1	6x6x1
4	**151**	147
6	144	-

TABLE S6. Convergence of reaction energy, E(*trans*)-E(*cis*) for Pd(110) surface. Lattice constant: 3.951Å. See caption in Tab. S1.

layers \ k-grid	3x3x1	6x6x1
4	**209**	210
6	220	-

TABLE S7. Convergence of reaction energy, E(*trans*)-E(*cis*) for Ni(110) surface. Lattice constant: 3.501 Å. See caption in Tab. S1.

II. REACTION AND BARRIER ENERGIES

In Tab. S8, the *cis*→ *trans* energy difference ($\Delta\tilde{E}$), the energy barrier of the stepwise mechanism ($\tilde{E}^*_{\text{step}}$) and the energy barrier of the concerted mechanism ($\tilde{E}^*_{\text{con}}$) for different metallic surfaces are presented. Note that, differently to the values reported in Tab. II in the main text, ΔE and E^*_{step}, the reported values in S8 are not zero-point energy corrected.

Surface	$\Delta\tilde{E}$	$\tilde{E}^*_{\mathrm{step}}$	$\tilde{E}^*_{\mathrm{con}}$
Ag(110)	24	188	313
Au(110)	72	216	386
Cu(110)	183	356	660
Ni(110)	180	498	914
Pd(110)	151	480	822

TABLE S8. Calculated reaction and barrier energies for the DHT of porphycene at several fcc [110] surfaces. Values are not zero-point energy corrected. See definitions in text. Energies are expressed meV.

III. RING POLYMER INSTANTON CALCULATIONS

The ring polymer instanton (RPI) simulations were performed using the implementation created by us in the i-PI package [8, 9]. Several enhancements in the implementation used for these calculations are available in the open-source code repository and described in Ref. [10].

The force convergence criterion for the transition state geometry and instanton optimizations was 0.005 eV/Å. The calculations need to be converged with respect to the number of discretization points of the closed closed Feynman path (CFP), also known as beads. The high-dimensional neural network reported in Ref. [11] which delivers an accurate description of the gas phase porphycene potential energy surface was used to perform such convergence tests due to its reduced computational cost. Since it presents a similar vibrational spectrum to the systems considered here, it shows a comparable convergence behaviour. In Tab. S9 and Tab. S10 the convergence of the hydrogen transfer rates for concerted and stepwise mechanisms, respectively, is presented. The reported rates for the DHT of porphycene on Cu(110) and Ag(110) in Fig. 2 in the main text were calculated with a different number of beads at each temperature, in such way to ensure that the error was always below 20% for the stepwise mechanism and within the order of magnitude for the concerted one.

T(K) \ Beads	128	256	512	1024
90	**0.91**	0.98	1.00	-
60	0.77	**0.95**	1.00	-
30	0.17	0.62	**0.91**	1.00

TABLE S9. Convergence of the reaction rate for the stepwise reaction. For each temperature a value of one is assigned to the converged rate. The number of beads used at each temperature for the instanton rate calculations in this work is highlighted.

T(K) \ Beads	128	256	512	1024	2048
60	**0.82**	0.96	1.00	-	-
30	0.53	**0.79**	0.92	1.00	-
10	-	-	**0.38**	0.69	1.00

TABLE S10. Convergence of the reaction rate for the concerted reaction. For each temperature a value of one is assigned to the calculation with a bigger amount of beads. The number of beads used at each temperature for the instanton rate calculations in this work is highlighted.

IV. MULTIDIMENSIONAL TUNNELING PATHWAYS

In Fig. S1, 3D and 2D projections of the minimum energy pathway (MEP) and the instanton tunneling paths at several temperatures on Cu(110) are presented. The MEP involves a shortening of 0.22 Å of the distance between nitrogen atoms (d_{NN}) and a flattening of the molecular conformation, as quantified in Tab. S11. The tunneling paths can be compared with the position of the transition state in the MEP, marked by a triangle. The projections show that decreasing the temperature causes the tunneling path to depart further from the position of the transition state. For example, at 40 K d_{NN} decreases only 0.1 Å in the tunneling path and it passes through a region 75 meV higher in energy than the transition state point. The shortening of the tunnelling pathway is the well-known concept coined as corner cutting. We note that static surface effects that cause the buckling of the *cis* and

trans conformers on Cu(110) result a considerable increase of the tunneling path length and consequent decrease of k_{inst} with respect to the gas-phase. Similar effects can be observed in Fig. S2 for the Ag(110) surface.

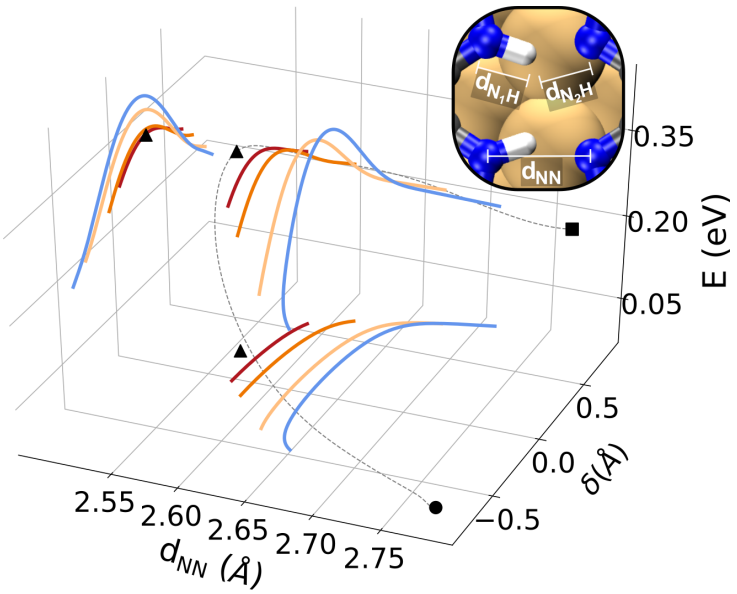

FIG. S1. 3D visualization of the stepwise instanton pathway at Cu(110) at 40 K (blue), 75 K (orange), 150 K (dark orange) and 200 K (red). The *cis*, *trans* and transition state geometries are marked with a circle, square and triangle, respectively. Projections are shown with respect to the nitrogen-nitrogen distance d_{NN}, and the DHT coordinate $\delta = d_{\mathrm{N_1H}} - d_{\mathrm{N_2H}}$. The definition guarantees a value of zero when the hydrogen atom is equidistant from N_1 and N_2. The MEP (grey dashed curve) is also plotted as a reference.

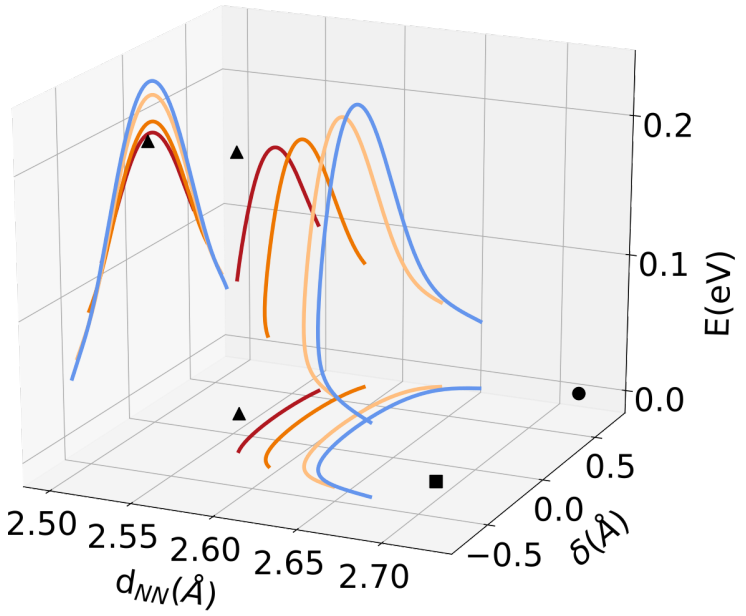

FIG. S2. 3D visualization of the instanton pathway at Ag(110) at 50K (blue), 80K (orange), 150K (dark orange) and 200K (red). The *cis*, *trans* and transition state geometries are represented by black circle, square and triangle, respectively. See coordinates definitions in the caption of Fig. S1.

V. DETAILS ON THE CALCULATION OF THE DHT ON AG(110)

As discussed in the main text, on Ag(110) at 8.5K the concerted mechanism becomes dominant over the stepwise one. The Euclidean action can be written as $S = \beta\hbar U^{\mathrm{RP}}$, where U^{RP} is the potential energy of the ring polymer which represents the discretization of the closed Feynman path [12]. The exponential dependence that the rate has on $S[\mathbf{x}_{\mathrm{inst}}(\beta)]$ results that at low temperatures (high β values) a small error in S has a huge impact on the rate. For example, an error of only 15 meV produces an error in the rate of $\approx e^{17}$ at 10 K, while at 100 K the error is reduced to only a factor of 5. Thus, while the results for Cu(110) are semi-quantitative, the ones corresponding to the Ag(110) surface at low temperatures should be interpreted only qualitatively.

The *cis* → *cis* reaction in the gas phase and on surfaces only admit stationary trajectories that represent second order saddle points rather than first order ones. In a similar spirit to what has been reported in Ref. [13], the steepest descent approximation along the second negative mode can be replaced by the full integration in that direction. This procedure was tested on representative 2D systems performing the required numerical integration using 200

points. The results of this procedure were contrasted with taking the module of the second negative frequency and using the standard expression for the rate. While the results differ by one or two orders of magnitude, the temperature dependence is similar (same order of magnitude). Nevertheless, this effect is minor in comparison to the inaccuracy of several orders of magnitude at low temperatures described before.

VI. HEAVY ATOMS CONTRIBUTION TO THE TUNNELLING PROCESS

In Tab. S11, the tunneling path lengths, computed as the arc length along the instanton pathways, for the different atomic species at several temperatures are presented. As expected, the lower the temperature the higher is contribution from heavy atoms to the tunneling dynamics. Even though the DHT is much slower at Cu(110) than at Ag(110), the tunnelling path lengths are very similar, showing that the molecule-surface interaction strength do not qualitatively modify the reaction pathway.

Species / T(K)	H	C	N	Cu
100	0.54/0.58	0.07/0.06	0.06/0.06	0.01/0.00
75	0.62/0.64	0.09/0.09	0.09/0.09	0.01/0.01
50	0.73/0.72	0.15/0.15	0.16/0.15	0.03/0.02

TABLE S11. Tunnelling path lengths for H, C, N and Cu atomic species for the *cis* $\rightarrow$ *trans* reaction at Cu(110) / Ag(110), respectively. Distances are expressed in Å.

VII. KINETIC ISOTOPE EFFECTS ON THE CU(110) SURFACE

The fact that the kinetic isotope effect (KIE) predicted by transition state theory (TST) is greater than the one predicted by RPI deserves a closer look. The Eyring TST [14] is given by

$$k_{\mathrm{TST}}(\beta) = \frac{1}{2\pi\beta\hbar}\frac{Q^{\ddagger}}{Q_{\mathrm{r}}}e^{-\beta E^{*}} = A_{\mathrm{TST}}e^{-\beta E^{*}}, \tag{1}$$

where $Q^{\ddagger}$ and Q_{r} refer to the transition state and reactant partition functions, respectively,

E^* to the potential energy barrier, and $\beta = 1/k_{\mathrm{B}}T$ with k_{B} the Boltzmann constant and T the temperature. RPI can be expressed in a similar way, see for example Eq. 1 in the main text and Eq. 8 in Ref. [15], where the terms entering the prefactor are explicitly given. In the main text the activation energy E_A and prefactor refer to the effective Arrhenius slope, $E_A = -\frac{\partial ln(k)}{\partial \beta}$, and effective Arrhenius prefactor, $A = k/e^{-\beta E_A}$. In Table S12, and in order to allow a rigorous comparison between the considered rate theories, the terms "exponential factor" and "prefactor" refer, instead, to the factors that appear in Eq. 1 above and in Eq. 1 of the main text.

As discussed already in the main text, the behaviour of the DHT rate in the low temperature limit for the stepwise mechanism presents an effective Arrhenius slope with a value of approximately ΔE. In the case of the hydrogen isotopologue, ΔE happens to coincide with E^*_{step} while for the deuterium isotopologue E^*_{step} is 90 meV larger. As a consequence of these energetic relations, and a fortuitous compensation (see Tab. S12), DHT rates predicted by TST for the hydrogen isotopologue are unexpectedly similar to the ones predicted by RPI. However, the rates for the deuterium isotopologue are largely underestimated below the cross-over temperature which results in the observed overestimation of KIE.

T (K)	A_{inst}(Hz)	$e^{-S_{\mathrm{inst}}/\hbar}$	A_{TST} (Hz)	$e^{-\beta \tilde{E}^*_{\mathrm{step}}}$
75	6×10^{17}	1×10^{-20}	3×10^{21}	1×10^{-24}
85	1×10^{17}	2×10^{-18}	4×10^{20}	8×10^{-22}
100	7×10^{16}	3×10^{-16}	2×10^{19}	1×10^{-18}

TABLE S12. Dimensionless exponential factor ($e^{-S_{\mathrm{inst}}/\hbar}$ and $e^{-\beta \tilde{E}^*_{\mathrm{step}}}$) and prefactors ($A_{\mathrm{inst}}$ and A_{TST}) obtained from RPI and TST simulations, respectively. $\tilde{E}^*_{\mathrm{step}}$ represents the energy barrier for the stepwise mechanism without zero-point energy corrections, because the exponential factor including these corrections is formally in A_{TST}. Interestingly, even though both theories predict similar DHT rates in this temperature range, the corresponding factors differ significantly.

VIII. ESTIMATION OF TRANSITION TEMPERATURE FROM STEPWISE TO CONCERTED MECHANISM IN THE DEEP TUNNELING REGIME

The low temperature behaviour of the DHT rate for the stepwise mechanism can be expressed by an Arrhenius-like formula

$$k_{\mathrm{step}}^{T\to 0}(\beta) \approx A_{\mathrm{step}} e^{-\beta E_A}, \tag{2}$$

where the zero-point energy corrected reaction energy, (ΔE in Tab. II.), is a good approximation of the effective activation energy, E_A, and the prefactor, A_{step}, can be approximated by the values obtained from the instanton calculations performed on the Ag(110) and Cu(110) surfaces. On the contrary, the plateau at the low temperature limit of the rate for the concerted mechanism is difficult to obtain (see Sec. V). Since this reaction is symmetric, a rough estimate of the rate can be obtained from its tunneling splitting, Δ, as

$$k_{\mathrm{con}}^{T\to 0} \approx \frac{\Delta}{2\pi}. \tag{3}$$

A reasonable 1D approximation of the potential energy along the reactive coordinate can be written as,

$$V(x) = V_0 \left[1 - \left(\frac{x}{x_0} \right)^2 \right]^2, \tag{4}$$

where V_0 is taken as the reaction energy barrier ($\tilde{E}_{\mathrm{con}}^{*}$ in Tab. S8), and x_0 is a measure of the barrier width that has to be determined.

In Tab. S13 and S14, the molecular distortions h_{bu}, measured as the difference between the height of the amino and imino N atoms in the molecule, are presented for the *cis* tautomer (reactant) and the transition state geometry corresponding to the concerted reaction at several surfaces. At all surfaces considered, the molecule has to reach a flat conformation, characterized by $h_{\mathrm{bu}} = 0$, for the reaction to take place. $x_0^{\mathrm{Ag}} = 1.2$ Å and $x_0^{\mathrm{Ag}} = 3.0$ Å reproduce Δ values which, by the application of Eq. 2, deliver the experimental and the theoretical plateau rates, respectively. The parameters for other surfaces were obtained by scaling x_0^{Ag} with the ratio of the h_{bu} values reported in Tab. S13, i.e. $x_0^{\mathrm{X}} = x_0^{\mathrm{Ag}} \times (h_{\mathrm{bu}}^{\mathrm{X}}/h_{\mathrm{bu}}^{\mathrm{Ag}})$.

System	h_{im}	h_{am}	h_{bu}
Ag(110)	2.11	2.55	0.44
Au(110)	2.02	2.54	0.52
Cu(110)	1.79	2.38	0.59
Pd(110)	1.68	2.25	0.56
Ni(110)	1.60	2.20	0.60

TABLE S13. Average height of nitrogen atoms belonging to the amino groups (h_{am}) and imino groups (h_{im}) for the *cis* tautomer. $h_{\mathrm{bu}} = h_{\mathrm{am}} - h_{\mathrm{im}}$ is a measure of the molecular distortion (buckling) [16]. Distances are expressed in Å.

System	h_{im}	h_{am}	h_{bu}
Ag(110)	2.32	2.32	0.0
Au(110)	2.34	2.34	0.0
Cu(110)	2.13	2.13	0.0
Pd(110)	2.06	2.06	0.0
Ni(110)	1.86	1.86	0.0

TABLE S14. Values corresponding to the transition state geometry that connects the two *cis* tautomers. See definitions in Tab. S13.

Other scaling factors based on the mass-scaled displacement between the *cis* adsorption conformation and a flat conformation were also tested with similar results.

Finally, the tunnelling splittings were computed using the Wentzel-Kramers-Brillouin (WKB) approximation [17], and the transition temperature T_t is derived by setting $k_{\mathrm{con}}^{T\to 0} = k_{\mathrm{step}}^{T\to 0}$. Both values of T_t, calculated from the experimentally derived parameters and from the theoretically derived parameters, are reported in Tab. II in the main text, giving the reader an assessment of the uncertainty of the estimation. The lower (higher) temperatures correspond to the calculation where the theoretical (experimental) Ag(110) rate value was

used as a reference.

---

[1] V. Blum, R. Gehrke, F. Hanke, P. Havu, V. Havu, X. Ren, K. Reuter, and M. Scheffler, Comp. Phys. Comm. **180**, 2175 (2009).

[2] A. H. Larsen, J. J. Mortensen, J. Blomqvist, I. E. Castelli, R. Christensen, M. Dułak, J. Friis, M. N. Groves, B. Hammer, C. Hargus, E. D. Hermes, P. C. Jennings, P. B. Jensen, J. Kermode, J. R. Kitchin, E. L. Kolsbjerg, J. Kubal, K. Kaasbjerg, S. Lysgaard, J. B. Maronsson, T. Maxson, T. Olsen, L. Pastewka, A. Peterson, C. Rostgaard, J. Schiøtz, O. Schtt, M. Strange, K. S. Thygesen, T. Vegge, L. Vilhelmsen, M. Walter, Z. Zeng, and K. W. Jacobsen, J. Phys. Condens. Matter **29**, 273002 (2017).

[3] M. Koch, M. Pagan, M. Persson, S. Gawinkowski, J. Waluk, and T. Kumagai, J. Am. Chem. Soc. **139**, 12681 (2017).

[4] A. V. Krukau, O. A. Vydrov, A. F. Izmaylov, and G. E. Scuseria, J. Chem. Phys. **125**, 224106 (2006).

[5] V. G. Ruiz, W. Liu, E. Zojer, M. Scheffler, and A. Tkatchenko, Phys. Rev. Lett. **108**, 146103 (2012).

[6] J. P. Perdew, K. Burke, and M. Ernzerhof, Phys. Rev. Lett. **77**, 3865 (1996).

[7] J. Hermann and A. Tkatchenko, (2019), arXiv:1910.03073.

[8] M. Ceriotti, J. More, and D. E. Manolopoulos, Comp. Phys. Comm. **185**, 1019 (2014).

[9] V. Kapil, M. Rossi, O. Marsalek, R. Petraglia, Y. Litman, T. Spura, B. Cheng, A. Cuzzocrea, R. H. Meißner, D. M. Wilkins, B. A. Helfrecht, P. Juda, S. P. Bienvenue, W. Fang, J. Kessler, I. Poltavsky, S. Vandenbrande, J. Wieme, C. Corminboeuf, T. D. Kühne, D. E. Manolopoulos, T. E. Markland, J. O. Richardson, A. Tkatchenko, G. A. Tribello, V. V. Speybroeck, and M. Ceriotti, Comp. Phys. Comm. **236**, 214 (2019).

[10] Y. Litman, *Tunneling and Zero-Point Energy Effects in Multidimensional Hydrogen Transfer Reactions: From Gas Phase to Adsorption on Metal Surfaces*, Ph.D. thesis, Freie Universität Berlin (2020), *submitted*.

[11] Y. Litman, J. Behler, and M. Rossi, Faraday Discuss. **221**, 526 (2020).

[12] J. O. Richardson, Int. Rev. Phys. Chem. **37**, 171 (2018).

[13] Y. Zhang, J. B. Rommel, M. T. Cvita, and S. C. Althorpe, Phys. Chem. Chem. Phys. **16**,

24292 (2014).

[14] H. Eyring, J. Chem. Phys. **3**, 107 (1935).

[15] A. N. Beyer, J. O. Richardson, P. J. Knowles, J. Rommel, and S. C. Althorpe, J. Phys. Chem. Lett. **7**, 4374 (2016).

[16] T. Kumagai, J. N. Ladenthin, Y. Litman, M. Rossi, L. Grill, S. Gawinkowski, J. Waluk, and M. Persson, J. Chem. Phys. **148**, 102330 (2018).

[17] A. Garg, Am. J. Phys. **68**, 430 (2000).

5.6 Paper VI

"Decisive role of nuclear quantum effects on surface mediated water dissociation at finite temperature "

Y. Litman, D. Donadio, M. Ceriotti, and M. Rossi

J. Chem. Phys. ***148****, 102320 (2018)*

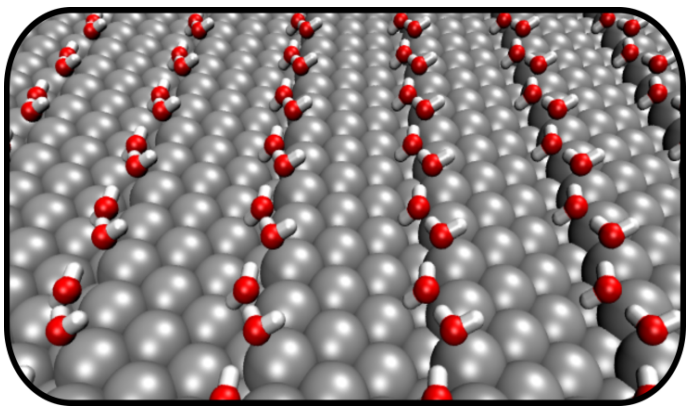

Figure 21: Paper VI graphical abstract created for this thesis.

URL: `https://doi.org/10.1063/1.5002537`

DOI: 10.1063/1.5002537

Author contributions: M. Rossi and I designed the research. The electronic structure calculations were performed by myself with the exception of the calculations of the Bader charges which were computed by D. Donadio. I also performed the MD and PIMD simulations. All the author analyzed the results and contributed to the writing of the manuscript.

Chapter 6

Conclusions and Outlook

The present work studies hydrogen dynamics in general, and hydrogen transfer in particular, and this thesis contributes to this research in several ways. Since these processes are usually governed by the interplay between NQE, anharmonic effects and multidimensional mode coupling, their description demands the juxtaposition of state-of-the-art methods requiring, in some cases, new approximations and code implementations. Even though a significant part of the thesis focuses on the DHT dynamics of the porphycene molecule, the new insights and knowledge obtained are rather general, and are expected to aid the understanding of many other systems as well.

Two distinctive features distinguish the work presented here from previous studies. First, all the quantitative results rely on *ab initio* theories. In some cases, previous semi-empirical theories are supported by the presented results and, in many other cases, their limitations are exposed. Second, all the relevant effects mentioned above (NQE, anharmonic effects and multidimensional mode coupling) are included in the DHT description superseding previous works where one or many of those effects were left out. In this work, the three effects were shown to be essential to get quantitative and even qualitative predictions.

One portion of this thesis deals with the study of DHT rates and IR spectra of the porphycene molecule in gas-phase. In both cases, the coupling of low-frequencies classical-like modes that modulate the molecule skeleton profoundly influences the dynamics of the high-frequency quantized modes. The calculated DHT rates and vibrational spectrum are in close agreement with experimental results. Temperature dependence studies were also carried out. The DHT mechanism was found to change with temperature, being concerted at low temperatures and stepwise at higher ones. Additionally, the two main activated channels that govern the DHT were identified, and the experimentally observed activation energies explained. The studies on the vibrational spectra predict a blue-shift of the NH stretch band with increasing temperature. Moreover, these studies reveal that the red-shift with temperature seen in classical-nuclei simulations is the result of a fictitious competition of effects, which is absent when NQE are taken into account.

The Born-Oppenheimer approximation is the cornerstone approximation used through this thesis, separating the so-called nuclear and electronic problems. For the questions addressed here,

where non-adiabatic effects, as well as nuclear exchange and coherence are of minor relevance, the final accuracy seems to be limited by how the electronic problem is solved and the quality of the generated PES. While for gas-phase molecules, CCSD(T) represents a high-quality standard to rely on, which delivers the excellent agreement obtained in the gas phase studies, it is not possible to find an analogous reference method for extended systems. While reasonably good and efficient approximations exist for solids and molecules separately, most of them fail to maintain their quality when used to describe molecule-solid interfaces. Thus, the lack of a reference method to benchmark against, hampers further progress in efficient methods to describe molecule-solid interfaces and limits its current predictive power. However, current progress on range separated XC functionals, periodic CCSD [295,296] and quantum Monte Carlo methods [110,297] are promising to deliver upgraded approximations and reference reliable values in a near future.

Complementary to electronic structure theory developments, machine learning methods applied to atomistic simulations are quicky becoming an indispensable tool. The basic idea is that given a set of reference values, one would like to have the best smooth interpolation of them that fulfills specific properties. For example, HDNNP were used in this thesis to perform 500 ns of simulations at a hybrid DFA level based solely on data from previous simulations and at almost no extra computational cost. Different combinations of RPI with machine learning techniques have also appeared in the literature recently [298,299]. Another good example is the MD simulations performed at the CCSD(T) level of theory by using a symmetrized gradient-domain machine learning model [300]. Such a task would not be affordable without machine learning techniques. Simultaneous improvements on more accurate and affordable reference methods, together with modern machine learning methods with less demanding requirements, i.e., smaller training sets, could boost the accuracy of atomic simulations. As a consequence, the theoretical predictive power for bigger and more complex systems will considerably increase. However, probably the most exciting outcome of better simulations is not its augmented accuracy, but rather the elucidation of new physical effects that may be show up from the discrepancies between high-quality well-controlled experiments and simulations.

Another portion of this thesis studies the DHT dynamics when the porphycene molecule is adsorbed on metal surfaces. Contrary to the gas phase scenario, one should acknowledge the current limitations of the methodology in terms of accuracy and predictive power. Overall, the results should be considered as semi-quantitative, and the comparison with well-controlled experiments helps to obtain robust conclusions. Nonetheless, one should not underestimate the insights that simulations bring to the increasing complex experimental observations. The results presented here are just one example of such insights. RPI calculations were performed to compute DHT rates for porphycene molecule on Cu(110) and Ag(110). In the two cases, the DHT mechanism was elucidated and contrasted with experiments. At intermediate temperatures, $\approx$ 100K, the computed rates are in better agreement with experiments since the calculations are less sensitive to the PES quality. At much lower temperatures, further deviations from experimental results are observed, especially for the concerted DHT mechanism. Nevertheless, the observed sharp change of DHT

rates when the temperature is lowered below 13K were successfully traced back to a change in the DHT mechanism. On the whole, RPI proved to be an efficient method to study hydrogen transfer of molecules on surfaces when there are only a few possible initial and final states, and therefore the tunneling processes can be represented with high fidelity by one or two main pathways.

A third portion of the thesis considers a more flexible system relevant to model catalytic reactions. Specifically, the water dissociation on the stepped Pt(221) surface is studied. The simulations indicate that NQE and anharmonicity of the PES favor the dissociation reaction significantly and also affect electronic observables like the WFC. In addition, the SL-RPC approximation scheme, which aims to reduce the computation cost associated with the inclusion of NQE on weakly bound systems, was proposed and benchmarked in this system. The simulations showed that SL-RPC allows simulating intact water structures on the Pt surface at classical computational cost with almost no loss in accuracy, whereas dissociated structures, where a hydrogen atom binds to the surface, cannot be treated as a weakly bound system, and consequently do not benefit much from this approach. To estimate the suitability of the approximation without the need to perform costly calculations, easy to compute descriptors based on harmonic frequencies are introduced.

Theory development is the main starting point of any significant advance in computational physics and chemistry. However, these theories only grow beyond specialized groups and start being used by the rest of the community when easy to use and reliable implementations become available. The times when each group used its own code and kept it private seem to be slowly being left behind. The whole community has started moving towards a new standard, where code sharing and reproducibility are not negotiable anymore[301,302]. In this context, a considerable portion of the work was dedicated to the implementation of RPI methods in the open-source code i-PI. Since i-PI already has a working interface with dozens of electronic structure and force-field codes, the new implementation is already accessible to all of the respective communities without any additional effort.

As a consequence of the specific traveled path, many roads left room for further exploration, and new avenues also appeared. An incomplete list of those ideas follows:

- The natural and simple next step would be to extend the current study to more molecules like porphyrin, phthalocyanines, or hemimorphycene, and the corresponding molecular derivatives[51] in order to develop rational design principles that can guide future synthetic research.

- Further exploration of the SL-RPC scheme in combination with multiple time steps algorithms[303], and its application within other path integral based methods like RPMD may be considered. Additionally, its application to other types of weakly bound systems like molecular crystals also deserves a closer look.

- The emergence of tunneling control reactions as a new reactivity paradigm in chemistry[304,305] is an attractive field where the RPI rate theory may be interesting to apply.

- Recent experimental advances on tip-enhanced Raman spectroscopy have reached the impressive goal of visualizing normal modes[306]. However, the interpretation of the observed

signal is rarely an easy task, and therefore, simulations are needed when deconvoluting it. This new and active field may bring new insights into the molecular dynamics on surfaces and therefore represents a new exciting path to follow.

- A more ambitious, and naturally more challenging, goal would be to go beyond the BOA and consider non-adiabatic effects. One possibility, if dealing with a metallic surface, is to consider the so-called electronic friction[307], where temperature and adsorbate movement can induce electronic excitations that, in turn, affect the adsorbate dynamics. A second avenue would be to combine the RPI rate theory with non-equilibrium green functions to generate a bias dependent PES[308], and simulate the hydrogen transfer process of adsorbate under an external bias voltage.

- Another provocative avenue would depart from the equilibrium condition and would study non-equilibrium hydrogen transfer rates. Several groups[17,29,34,60,309] have shown that it is possible to trigger the hydrogen transfer reaction by vibrational excitation of skeleton modes by inelastic scattering of electrons, but it is not clear how the energy flows from the vibrationally excited mode to the reactive one. A possible way to perform these simulations could be based on RPMD[310] or combination of the δ-thermostat[311,312] with PIGLET[190].

It is evident that even though much progress has been made, still many exciting questions remain unsolved. The author of this thesis hopes that the results presented here stimulate more theoretical work on the study of dynamics of molecules on surfaces, closing the gap between theory and experiments, and bringing new physical insights to this fascinating and active field.

Appendix

Details of Instanton Calculations in Chapter 3

The description of the system used to prepare the guidelines outlined in Chapter 3 are presented in Tab. 1.

System #	Reaction type	T_c (K)	Barrier sym.	PES	DOF	N.T.A.
1	intermolecular	240	symmetric	analytic formula	1	1
2	intramolecular	184	symmetric	numerical fit	27	1
3	intermolecular	282	asymmetric	*ab initio*	24	2
4	intermolecular	340	asymmetric	numerical fit	18	1
5	intramolecular	287	asymmetric	numerical fit	114	1

Table 1: N.T.A. and DOF stand for the number of tunneling atoms and nuclear degrees of freedom, respectively. *System 1*: Eckart barrier with the same parameter as used in Ref. 270. *System 2*: malonaldehyde intramolecular hydrogen transfer, fitted neural network on DFA data (PBE+vdW[147]). *System 3*: $BH_3NH_3 \rightarrow BH_2NH_2 + H_2$. DFA (PBE+vdW[147]). *System 4*: $CH_4 + H \rightarrow CH_3 + H_2$, CBE potential[313]. *System 5*: Porphycene *trans* → *cis*. Fitted neural network described in Ref. 294.

Convergence

The convergence of the tunneling rates for the different models are shown in the following tables. Only models that represent realistic reactions are presented.

T/T_c	0.75			0.50			0.25		
$P \times T/T_c$	20	40	80	20	44	88	21	44	87
Error	-23	-6	0	-23	-5	0	-24	-6	0

Table 2: Rate convergence for system 2. The error is defined as $\frac{Rate(P)-Rate(P\rightarrow\infty)}{Rate(P\rightarrow\infty)} \times 100$.

T/T_c	0.75			0.50			0.25		
$P \times T/T_c$	21	42	83	21	42	84	25	51	102
Error	-6	-1	0	9	2	0	30	5	0

Table 3: Rate convergence for system 3. See caption in Tab. 2 for error definition.

T/T_c	0.75			0.50			0.25		
$P \times T/T_c$	21	42	84	22	42	85	20	40	80
Error	-2	-1	0	13	3	0	63	11	0

Table 4: Rate convergence for system 4. See caption in Tab. 2 for error definition.

T/T_c	0.75			0.50			0.25		
$P \times T/T_c$	22	43	85	22	42	85	20	40	62
Error	-15	3	0	-19	-4	0	-26	-6	0

Table 5: Rate convergence for system 5. See caption in Tab. 2 for error definition.

Curriculum Vitae

For reasons of data protection, the curriculm vitae is not included in the online version.

Bibliography

[1] Hynes, J. T.; Klinman, J. P.; Limbach, H.; Schowen, R. L. *Hydrogen-Transfer Reactions*; Wiley-VCH Verlag GmbH and Co. KGaA, 2007.

[2] Kraytsberg, A.; Ein-Eli, Y. *Energy Fuels* **2014**, *28*, 7303–7330.

[3] Peruzzini, M.; Poli, R. *Recent Advances in Hydride Chemistry*; Elsevier: Amsterdam, 2001.

[4] Eigen, M. *Angew. Chem. Int. Ed.* **1964**, *3*, 1–19.

[5] McNaught, A. D.; Wilkinson, A. *Compendium of Chemical Terminology, 2nd ed.*; Blackwell Scientific Publications, Oxford, 1997.

[6] Pospisil, P.; Ballmer, P.; Scapozza, L.; Folkers, G. *J. Recept. Signal Transduct.* **2003**, *23*, 361–371.

[7] Wojnarowska, Z.; Wlodarczyk, P.; Kaminski, K.; Grzybowska, K.; Hawelek, L.; Paluch, M. *J. Chem. Phys.* **2010**, *133*, 094507.

[8] Zhu, C.; Lu, L.; Zhang, J.; Yue, Z.; Song, J.; Zong, S.; Liu, M.; Stovicek, O.; Gao, Y. Q.; Yi, C. *Proc. Natl. Acad. Sci. U.S.A.* **2016**, *113*, 7792–7797.

[9] Li, D.; Fedeles, B. I.; Singh, V.; Peng, C. S.; Silvestre, K. J.; Simi, A. K.; Simpson, J. H.; Tokmakoff, A.; Essigmann, J. M. *Proc. Natl. Acad. Sci. U.S.A.* **2014**, *111*, 3252–3259.

[10] Peng, C. S.; Fedeles, B. I.; Singh, V.; Li, D.; Amariuta, T.; Essigmann, J. M.; Tokmakoff, A. *Proc. Natl. Acad. Sci. U.S.A.* **2015**, *112*, 3229–3234.

[11] Pérez, A.; Tuckerman, M. E.; Hjalmarson, H. P.; von Lilienfeld, O. A. *J. Am. Chem. Soc.* **2010**, *132*, 11510–11515.

[12] Antonov, L. *Tautomerism: Concepts and Applications in Science and Technology.*; Wiley-VCH Verlag GmbH and Co. KGaA, 2016.

[13] Gawinkowski, S.; Walewski, L.; Vdovin, A.; Slenczka, A.; Rols, S.; Johnson, M. R.; Lesyng, B.; Waluk, J. *Phys. Chem. Chem. Phys.* **2012**, *14*, 5489–5503.

[14] Reeves, R. L.; Maggio, M. S.; Costa, L. F. *J. Am. Chem. Soc.* **1974**, *96*, 5917–5925.

[15] Gilli, G.; Bellucci, F.; Ferretti, V.; Bertolasi, V. *J. Am. Chem. Soc.* **1989**, *111*, 1023–1028.

[16] Claramunt, R.; López, C.; María, M. S.; Sanz, D.; Elguero, J. *Prog. Nucl. Mag. Res. Sp.* **2006**, *49*, 169–206.

[17] Liljeroth, P.; Repp, J.; Meyer, G. *Science* **2007**, *317*, 1203–1206.

[18] Binnig, G.; Rohrer, H.; Gerber, C.; Weibel, E. *Phys. Rev. Lett.* **1982**, *49*, 57–61.

[19] Binnig, G.; Quate, C. F.; Gerber, C. *Phys. Rev. Lett.* **1986**, *56*, 930–933.

[20] Voigtländer, B. *Scanning Probe Microscopy*; Springer, Berlin, Heidelberg, 2015.

[21] Giessibl, F. J. *Science* **1995**, *267*, 68–71.

[22] Gross, L.; Mohn, F.; Moll, N.; Liljeroth, P.; Meyer, G. *Science* **2009**, *325*, 1110–1114.

[23] Eigler, D. M.; Schweizer, E. K. *Nature* **1990**, *344*, 524–526.

[24] Crommie, M. F.; Lutz, C. P.; Eigler, D. M. *Science* **1993**, *262*, 218–220.

[25] Stipe, B. C.; Rezaei, M. A.; Ho, W. *Science* **1998**, *280*, 1732–1735.

[26] Le Ru, E. C.; Etchegoin, P. G. *Annu. Rev. Phys. Chem.* **2012**, *63*, 65–87.

[27] Du, S.; Yoshida, K.; Zhang, Y.; Hamada, I.; Hirakawa, K. *Nat. Photonics* **2018**, *12*, 608–612.

[28] Auwärter, W.; Seufert, K.; Bischoff, F.; Ecija, D.; Vijayaraghavan, S.; Joshi, S.; Klappenberger, F.; Samudrala, N.; Barth, J. V. *Nat. Nanotechnol.* **2012**, *7*, 41–46.

[29] Kumagai, T.; Hanke, F.; Gawinkowski, S.; Sharp, J.; Kotsis, K.; Waluk, J.; Persson, M.; Grill, L. *Phys. Rev. Lett.* **2013**, *111*, 246101.

[30] Ladenthin, J. N.; Frederiksen, T.; Persson, M.; Sharp, J. C.; Gawinkowski, S.; Waluk, J.; Kumagai, T. *Nat. Chem.* **2016**, *8*, 935–940.

[31] Ladenthin, J. N.; Grill, L.; Gawinkowski, S.; Liu, S.; Waluk, J.; Kumagai, T. *ACS Nano* **2015**, *9*, 7287–7295.

[32] Kumagai, T.; Hanke, F.; Gawinkowski, S.; Sharp, J.; Kotsis, K.; Waluk, J.; Persson, M.; Grill, L. *Nat. Chem.* **2014**, *6*, 41–46.

[33] Böckmann, H.; Liu, S.; Mielke, J.; Gawinkowski, S.; Waluk, J.; Grill, L.; Wolf, M.; Kumagai, T. *Nano Lett.* **2016**, *16*, 1034–1041.

[34] Kügel, J.; Leisegang, M.; Bode, M. *ACS Nano* **2018**, *12*, 8733–8738.

[35] Sperl, A.; Kröger, J.; Berndt, R. *Angew. Chem. Int. Ed.* **2011**, *50*, 5294–5297.

[36] Tersoff, J.; Hamann, D. R. *Phys. Rev. B* **1985**, *31*, 805–813.

[37] Tremblay, J. C.; Blanco-Rey, M. *Phys. Chem. Chem. Phys.* **2015**, *17*, 13973–13983.

[38] Ueba, H.; Mii, T.; Lorente, N.; Persson, B. N. J. *J. Chem. Phys.* **2005**, *123*, 084707.

[39] Vogel, E.; Köcher, M.; Schmickler, H.; Lex, J. *Angew. Chem. Int. Ed.* **1986**, *25*, 257–259.

[40] Waluk, J. *Chem. Rev.* **2017**, *117*, 2447–2480.

[41] Stockert, J. C.; Canete, M.; Juarranz, A.; Villanueva, A.; Horobin, R. W.; Borrell, J. I.; Teixido, J.; Nonell, S. *Curr. Med. Chem.* **2007**, *14*, 997–1026.

[42] Masiera, N.; Bojarska, A.; Gawryszewska, I.; Sadowy, E.; Hryniewicz, W.; Waluk, J. *J. of Photochem. Photobiol. B* **2017**, *174*, 84–89.

[43] Berlicka, A.; König, B. *Photochem. Photobiol. Sci.* **2010**, *9*, 1359–1366.

[44] Oohora, K.; Kihira, Y.; Mizohata, E.; Inoue, T.; Hayashi, T. *J. Am. Chem. Soc.* **2013**, *135*, 17282–17285.

[45] Saeki, H.; Kurimoto, O.; Nakaoka, H.; Misaki, M.; Kuzuhara, D.; Yamada, H.; Ishida, K.; Ueda, Y. *J. Mater. Chem. C* **2014**, *2*, 5357–5364.

[46] Hayashi, T.; Dejima, H.; Matsuo, T.; Sato, H.; Murata, D.; Hisaeda, Y. *J. Am. Chem. Soc.* **2002**, *124*, 11226–11227.

[47] Matsuo, T.; Murata, D.; Hisaeda, Y.; Hori, H.; Hayashi, T. *J. Am. Chem. Soc.* **2007**, *129*, 12906–12907.

[48] Wang, Q.; Song, X.; Li, P.; Bu, Y. *J. Phys. Chem. C* **2019**, *123*, 10764–10776.

[49] Vdovin, A.; Waluk, J.; Dick, B.; Slenczka, A. *Chem. Phys. Chem.* **2009**, *10*, 761–765.

[50] Mengesha, E. T.; Sepioł, J.; Borowicz, P.; Waluk, J. *J. Chem. Phys.* **2013**, *138*, 174201.

[51] Ciąćka, P.; Fita, P.; Listkowski, A.; Kijak, M.; Nonell, S.; Kuzuhara, D.; Yamada, H.; Radzewicz, C.; Waluk, J. *J. Phys. Chem. B* **2015**, *119*, 2292–2301.

[52] Piatkowski, L.; Schanbacher, C.; Wackenhut, F.; Jamrozik, A.; Meixner, A. J.; Waluk, J. *J. Phys. Chem. Lett.* **2018**, *9*, 1211–1215.

[53] Chizhik, A. M.; Jäger, R.; Chizhik, A. I.; Bär, S.; Mack, H.-G.; Sackrow, M.; Stanciu, C.; Lyubimtsev, A.; Hanack, M.; Meixner, A. J. *Phys. Chem. Chem. Phys.* **2011**, *13*, 1722–1733.

[54] Mengesha, E. T.; Zehnacker-Rentien, A.; Sepioł, J.; Kijak, M.; Waluk, J. *J. Phys. Chem. B* **2015**, *119*, 2193–2203.

[55] Gil, M.; Dobkowski, J.; Wiosna-Sałyga, G.; Urbańska, N.; Fita, P.; Radzewicz, C.; Pietraszkiewicz, M.; Borowicz, P.; Marks, D.; Glasbeek, M.; Waluk, J. *J. Am. Chem. Soc.* **2010**, *132*, 13472–13485.

[56] Gil, M.; Waluk, J. *J. Am. Chem. Soc.* **2007**, *129*, 1335–1341.

[57] Fita, P.; Urbańska, N.; Radzewicz, C.; Waluk, J. *Chem.: Eur. J.* **2009**, *15*, 4851–4856.

[58] Ciąćka, P.; Fita, P.; Listkowski, A.; Radzewicz, C.; Waluk, J. *J. Phys. Chem. Lett.* **2016**, *7*, 283–288.

[59] Malsch, K.; Hohlneicher, G. *J. Phys. Chem. A* **1997**, *101*, 8409–8416.

[60] Kügel, J.; Leisegang, M.; Böhme, M.; Krönlein, A.; Sixta, A.; Bode, M. *Nano Lett.* **2017**, *17*, 5106–5112.

[61] Koch, M.; Pagan, M.; Persson, M.; Gawinkowski, S.; Waluk, J.; Kumagai, T. *J. Am. Chem. Soc. .* **2017**, *139*, 12681–12687.

[62] Limbach, H.-H.; Hennig, J.; Gerritzen, D.; Rumpel, H. *Faraday Discuss. Chem. Soc.* **1982**, *74*, 229–243.

[63] Schlabach, M.; Limbach, H. H.; Bunnenberg, E.; Shu, A. Y. L.; Tolf, B. R.; Djerassi, C. *J. Am. Chem. Soc.* **1993**, *115*, 4554–4565.

[64] Braun, J.; Limbach, H.-H.; Williams, P. G.; Morimoto, H.; Wemmer, D. E. *J. Am. Chem. Soc.* **1996**, *118*, 7231–7232.

[65] Lopez del Amo, J. M.; Langer, U.; Torres, V.; Pietrzak, M.; Buntkowsky, G.; Vieth, H.-M.; Shibl, M. F.; Kühn, O.; Bröring, M.; Limbach, H.-H. *J. Phys. Chem. A* **2009**, *113*, 2193–2206.

[66] Pietrzak, M.; Shibl, M. F.; Bröring, M.; Kühn, O.; Limbach, H.-H. *J. Am. Chem. Soc.* **2007**, *129*, 296–304.

[67] Shibl, M. F.; Pietrzak, M.; Limbach, H.-H.; Kühn, O. *Chem. Phys. Chem.* **2007**, *8*, 315–321.

[68] Smedarchina, Z.; Shibl, M.; Kühn, O.; Fernández-Ramos, A. *Chem. Phys. Lett.* **2007**, *436*, 314–321.

[69] Smedarchina, Z.; Siebrand, W.; Fernández-Ramos, A. *J. Chem. Phys.* **2014**, *141*, 174312.

[70] Smedarchina, Z.; Siebrand, W.; Fernández-Ramos, A. *J. Chem. Phys.* **2007**, *127*, 174513.

[71] Smedarchina, Z.; Zgierski, M. Z.; Siebrand, W.; Kozlowski, P. M. *J. Chem. Phys.* **1998**, *109*, 1014–1024.

[72] Limbach, H.-H.; Klein, O.; Lopez Del Amo, J. M.; Elguero, J. *Zeitschrift für Physikalische Chemie* **2004**, *217*, 17–49.

[73] Gerritzen, D.; Limbach, H. H. *J. Am. Chem. Soc.* **1984**, *106*, 869–879.

[74] Scherer, G.; Limbach, H. H. *J. Am. Chem. Soc.* **1989**, *111*, 5946–5947.

[75] Lopez, J. M.; Männle, F.; Wawer, I.; Buntkowsky, G.; Limbach, H.-H. *Phys. Chem. Chem. Phys.* **2007**, *9*, 4498–4513.

[76] Braun, J.; Koecher, M.; Schlabach, M.; Wehrle, B.; Limbach, H.-H.; Vogel, E. *J. Am. Chem. Soc.* **1994**, *116*, 6593–6604.

[77] Walewski, L.; Waluk, J.; Lesyng, B. *J. Phys. Chem. A* **2010**, *114*, 2313–2318.

[78] Yoshikawa, T.; Sugawara, S.; Takayanagi, T.; Shiga, M.; Tachikawa, M. *Chem. Phys.* **2012**, *394*, 46–51.

[79] Yoshikawa, T.; Sugawara, S.; Takayanagi, T.; Shiga, M.; Tachikawa, M. *Chem. Phys. Lett.* **2010**, *496*, 14–19.

[80] Liu, S.; Baugh, D.; Motobayashi, K.; Zhao, X.; Levchenko, S. V.; Gawinkowski, S.; Waluk, J.; Grill, L.; Persson, M.; Kumagai, T. *Phys. Chem. Chem. Phys.* **2018**, *20*, 12112–12119.

[81] Li, J.; Yang, S.; Ren, J.-C.; Su, G.; Li, S.; Butch, C. J.; Ding, Z.; Liu, W. *J. Phys. Chem. Lett.* **2019**, *10*, 6755–6761.

[82] Novko, D.; Tremblay, J. C.; Blanco-Rey, M. *J. Chem. Phys.* **2017**, *147*, 169901.

[83] Novko, D.; Tremblay, J. C.; Blanco-Rey, M. *J. Chem. Phys.* **2016**, *145*, 244701.

[84] Novko, D.; Blanco-Rey, M.; Tremblay, J. C. *J. Phys. Chem. Lett.* **2017**, *8*, 1053–1059.

[85] Zhang, J. L.; Zhong, J. Q.; Lin, J. D.; Hu, W. P.; Wu, K.; Xu, G. Q.; Wee, A. T. S.; Chen, W. *Chem. Soc. Rev.* **2015**, *44*, 2998–3022.

[86] Qiu, X. H.; Nazin, G. V.; Ho, W. *Phys. Rev. Lett.* **2004**, *93*, 196806.

[87] Qu, C.; Bowman, J. M. *Phys. Chem. Chem. Phys.* **2019**, *21*, 3397–3413.

[88] Parr, R. G.; Yang, W. *Density Functional Theory of Atoms and Molecules*; Oxford University Press, 1994.

[89] Dreizler, R. M.; Gross, E. K. U. *Density Functional Theory: An Approach to the Quantum Many-Body Problem*; Springer-Verlag, Berlin Heidelberg, 1990.

[90] Engel, E.; Dreizler, R. M. *Density Functional Theory: And Advanced Course*; Springer-Verlag,Berlin,Heidelberg, 2011.

[91] Tuckerman, M. *Statistical Mechanics: Theory and Molecular Simulation*; Oxford University Press, 2010.

[92] Allen, M. P.; Tildesley, D. J. *Compute Simulations of Liquids*; Oxford University Press, 1987.

[93] Marx, D.; Hutter, J. *Ab Initio Molecular Dynamics: Basic Theory and Advanced Methods*; Cambridge University Press, Cambridge, 2009.

[94] Born, M.; Oppenheimer, R. *Ann. Phys.* **1927**, *389*, 457–484.

[95] Born, M.; Huang, K. *Dynamical Theory of Crystal Lattices*; Oxford University Press, 1954.

[96] Worth, G. A.; Cederbaum, L. S. *Annu. Rev. Phys. Chem.* **2004**, *55*, 127–158.

[97] Pisana, S.; Lazzeri, M.; Casiraghi, C.; Novoselov, K. S.; Geim, A. K.; Ferrari, A. C.; Mauri, F. *Nat. Mater.* **2007**, *6*, 198–201.

[98] White, J. D.; Chen, J.; Matsiev, D.; Auerbach, D. J.; Wodtke, A. M. *Nature* **2005**, *433*, 503–505.

[99] Neese, F.; Atanasov, M.; Bistoni, G.; Maganas, D.; Ye, S. *J. Am. Chem. Soc.* **2019**, *141*, 2814–2824.

[100] Hartree, D. R. *Math. Proc. Camb. Philos. Soc.* **1928**, *24*, 89–110.

[101] Slater, J. C. *Phys. Rev.* **1929**, *34*, 1293–1322.

[102] Fock, V. *Zeitschrift für Physik* **1930**, *61*, 126–148.

[103] Møller, C.; Plesset, M. S. *Phys. Rev.* **1934**, *46*, 618–622.

[104] Cremer, D. *WIREs Comput. Mol. Sci.* **2011**, *1*, 509–530.

[105] Cremer, D.; He, Z. *J. Phys. Chem.* **1996**, *100*, 6173–6188.

[106] Neese, F.; Hansen, A.; Liakos, D. G. *J. Chem. Phys.* **2009**, *131*, 064103.

[107] Riplinger, C.; Neese, F. *J. Chem. Phys.* **2013**, *138*, 034106.

[108] Szalay, P. G.; Müller, T.; Gidofalvi, G.; Lischka, H.; Shepard, R. *Chem. Rev.* **2012**, *112*, 108–181.

[109] Evangelista, F. A. *J. Chem. Phys.* **2018**, *149*, 030901.

[110] Zen, A.; Brandenburg, J. G.; Klimeš, J.; Tkatchenko, A.; Alfè, D.; Michaelides, A. *Proc. Natl. Acad. Sci. U.S.A.* **2018**, *115*, 1724–1729.

[111] Hermann, J.; Schätzle, Z.; Noé, F. **2019**, arXiv:1909.08423.

[112] Pfau, D.; Spencer, J. S.; Matthews, A. G. d. G.; Foulkes, W. M. C. **2019**,

[113] Hohenberg, P.; Kohn, W. *Phys. Rev.* **1964**, *136*, 864–871.

[114] Levy, M. *Proc. Natl. Acad. Sci. U.S.A.* **1979**, *76*, 6062–6065.

[115] Lieb, E. H. *Int. J. Quantum Chem.* **1983**, *24*, 243–277.

[116] Kohn, W.; Sham, L. J. *Phys. Rev.* **1965**, *140*, 1133–1138.

[117] Wesolowski, T. A.; Wang, Y. A. *Recent Progress in Orbital-free Density Functional Theory*; World Scientific, 2013.

[118] Witt, W. C.; del Rio, B. G.; Dieterich, J. M.; Carter, E. A. *J. Mater. Res.* **2018**, *33*, 777–795.

[119] Janak, J. F. *Phys. Rev. B* **1978**, *18*, 7165–7168.

[120] Stowasser, R.; Hoffmann, R. *J. Am. Chem. Soc.* **1999**, *121*, 3414–3420.

[121] Cohen, A. J.; Mori-Sánchez, P.; Yang, W. *Chem. Rev.* **2012**, *112*, 289–320.

[122] Langreth, D. C.; Perdew, J. P. *Phys. Rev. B* **1977**, *15*, 2884–2901.

[123] Harris, J.; Jones, R. O. *J. Phy. F: Met. Phys.* **1974**, *4*, 1170–1186.

[124] Sun, J.; Ruzsinszky, A.; Perdew, J. P. *Phys. Rev. Lett.* **2015**, *115*, 036402.

[125] Lehtola, S.; Steigemann, C.; Oliveira, M. J.; Marques, M. A. *SoftwareX* **2018**, *7*, 1–5.

[126] Goerigk, L.; Grimme, S. *Phys. Chem. Chem. Phys.* **2011**, *13*, 6670–6688.

[127] Mardirossian, N.; Head-Gordon, M. *Mol. Phys.* **2017**, *115*, 2315–2372.

[128] Koch, W.; Holthausen, M. C. *A Chemist's Guide to Density Functional Theory, Second Edition*; Wiley-VCH Verlag GmbH, 2001.

[129] Sousa, S. F.; Fernandes, P. A.; Ramos, M. J. *J. Phys. Chem. A* **2007**, *111*, 10439–10452.

[130] Perdew, J. P.; Burke, K.; Ernzerhof, M. *Phys. Rev. Lett.* **1996**, *77*, 3865–3868.

[131] Ernzerhof, M.; Scuseria, G. E. *J. Chem. Phys.* **1999**, *110*, 5029–5036.

[132] Zhang, G.-X.; Reilly, A. M.; Tkatchenko, A.; Scheffler, M. *New J. Phys.* **2018**, *20*, 063020.

[133] Haas, P.; Tran, F.; Blaha, P. *Phys. Rev. B* **2009**, *79*, 085104.

[134] Gillan, M. J.; Alfè, D.; Michaelides, A. *J. Chem. Phys.* **2016**, *144*, 130901.

[135] Barone, V.; Orlandini, L.; Adamo, C. *Chem. Phys. Lett.* **1994**, *231*, 295–300.

[136] Becke, A. D. *J. Chem. Phys.* **1993**, *98*, 5648–5652.

[137] Lee, C.; Yang, W.; Parr, R. G. *Phys. Rev. B* **1988**, *37*, 785–789.

[138] Vosko, S. H.; Wilk, L.; Nusair, M. *Can. J. Phys.* **1980**, *58*, 1200–1211.

[139] Stephens, P. J.; Devlin, F. J.; Chabalowski, C. F.; Frisch, M. J. *J. Phys. Chem.* **1994**, *98*, 11623–11627.

[140] Perdew, J. P.; Ernzerhof, M.; Burke, K. *J. Chem. Phys.* **1996**, *105*, 9982–9985.

[141] Paier, J.; Marsman, M.; Kresse, G. *J. Chem. Phys.* **2007**, *127*, 024103.

[142] Janesko, B. G.; Henderson, T. M.; Scuseria, G. E. *Phys. Chem. Chem. Phys.* **2009**, *11*, 443–454.

[143] Krukau, A. V.; Vydrov, O. A.; Izmaylov, A. F.; Scuseria, G. E. *J. Chem. Phys.* **2006**, *125*, 224106.

[144] Klimeš, J.; Michaelides, A. *J. Chem. Phys.* **2012**, *137*, 120901.

[145] Hermann, J.; DiStasio, R. A.; Tkatchenko, A. *Chem. Rev.* **2017**, *117*, 4714–4758.

[146] Grimme, S.; Antony, J.; Ehrlich, S.; Krieg, H. *J. Chem. Phys.* **2010**, *132*, 154104.

[147] Tkatchenko, A.; Scheffler, M. *Phys. Rev. Lett.* **2009**, *102*, 073005.

[148] Ruiz, V. G.; Liu, W.; Zojer, E.; Scheffler, M.; Tkatchenko, A. *Phys. Rev. Lett.* **2012**, *108*, 146103.

[149] Klein, B. P.; Morbec, J. M.; Franke, M.; Greulich, K. K.; Sachs, M.; Parhizkar, S.; Bocquet, F. C.; Schmid, M.; Hall, S. J.; Maurer, R. J.; Meyer, B.; Tonner, R.; Kumpf, C.; Kratzer, P.; Gottfried, J. M. *J. Phys. Chem. C* **2019**, *123*, 29219–29230.

[150] Tkatchenko, A.; DiStasio, R. A.; Car, R.; Scheffler, M. *Phys. Rev. Lett.* **2012**, *108*, 236402.

[151] Dion, M.; Rydberg, H.; Schröder, E.; Langreth, D. C.; Lundqvist, B. I. *Phys. Rev. Lett.* **2004**, *92*, 246401.

[152] Vydrov, O. A.; Van Voorhis, T. *Phys. Rev. Lett.* **2009**, *103*, 063004.

[153] Klimeš, J.; Michaelides, A. *J. Chem. Phys.* **2012**, *137*, 120901.

[154] Feynman, R. P. *Phys. Rev.* **1939**, *56*, 340–343.

[155] Pulay, P. *Mol. Phys.* **1969**, *17*, 197–204.

[156] Blum, V.; Gehrke, R.; Hanke, F.; Havu, P.; Havu, V.; Ren, X.; Reuter, K.; Scheffler, M. *Comput. Phys. Commun.* **2009**, *180*, 2175–2196.

[157] Kohn, W. *Phys. Rev. Lett.* **1996**, *76*, 3168–3171.

[158] Baer, R.; Head-Gordon, M. *Phys. Rev. Lett.* **1997**, *79*, 3962–3965.

[159] Galli, G.; Parrinello, M. *Phys. Rev. Lett.* **1992**, *69*, 3547–3550.

[160] Havu, V.; Blum, V.; Havu, P.; Scheffler, M. *J. Comput. Phys.* **2009**, *228*, 8367–8379.

[161] Skylaris, C.-K.; Haynes, P. D.; Mostofi, A. A.; Payne, M. C. *J. Chem. Phys.* **2005**, *122*, 084119.

[162] Gale, J. D. *Computational Methods for Large Systems*; John Wiley & Sons, Ltd, 2011; Chapter 2, pp 45–75.

[163] zhe Yu, V. W.; Corsetti, F.; García, A.; Huhn, W. P.; Jacquelin, M.; Jia, W.; Lange, B.; Lin, L.; Lu, J.; Mi, W.; Seifitokaldani, A.; Álvaro Vázquez-Mayagoitia,; Yang, C.; Yang, H.; Blum, V. *Comp. Phys. Commun.* **2018**, *222*, 267–285.

[164] Ochsenfeld, C.; White, C. A.; Head-Gordon, M. *J. Chem. Phys* **1998**, *109*, 1663–1669.

[165] Ihrig, A. C.; Wieferink, J.; Zhang, I. Y.; Ropo, M.; Ren, X.; Rinke, P.; Scheffler, M.; Blum, V. *New J. Phys.* **2015**, *17*, 093020.

[166] Ashcroft, N. W.; Mermin, N. D. *Solid State Physics*; Thomson Learning, London, 1976.

[167] McQuarrie, D. A. *Statistical mechanics*; University Science Books, 2000.

[168] Martyna, G. J.; Klein, M. L.; Tuckerman, M. *J. Chem. Phys.* **1992**, *97*, 2635–2643.

[169] Hoover, W. G. *Phys. Rev. A* **1985**, *31*, 1695–1697.

[170] Bussi, G.; Donadio, D.; Parrinello, M. *J. Chem. Phys.* **2007**, *126*, 014101.

[171] Ceriotti, M.; Bussi, G.; Parrinello, M. *Phys. Rev. Lett.* **2009**, *102*, 020601.

[172] Wang, F.; Landau, D. P. *Phys. Rev. E* **2001**, *64*, 056101.

[173] Metropolis, N.; Rosenbluth, A. W.; Rosenbluth, M. N.; Teller, A. H.; Teller, E. *J. Chem. Phys.* **1953**, *21*, 1087–1092.

[174] Hirshberg, B.; Rizzi, V.; Parrinello, M. *Proc. Natl. Acad. Sci. U.S.A.* **2019**, *116*, 21445–21449.

[175] Hirshberg, B.; Invernizzi, M.; Parrinello, M. **2020**, arXiv:2003.10317.

[176] Chandler, D.; Wolynes, P. G. *J. Chem. Phys.* **1981**, *74*, 4078–4095.

[177] Feynman, R. P.; Hibbs, A. R. *Quantum Mechanics and Path Integrals*; McGraw-Hill, 1965.

[178] Parrinello, M.; Rahman, A. *J. Chem. Phys.* **1984**, *80*, 860–867.

[179] Markland, T. E.; Ceriotti, M. *Nat. Rev. Chem.* **2018**, *2*, 0109.

[180] Sugita, Y.; Okamoto, Y. *Chem. Phys. Lett.* **1999**, *314*, 141–151.

[181] Barducci, A.; Bonomi, M.; Parrinello, M. *WIREs Comput. Mol. Sci.* **2011**, *1*, 826–843.

[182] Voter, A. F. *Phys. Rev. Lett.* **1997**, *78*, 3908–3911.

[183] Streett, W.; Tildesley, D.; Saville, G. *Mol. Phys.* **1978**, *35*, 639–648.

[184] Tuckerman, M.; Berne, B. J.; Martyna, G. J. *J. Chem. Phys.* **1992**, *97*, 1990–2001.

[185] Takahashi, M.; Imada, M. *J. Phys. Soc. Jpn.* **1984**, *53*, 3765–3769.

[186] Kapil, V.; Behler, J.; Ceriotti, M. *J. Chem. Phys.* **2016**, *145*, 234103.

[187] Poltavsky, I.; Tkatchenko, A. *Chem. Sci.* **2016**, *7*, 1368–1372.

[188] Poltavsky, I.; Kapil, V.; Ceriotti, M.; Kim, K. S.; Tkatchenko, A. *J. Chem. Theory Comput.* **2020**, *16*, 1128–1135.

[189] Ceriotti, M.; Manolopoulos, D. E.; Parrinello, M. *J. Chem. Phys.* **2011**, *134*, 084104.

[190] Ceriotti, M.; Manolopoulos, D. E. *Phys. Rev. Lett.* **2012**, *109*, 100604.

[191] Markland, T. E.; Manolopoulos, D. E. *J. Chem. Phys.* **2008**, *129*, 024105.

[192] Markland, T. E.; Manolopoulos, D. E. *Chem. Phys. Lett.* **2008**, *464*, 256–261.

[193] John, C.; Spura, T.; Habershon, S.; Kühne, T. D. *Phys. Rev. E* **2016**, *93*, 043305.

[194] Kapil, V.; VandeVondele, J.; Ceriotti, M. *J. Chem. Phys.* **2016**, *144*, 054111.

[195] Marsalek, O.; Markland, T. E. *J. Chem. Phys.* **2016**, *144*, 054112.

[196] Gallicchio, E.; Berne, B. J. *J. Chem. Phys.* **1994**, *101*, 9909–9918.

[197] Rabani, E.; Reichman, D. R.; Krilov, G.; Berne, B. J. *Proc. Natl. Acad. Sci. U.S.A.* **2002**, *99*, 1129–1133.

[198] Habershon, S.; Braams, B. J.; Manolopoulos, D. E. *J. Chem. Phys.* **2007**, *127*, 174108.

[199] Wang, H.; Sun, X.; Miller, W. H. *J. Chem. Phys.* **1998**, *108*, 9726–9736.

[200] Sun, X.; Wang, H.; Miller, W. H. *J. Chem. Phys.* **1998**, *109*, 7064–7074.

[201] Miller, W. H. *J. Phys. Chem. A* **2001**, *105*, 2942–2955.

[202] Shao, J.; Makri, N. *J. Phys. Chem. A* **1999**, *103*, 7753–7756.

[203] Habershon, S.; Manolopoulos, D. E. *J. Chem. Phys.* **2009**, *131*, 244518.

[204] Liu, J.; Miller, W. H.; Paesani, F.; Zhang, W.; Case, D. A. *J. Chem. Phys.* **2009**, *131*, 164509.

[205] Craig, I. R.; Manolopoulos, D. E. *J. Chem. Phys.* **2004**, *121*, 3368–3373.

[206] Ramírez, R.; López-Ciudad, T.; Kumar P, P.; Marx, D. *J. Chem. Phys.* **2004**, *121*, 3973–3983.

[207] Habershon, S.; Fanourgakis, G. S.; Manolopoulos, D. E. *J. Chem. Phys.* **2008**, *129*, 074501.

[208] Shiga, M.; Nakayama, A. *Chem. Phys. Lett.* **2008**, *451*, 175–181.

[209] Witt, A.; Ivanov, S. D.; Shiga, M.; Forbert, H.; Marx, D. *J. Chem. Phys.* **2009**, *130*, 194510.

[210] Cao, J.; Voth, G. A. *J. Chem. Phys.* **1994**, *100*, 5093–5105.

[211] Jang, S.; Voth, G. A. *J. Chem. Phys.* **1999**, *111*, 2371–2384.

[212] Voth, G. A. *Adv. Chem. Phys.* **2007**, *93*, 135–218.

[213] Trenins, G.; Willatt, M. J.; Althorpe, S. C. *J. Chem. Phys.* **2019**, *151*, 054109.

[214] Trenins, G.; Althorpe, S. C. *J. Chem. Phys.* **2018**, *149*, 014102.

[215] Rossi, M.; Ceriotti, M.; Manolopoulos, D. E. *J. Chem. Phys.* **2014**, *140*, 234116.

[216] Rossi, M.; Kapil, V.; Ceriotti, M. *J. Chem. Phys.* **2018**, *148*, 102301.

[217] Craig, I. R.; Manolopoulos, D. E. *J. Chem. Phys.* **2005**, *122*, 084106.

[218] Craig, I. R.; Manolopoulos, D. E. *J. Chem. Phys.* **2005**, *123*, 034102.

[219] Lawrence, J. E.; Fletcher, T.; Lindoy, L. P.; Manolopoulos, D. E. *J. Chem. Phys.* **2019**, *151*, 114119.

[220] Lawrence, J. E.; Manolopoulos, D. E. *Faraday Discuss.* **2020**, *221*, 9–29.

[221] Habershon, S.; Manolopoulos, D. E.; Markland, T. E.; Miller, T. F. *Annu. Rev. Phys. Chem.* **2013**, *64*, 387–413.

[222] Pérez de Tudela, R.; Aoiz, F. J.; Suleimanov, Y. V.; Manolopoulos, D. E. *J. Phys. Chem. Lett.* **2012**, *3*, 493–497.

[223] Richardson, J. O.; Althorpe, S. C. *J. Chem. Phys.* **2009**, *131*, 214106.

[224] Hele, T. J. H.; Althorpe, S. C. *J. Chem. Phys.* **2013**, *138*, 084108.

[225] Hele, T. J. H.; Althorpe, S. C. *J. Chem. Phys.* **2013**, *139*, 084116.

[226] Althorpe, S. C.; Hele, T. J. H. *J. Chem. Phys.* **2013**, *139*, 084115.

[227] Suleimanov, Y. V.; Collepardo-Guevara, R.; Manolopoulos, D. E. *J. Chem. Phys.* **2011**, *134*, 044131.

[228] Hele, T. J. H.; Willatt, M. J.; Muolo, A.; Althorpe, S. C. *J. Chem. Phys.* **2015**, *142*, 134103.

[229] Hele, T. J. H.; Willatt, M. J.; Muolo, A.; Althorpe, S. C. *J. Chem. Phys.* **2015**, *142*, 191101.

[230] Coleman, S. *Phys. Rev. D* **1977**, *15*, 2929–2936.

[231] Caldeira, A.; Leggett, A. *Ann. Phys.* **1983**, *149*, 374–456.

[232] Miller, W. H. *J. Chem. Phys.* **1975**, *62*, 1899–1906.

[233] Richardson, J. O. *J. Chem. Phys.* **2018**, *148*, 200901.

[234] Affleck, I. *Phys. Rev. Lett.* **1981**, *46*, 388–391.

[235] Rommel, J. B. Improvements to the Instanton Method: Tunneling Rates in the Enzyme Glutamate Mutase. Ph.D. thesis, Universität Stuttgart, 2012.

[236] Richardson, J. O. *Int. Rev. Phys. Chem.* **2018**, *37*, 171–216.

[237] Arnaldsson, A. Calculation of quantum mechanical rate constants directly from ab initio atomic forces. Ph.D. thesis, University of Washington, 2007.

[238] Richardson, J. O. *J. Chem. Phys.* **2016**, *144*, 114106.

[239] Kleinert, H. *Path Integrals in Quantum Mechanics, Statistics, Polymer Physics, and Financial Markets. 5th ed.*; World Scientific, 2009.

[240] Faddeev, L.; Popov, V. *Phys. Lett. B* **1967**, *25*, 29–30.

[241] Zhang, Y.; Rommel, J. B.; Cvitaš, M. T.; Althorpe, S. C. *Phys. Chem. Chem. Phys.* **2014**, *16*, 24292–24300.

[242] Richardson, J. O. *Faraday Discuss.* **2016**, *195*, 49–67.

[243] Beyer, A. N.; Richardson, J. O.; Knowles, P. J.; Rommel, J.; Althorpe, S. C. *J. Phys. Chem. Lett.* **2016**, *7*, 4374–4379.

[244] Richardson, J. O. *Phys. Chem. Chem. Phys.* **2017**, *19*, 966–970.

[245] Andersson, S.; Nyman, G.; Arnaldsson, A.; Manthe, U.; Jónsson, H. *J. Phys. Chem. A* **2009**, *113*, 4468–4478.

[246] Richardson, J. O.; Althorpe, S. C. *J. Chem. Phys.* **2011**, *134*, 054109.

[247] Seideman, T.; Miller, W. H. *J. Chem. Phys.* **1992**, *96*, 4412–4422.

[248] Althorpe, S. C. *J. Chem. Phys.* **2011**, *134*, 114104.

[249] Löhle, A.; Kästner, J. *J. Chem. Theory Comput.* **2018**, *14*, 5489–5498.

[250] McConnell, S. R.; Löhle, A.; Kästner, J. *J. Chem. Phys.* **2017**, *146*, 074105.

[251] Richardson, J. O. *Faraday Discuss.* **2016**, *195*, 49–67.

[252] Rommel, J. B.; Goumans, T. P. M.; Kästner, J. *J. Chem. Theory Comput.* **2011**, *7*, 690–698.

[253] Kapil, V. et al. *Comp. Phys. Commun.* **2019**, *236*, 214–223.

[254] Ceriotti, M.; More, J.; Manolopoulos, D. E. *Comp. Phys. Commun.* **2014**, *185*, 1019–1026.

[255] Kapil, V.; Engel, E.; Rossi, M.; Ceriotti, M. *J. Chem. Theory Comput.* **2019**, *15*, 5845–5857.

[256] Hutter, J.; Iannuzzi, M.; Schiffmann, F.; VandeVondele, J. *WIREs Comput. Mol. Sci.* **2014**, *4*, 15–25.

[257] Aradi, B.; Hourahine, B.; Frauenheim, T. *J. Phys. Chem. A* **2007**, *111*, 5678–5684.

[258] Plimpton, S. *J. Comput. Phys.* **1995**, *117*, 1–19.

[259] Soler, J. M.; Artacho, E.; Gale, J. D.; García, A.; Junquera, J.; Ordejón, P.; Sánchez-Portal, D. *J. Phys. Condens. Matter* **2002**, *14*, 2745–2779.

[260] Nocedal, J.; Wright, S. *Numerical optimization*, 2nd ed.; Springer: New York, NY, 2006.

[261] Litman, Y.; Richardson, J. O.; Kumagai, T.; Rossi, M. *J. Am. Chem. Soc.* **2019**, *141*, 2526–2534.

[262] Henkelman, G.; Jónsson, H. *J. Chem. Phys* **1999**, *111*, 7010–7022.

[263] Jonsson, H.; Mills, G.; Jacobsen, K. W. *Classical and Quantum Dynamics in Condensed Phase Simulations*; 1998; pp 385–404.

[264] Henkelman, G.; Uberuaga, B. P.; Jónsson, H. *J. Chem. Phys.* **2000**, *113*, 9901–9904.

[265] E, W.; Ren, W.; Vanden-Eijnden, E. *Phys. Rev. B* **2002**, *66*, 052301.

[266] E, W.; Ren, W.; Vanden-Eijnden, E. *J. Chem. Phys.* **2007**, *126*, 164103.

[267] Packwood, D.; Kermode, J.; Mones, L.; Bernstein, N.; Woolley, J.; Gould, N.; Ortner, C.; Csányi, G. *J. Chem. Phys.* **2016**, *144*, 164109.

[268] Mones, L.; Ortner, C.; Csányi, G. *Sci. Rep.* **2018**, *8*, 13991.

[269] Nichols, J.; Taylor, H.; Schmidt, P.; Simons, J. *J. Chem. Phys.* **1990**, *92*, 340–346.

[270] Richardson, J. Ring-polymer approaches to instanton theory. Ph.D. thesis, University of Cambridge, 2012.

[271] Olsen, R. A.; Kroes, G. J.; Henkelman, G.; Arnaldsson, A.; Jónsson, H. *J. Chem. Phys.* **2004**, *121*, 9776–9792.

[272] Fletcher., R. *Practical Methods of Optimization. 2nd ed.*; John Wiley & Sons, 1987.

[273] Rommel, J. B.; Kästner, J. *J. Chem. Phys.* **2011**, *134*, 184107.

[274] Ásgeirsson, V.; Arnaldsson, A.; Jónsson, H. *J. Chem. Phys.* **2018**, *148*, 102334.

[275] Auckenthaler, T.; Blum, V.; Bungartz, H.-J.; Huckle, T.; Johanni, R.; Krämer, L.; Lang, B.; Lederer, H.; Willems, P. *Parallel Comput.* **2011**, *37*, 783–794.

[276] `https://gitlab.com/litman90/pyelpa-examples`.

[277] Winter, P.; Richardson, J. O. *J. Chem. Theory Comput.* **2019**, *15*, 2816–2825.

[278] Meisner, J.; Kästner, J. *J. Chem. Theory Comput.* **2018**, *14*, 1865–1872.

[279] Henri-Rousseau, O.; Blaise, P. *Adv. Chem. Phys.*; Wiley-Blackwell, 2008; Chapter 5, pp 245–496.

[280] Behler, J.; Parrinello, M. *Phys. Rev. Lett.* **2007**, *98*, 146401.

[281] Hastie, T.; Tibshirani, R.; Friedman, J. *The Elements of Statistical Learning, 2nd ed.*; Springer, New York, 2009.

[282] Tuckerman, M. E.; Marx, D. *Phys. Rev. Lett.* **2001**, *86*, 4946–4949.

[283] Lin, C.; Durant, E.; Persson, M.; Rossi, M.; Kumagai, T. *J. Phys. Chem. Lett.* **2019**, *10*, 645–649.

[284] Fang, W.; Chen, J.; Pedevilla, P.; Li, X.-Z.; Richardson, J. O.; Michaelides, A. *Nat. Comm.* **2020**, *11*, 1689.

[285] Woodruff, D. P. *J. Phys. Condens. Matter* **2016**, *28*, 491001.

[286] Nakamura, M.; Sato, N.; Hoshi, N.; Soon, J. M.; Sakata, O. *J. Phys. Chem. C* **2009**, *113*, 4538–4542.

[287] Donadio, D.; Ghiringhelli, L. M.; Delle Site, L. *J. Am. Chem. Soc.* **2012**, *134*, 19217–19222.

[288] Peköz, R.; Wörner, S.; Ghiringhelli, L. M.; Donadio, D. *J. Phys. Chem. C* **2014**, *118*, 29990–29998.

[289] Peköz, R.; Donadio, D. *J. Phys. Chem. C* **2017**, *121*, 16783–16791.

[290] Endo, O.; Nakamura, M.; Sumii, R.; Amemiya, K. *J. Phys. Chem. C* **2012**, *116*, 13980–13984.

[291] Habershon, S.; Manolopoulos, D. E. *J. Chem. Phys.* **2011**, *135*, 224111.

[292] Ferri, N.; Ambrosetti, A.; Tkatchenko, A. *Phys. Rev. Materials* **2017**, *1*, 026003.

[293] Shiotari, A.; Sugimoto, Y. *Nat. Commun.* **2017**, *8*, 14313.

[294] Litman, Y.; Behler, J.; Rossi, M. *Faraday Discuss.* **2020**, *221*, 526–546.

[295] Gruber, T.; Liao, K.; Tsatsoulis, T.; Hummel, F.; Grüneis, A. *Phys. Rev. X* **2018**, *8*, 021043.

[296] Zhang, I. Y.; Grüneis, A. *Front. Mater.* **2019**, *6*, 123.

[297] Brandenburg, J. G.; Zen, A.; Fitzner, M.; Ramberger, B.; Kresse, G.; Tsatsoulis, T.; Grüneis, A.; Michaelides, A.; Alfè, D. *J. Phys. Chem. Lett.* **2019**, *10*, 358–368.

[298] Laude, G.; Calderini, D.; Tew, D. P.; Richardson, J. O. *Faraday Discuss.* **2018**, *212*, 237–258.

[299] Cooper, A. M.; Hallmen, P. P.; Kästner, J. *J. Chem. Phys.* **2018**, *148*, 094106.

[300] Chmiela, S.; Sauceda, H. E.; Müller, K.-R.; Tkatchenko, A. *Nature Commun.* **2018**, *9*, 3887.

[301] The PLUMED Consortium, *Nat. Methods* **2019**, *16*, 670–673.

[302] Lejaeghere, K. et al. *Science* **2016**, *351*.

[303] Kapil, V.; VandeVondele, J.; Ceriotti, M. *J. Chem. Phys.* **2016**, *144*, 054111.

[304] Schreiner, P. R.; Reisenauer, H. P.; Ley, D.; Gerbig, D.; Wu, C.-H.; Allen, W. D. *Science* **2011**, *332*, 1300–1303.

[305] Schreiner, P. R. *J. Am. Chem. Soc.* **2017**, *139*, 15276–15283.

[306] Lee, J.; Crampton, K. T.; Tallarida, N.; Apkarian, V. A. *Nature* **2019**, *568*, 78–82.

[307] Head-Gordon, M.; Tully, J. C. *Phys. Rev. B* **1992**, *46*, 1853–1856.

[308] Pedroza, L. S.; Brandimarte, P.; Rocha, A. R.; Fernández-Serra, M.-V. *Chem. Sci.* **2018**, *9*, 62–69.

[309] Kügel, J.; Klein, L.; Leisegang, M.; Bode, M. *J. Phys. Chem. C* **2017**, *121*, 28204–28210.

[310] Welsch, R.; Song, K.; Shi, Q.; Althorpe, S. C.; Miller, T. F. *J. Chem. Phys.* **2016**, *145*, 204118.

[311] Ceriotti, M.; Parrinello, M. *Procedia Comput. Sci.* **2010**, *1*, 1607–1614.

[312] Dettori, R.; Ceriotti, M.; Hunger, J.; Colombo, L.; Donadio, D. *J. Phys. Chem. Lett.* **2019**, *10*, 3447–3452.

[313] Corchado, J. C.; Bravo, J. L.; Espinosa-Garcia, J. *J. Chem. Phys.* **2009**, *130*, 184314.